Plasmon Hybridization in Self-Assembled 3D Graphene-based Metamaterials

A THESIS SUBMITTED TO THE FACULTY OF THE
UNIVERSITY OF MINNESOTA
BY

Kriti Agarwal

IN PARTIAL FULFILLMENT OF THE REQUIREMNETS FOR
THE DEGREE OF
DOCTOR OF PHILOSOPHY

Advisor: Prof. Jeong-Hyun Cho

April 2020

Copyright

Acknowledgement

This work, my future career, and a major part of who I am today would have never been possible without the support and guidance of my advisor Prof. Jeong-Hyun Cho. I express my everlasting gratitude to him for giving me the opportunity to learn from him and for patiently reshaping all my pre-conceived notions to re-design me to be a more hardworking and humbler person. Even outside of the research, Prof. Cho offered his guidance every step of the way over the last size year and no words can ever appropriately acknowledge his contribution to my success.

I am also grateful to some of the most encouraging, patient, and brilliant faculty members with whom I had the opportunity to work, Prof. Campbell, Prof. Tony Low, and Prof. Sang-Hyun Oh. I would like to thank my committee members: Prof. Cohen, Prof. Low, and Prof. Wang for their encouragement and insightful suggestions.

I would never have been able to successfully complete these projects without the contributions and support from my colleagues: Dr. Andrei Nemilentsau, Prof. Daeha Joung, Dr. Chao Liu, and Chunhui Dai. A special thank you to Dr. Liu and Mr. Dai for helping me maintain my sanity by their

brotherhood and positive spirit throughout the past six years for which they have my lifelong friendship and gratitude. I am also grateful to the undergraduate student collaborators Nicholas Buchele and Rezkath Awal who made significant contribution in the graphical design for the complex 3D geometries. I would also like to thank Prof. Hyeong-Ryeol. Park, Prof. Sang-Hyun Oh, Prof. Greg Haugstad, and Dr. Hans Bechtel for their assistance in characterizing the 3D SRRs and graphene.

Finally, I would have never even begun this journey of being a PhD student or come close to finishing it without the lifetime of support, encouragement, and opportunities I have received from my parents who have made my success and happiness their priority through every twists and turns of life.

Dedication

To my parents,

for being my rock and trusting all my crazy decisions

To my Nani,

for being the inspiration every woman deserves.

Abstract

Three-dimensional (3D) photonic geometries are attractive for developing novel coupled optical modes that cannot exist in the two-dimensional (2D) nano and microfabrication world. In this thesis, the various optical properties that can be induced as a result of 3D architecture are designed, fabricated, and characterized. Even for the well-established resonance in split-ring resonator-based metamaterials, the addition of the multiple planes of symmetric coupling or decoupling induce isotropic and anisotropic resonances for applications such as ultra-sensitive molecular analysis with two-fold advantage of frequency and amplitude monitoring for small concentrations and low on-chip power inclinometers with nanodegree sensitivity, respectively.

The limited spatial coverage of the plasmon-enhanced near-field in 2D graphene ribbons presents a major hurdle in practical applications. The ability to transform 2D materials into 3D structures while preserving their unique inherent properties offers enticing opportunities for the development of diverse applications for next-generation micro/nanodevices. Diverse self-assembled 3D graphene architectures are explored here that induce hybridized plasmon modes by simultaneous in-plane and out-of-plane coupling to

overcome the limited coverage in 2D ribbons. While 2D graphene can only demonstrate in-plane bi-directional coupling through the edges, 3D architectures benefit from fully symmetric 360° coupling at the apex of pyramidal graphene, orthogonal four-directional coupling in cubic graphene, and uniform cross-sectional radial coupling in tubular graphene. The 3D coupled vertices, edges, surfaces, and volumes induce corresponding enhancement modes that are highly dependent on their shape and dimensions. While most of this work strives to achieve multiple coupled planes of symmetry, the same ideas are also applied to achieve multiple 3D graphene geometries that break mirror symmetry across multiple planes. The asymmetric graphene induces giant optical activity (chirality) that has remained previously unrealized due to the 2D nature of graphene. The chirality induced within the 3D graphene chiral helixes is also a strong function of the geometrical parameters that are analyzed using a machine-learning-based multivariate regression approach to determine the 3D geometry with the strongest chirality. The hybrid modes introduced through the 3D couplings amplify the limited plasmon response in 2D ribbons to deliver non-diffusion-limited sensors, high-efficiency fuel cells, and extreme propagation length optical interconnects.

Table of Contents

List of Tables

List of Figures

List of Abbreviations

2D: two-dimensional

3D: three-dimensional

AFM: Atomic force microscopy

Al_2O_3: aluminum oxide

Au: gold

C-C: Carbon-Carbon

CD: circular dichroism

Cr: chromium

Cu: copper

CVD: chemical vapor deposition

DA: detection accuracy

DI: deionized

DNA: deoxyribonucleic Acid

EBL: electron beam lithography

FET: field-effect transistor

FOM: figure of merit

FTIR: Fourier transform infrared

FWHM: full width half maximum

h-BN: hexagonal Boron Nitride

HF: Hydroflouric acid

IR: Infrared

I-V: Current-Voltage

LCP: left circular polarization

LSPR: Localized surface plasmon resonance

PE: Polyethylene

PMMA: Poly(methyl methacrylate)

QCL: Quantum cascade laser

Q-factor: quality factor

RCP: right circular polarization

RIE: reactive ion etching

SEM: scanning electron microscope

SERS: surface-enhance Raman spectroscopy

Si: Silicon

SiC: Silicon Carbide

SINS: Synchotron Infrared Nanospectroscopy

SiO_2: Silicon Dioxide

Sn: tin

SNR: Signal to Noise Ratio

SPP: surface plasmon polariton

SRR: split ring resonator

TDS: Time-domain spectroscopy

TE: Transverse Electric

THz: terahertz

TM: Transverse Magnetic

Chapter 1

Current State of Three-dimensional Graphene-based Materials

1.1 Introduction

The mechanical exfoliation of a single layer of hexagonally arranged carbon atoms from bulk graphite by Geim, et. al. [1] led to the first step in what has been more than a decade of groundbreaking research in two-dimensional (2D) materials. Since then several types of 2D materials have been explored, such as graphene, graphene oxide (GO), transition metal dichalcogenides (TMDCs), and black phosphorus [2-4]. Each of these materials possesses its own extraordinary electronic, optical, mechanical, and permeation properties, making them model systems for the observation of unknown physical phenomena as well as being suitable to be used as building blocks for future devices [5-7]. However, the original 2D material, graphene, has continued to sustain its original momentum owing to its zero-gap band structure, extraordinary carrier mobility, intrinsic tensile strength of 130 GPa and

Young's modulus of 1 TPa, superior optical absorption, and a high thermal conductivity of about 5 kW/mK [8,9].

Describing the many beneficial properties of graphene and their applications could fill a library many times over. Therefore, in the rest of this chapter, we focus only on the optical properties of graphene, their applications, limitations, and available transformation routes to realize novel devices.

1.1.1 Plasmon excitation in graphene

The delocalized π-orbitals in graphene give rise to its extraordinary optical properties [10]. There are several routes available to control the light-matter interaction in graphene, namely, electrical gating, structural engineering, and coupling between graphene layers [11-13]. In the infrared (IR) frequency regime, the photon energy overlaps with the elementary excitations in graphene, including interband and intraband electronic transitions, Landau level transitions, and plasmon excitations [14]. Especially the interband transitions in graphene are highly gate-tunable by electrostatic doping through Pauli blocking with carrier concentrations exceeding 10^{14} cm^{-2}. Furthermore, in the Drude weight that defines the intraband transitions from the valence to the conduction band is also related to the imperfect Pauli blocking, thus, similarly scaling with the gate doping [15]. The resulting

optical conductivity of graphene is thus composed of two components and can be given by the Kubo formula. In pristine graphene, the optical conductivity reduces to a universal frequency-independent conductance of $\sigma(\omega) = \pi.e^2/2h$, which corresponds to an absorption of 2.9% [16].

These Dirac electron transitions in graphene under incident illumination can give rise to oscillations of charge carriers i.e. plasmon excitations, which are widely different from those occurring in metals. The large difference between the Fermi velocity in graphene and the speed of light leads to a momentum mismatch that does not allow direct excitation of plasmons in graphene. Plasmons in graphene can be excited through the creation of nanostructured geometries, the most popular of them being 2D graphene nanoribbons [17, 18]. Under plane wave illumination, the plasmon excitation in the 2D graphene ribbons gives rise to a strong near-field enhancement of the incident energy (Figure 1.1a). The plasmon frequency and the near-field enhancement scale with the width of the ribbon (Figure 1.1b) as given by, $\omega_p \alpha w^{-1/2}$, where ω_p is the angular plasmon frequency and w is the width of the ribbon [19]. The near-field enhancement (NFE) in graphene can be given by $NFE = (E_0/E_i)^2$, where E_0 is the electric field amplitude under plasmon excitation and E_i is the incident electric field.

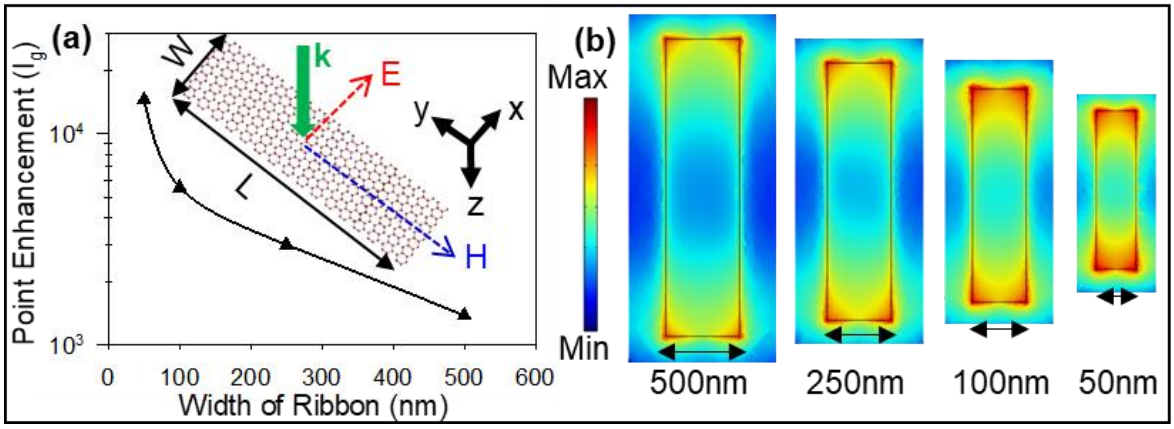

Figure 1.1 (a) Graph (log scale) showing the exponential increase in the maximum near-field enhancement for the 2D rectangular graphene ribbons when the width (and length) of the ribbon are reduced. Inset shows the illustration of a 2D graphene ribbon with length (L) and width (W) under plasmon excitation by an incident light with electric field (E), magnetic (H) field and wave vector (k) polarized in the direction as represented by the arrows (b) Simulated color map showing the variations in the field enhancement on the surface of the 2D ribbons of varying widths.

1.1.2 Applications of graphene plasmons

Owing to their extraordinary optical, electronic, and mechanical properties, two-dimensional (2D) graphene sheets have the potential to be an ideal platform for the observation of novel quantum phenomena and to serve as building blocks for future electronics, optoelectronics, and plasmonics [20-

22]. In particular, tailoring the shapes and architectures of graphene has been studied to obtain new physical phenomena. For example, lithographically patterning graphene into quantum dots and nanoribbons produces a finite energy gap, leading to new properties such as quantum confinement effects, magnetism, spin-polarized edge states, and localized electron distributions [23, 24]. The extreme light confinement by 2D graphene plasmons enhances the electric field around the graphene surface, making the near-field intensity several orders of magnitude higher than the incident wave. The long lifetime tunable plasmon resonance alongside superior mechanical properties in graphene have been utilized for a diverse range of applications such as reconfigurable metamaterials and optoelectronic devices for photodetection, vibrational spectroscopy techniques, solar cells, cell therapeutics, and light sources [25-29]. Out of all these diverse plasmon applications, a unique advantage further stems from the capability to perform mid-IR and Terahertz (THz) biosensing [30].

Sensing and analysis of biological specimens in this spectral regime gives vital information about their primary structure, hydrogen and van der Waals bonds, molecular vibrations, molecular rotations, and chemical composition with peaks in the frequency spectra corresponding to each molecular resonance in the specimen (Figure 1.2a). The activation of DNA

mutations for a variety of diseases such as Alzheimer's, sickle cell anemia, and cancers with short lead time and a requiring early intervention, is reflected by a modification in the protein molecules and DNA, respectively [31-33]. However, a three order of magnitude difference between the wavelength of incident light (micrometer scale) and size of biological molecules (nanometer scale) leads to extremely small absorption and indiscernible transmission peaks in the frequency spectrum (Figure 1.2b). The low absorption limits the sensitivity of optical detection techniques to millimolar range, acting as a significant hindrance in its application for early diagnosis requiring sensitivities in the picomolar range. The surface plasmons in graphene enhance the incident light by five orders of magnitude by confining it to nanoscale dimensions [34]. Unlike bio-sensing with conventional metal plasmonics, the graphene plasmon can be spectrally tunable with an electrical gate, allowing one to obtain full vibrational spectra information i.e. the absorbed molecules fingerprint. The specimens can couple to the plasmon field through molecular vibrational modes. When the plasmon and the phonon resonance coincide, the plasmon reveals a narrow transparent window in conjunction with the broad main plasmonic spectral resonance. This narrow transparency is a result of the destructive interference between the plasmons and phonons. This phonon-induced transparency effect underlies the basic principle for detecting the

vibrational modes of adsorbed molecules, hence allowing spectral determination of the chemical "fingerprint". Due to the spectroscopy-like nature of the information obtained, it also provides a clear advantage in signal-to-noise ratio as compared to conventional electronic biosensors. Recently, several plasmonic sensing devices based on graphene nanostructures have been developed for detecting various targets such as chemical compounds, biomaterials, and gases [35-38].

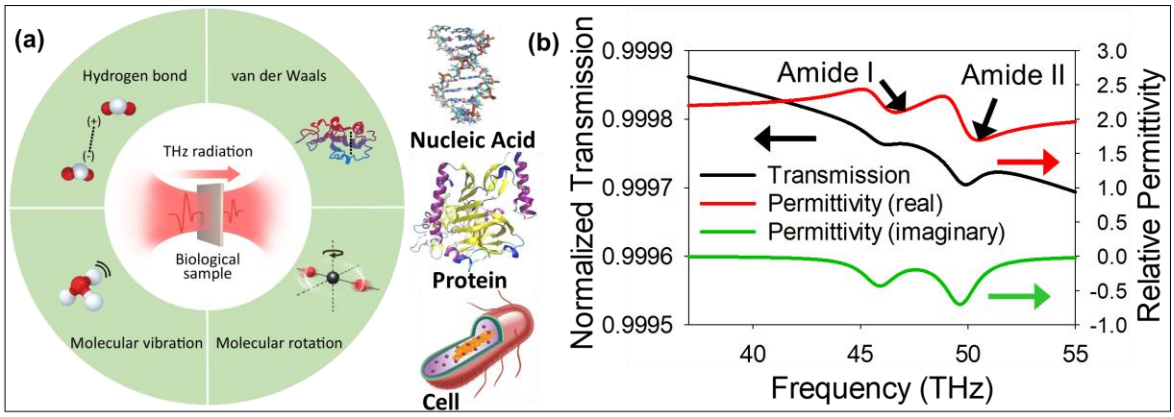

Figure 1.2 (a) Biomedical Applications of Terahertz (THz) Spectroscopy [30]. (b) Graph showing the optical transmission amplitude for bovine protein (black line) as well as the variations in real (red line) and imaginary (green line) part of protein's relativity permittivity with frequency, which cause the optical resonances.

1.2 Limitations of 2D graphene plasmons

Any external molecule that is brought into the vicinity of the enhanced electric (E) field at the surface of the graphene-based sensors, causes a change in the refractive index of the interface proportional to the dielectric properties of the target molecule. For a GNR with the incident E-field polarized along the width of the ribbon, the incident photons give rise to a strong NFE at the corners and edges of the ribbon. The NFE is directly proportional to the intensity of the photons that will be absorbed by the targeted molecule and is thus a key parameter in determining the performance of the sensor. For a GNR of width 500 nm, the NFE drops by 64% even 20 nm away from the surface (Figure 1.3a). At low concentrations of analyte (<100pM), the detection is primarily limited by diffusion of the molecules to the surface of the GNR due to the exponential decay of the enhanced E field away from the surface, which occurs for all plasmon frequency and GNR widths (Figure 1.3b). This constraint limits the sensitivity of plasmonic sensors to $1x10^{-12}$ mol/cm^2, which fails in analysis of single protein or molecules with a radius of 2 nm that require a minimum detection limit in femto and atto moles [39-42].

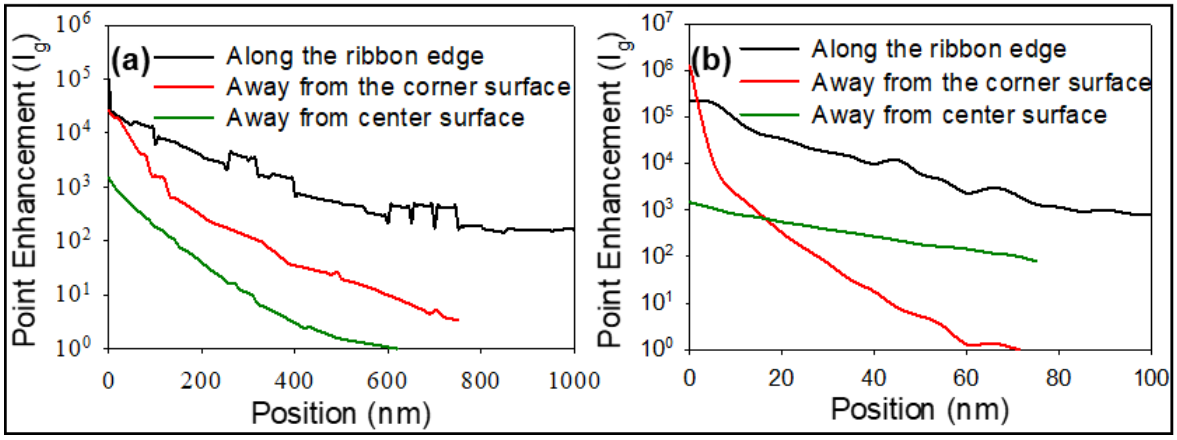

Figure 1.3 Change in the near field enhancement obtained at the surface of the ribbon for (a) width = 500 nm and Length = 2000 nm, and (b) Width = 50 nm and Length = 200 nm when the position is increased away from the surface of the ribbon (black line) and on the surface away from the edge of the ribbon (red line).

1.2.1 Methods for 2D plasmon hybridization

Rectangular nanoribbons were the first candidates for inducing direct plasmons in graphene; however, they are not the best candidate for mid-IR sensing techniques. In order to achieve a stronger absorption of the incident light and induce a stronger NFE, diverse forms of 2D graphene have been investigated [43], chief among them being arrays of graphene nanodisks [44-

47], tapered graphene [48,49], and hybrid plasmons in gap structures [50,51] and metal-coupled acoustic plasmons [52-54] as shown in Figure 1.4a-d.

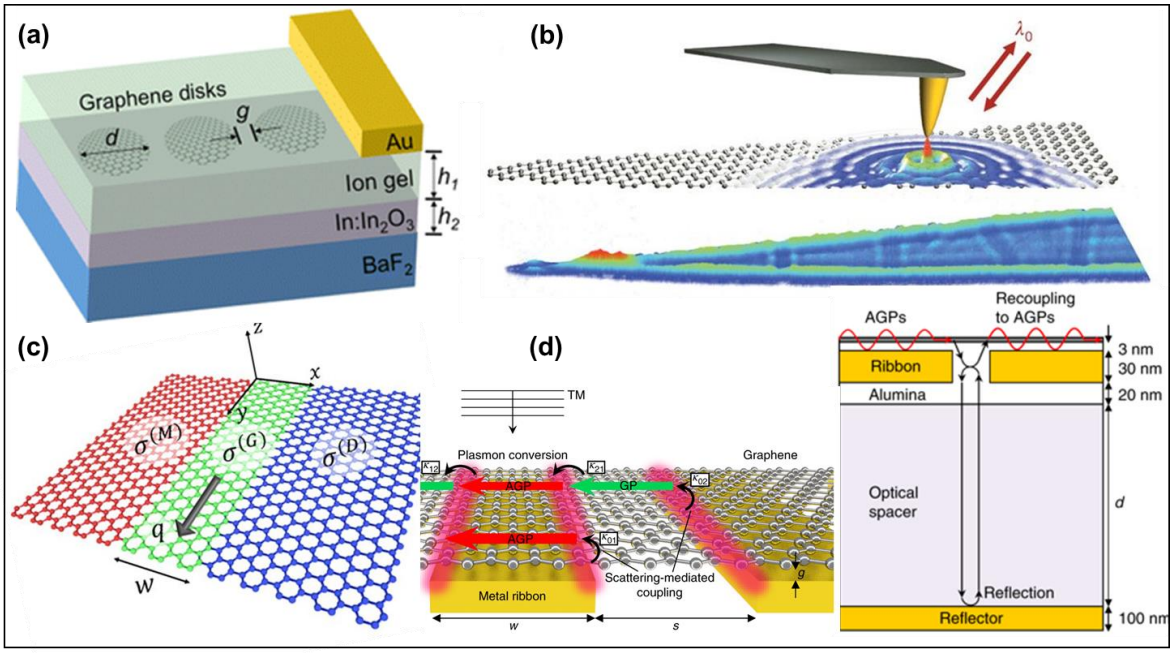

Figure 1.4 (a) Scheme of graphene nanodisk arrays. A graphene monolayer is transferred to an In–In_2O_3/BaF_2 substrate and subsequently patterned with e-beam lithography. The ion-gel was spin-coated on top of the graphene nanostructure, and the Au gate contact deposited on the top [55]. (b) Diagram of the metallized AFM tip (shown in yellow) illuminated by an infrared laser beam with wavelength λ0 and the near-field amplitude image acquired for a tapered graphene ribbon on top of 6H-SiC [48]. (c) Schematic of the proposed 2D metal-gap-dielectric system, composed of a gap domain G between two semi-infinite domains Metallic and Dielectric. The H-GGP mode is assumed to propagate along the y-axis [51]. (d) Schematic illustration of the acoustic

plasmon resonator architecture and coupling routes to plasmon modes for a plane wave normally incident with TM polarization [52].

The graphene nanodisk arrays can achieve a stronger absorption of the incident light, increasing from 3% in pristine graphene to 30% in closely spaced arrays where the extinction cross-section of each disk is designed to be comparable to the area of the unit cell [55]. In contrast, the tapered graphene geometries achieve a stronger shift of the Fermi level (and consequently a higher sensitivity) through hotspots of greater confinement due to higher plasmon energy density at the tapered tip, increasing nearly 20 times [56]. In addition, the careful design of their array composition and distance between constituting elements can lead to gap-based plasmon modes and acoustic plasmons. Both these coupled plasmon techniques follow a similar concept where a larger hybrid plasmon mode volume is achieved as well as larger "hotspots" on the graphene monolayers compared to the conventional edge plasmon modes in graphene. However, the hotspots induced in these 2D arrays are highly localized due to non-uniform 2D coupling, which also leads to broadening of their spectra and reduces the signal to ratio. The incorporation of metals and dielectric in acoustic graphene plasmons can also achieve a stronger nearly perfect absorption of the incident IR light. However, the

perfect absorption in acoustic plasmons is not accompanied by a proportional increase in the near-field enhancement, which remains similar to that of 2D graphene nanoribbons. Thus, each of these 2D techniques namely, varied graphene geometries and coupling while having their merits, continue to suffer from a severe drawback of exponential field decay in the out-of-plane direction resulting in surface-diffusion-limited sensitivities.

1.3 Pathways towards fully 3D graphene

Even with the above noted advantages of 2D graphene forms, they continue to suffer from the low spatial coverage of their enhanced near-field (Figure 1.5a). Furthermore, in the case of insulating substrates such as SiO_2 and h-BN, the planar two-dimensional graphene plasmons couple strongly with the substrate surface polar phonons as a result of large spatial overlap [57]. The substrate-dependent damping effect is further amplified in the case of semiconducting substrates such as silicon. The strong coupling between the substrate carriers and the graphene plasmons results in energy dissipation due to non-radiative surface plasmon relaxation. The substrate coupling has been

shown to degrade the quality factor of the plasmon resonance by two orders of magnitude as compared to pristine graphene [58]. The ohmic losses also significantly reduce the near-field enhancement limiting the enhanced field to only the corners of the ribbon, as opposed to pristine graphene where a uniformly decaying field can be seen across the surface of the ribbon (Figure 1.5b).

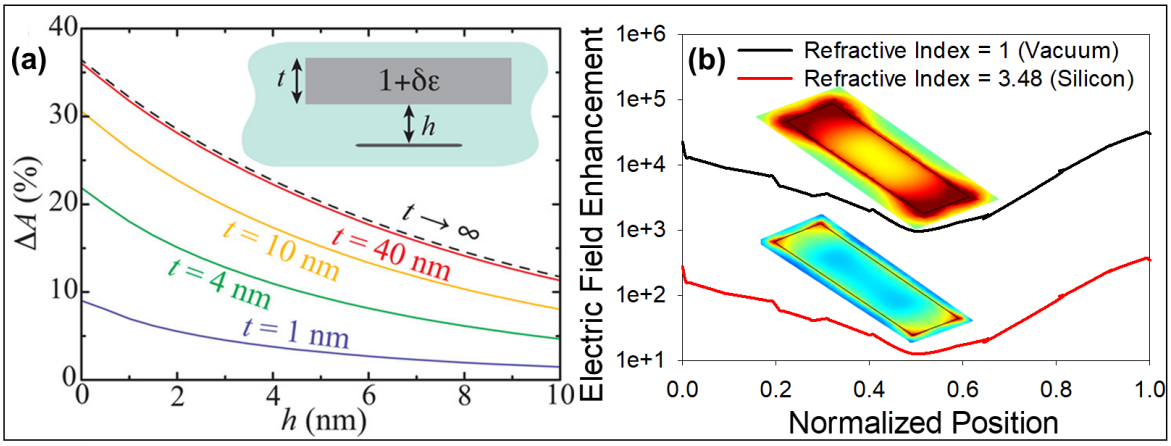

Figure 1.5 (a) Dependence of absorption cross-section, ΔA, on the molecular layer properties for a single nanodisk with Fermi level E_F = 300 meV plotted as a function of the distance, h, between the nanodisk and the molecular layer for different values of the layer thickness, t [44]. (b) Graph showing the change in electric field enhancement across the width of the 2D ribbon showing the two order of magnitude reduction on silicon (red line) compared to the enhancement in vacuum (black line).

One technique used to overcome the surface-limited fields is to extend graphene in the out-of-plane direction. A large number of techniques have been explored to achieve these “three-dimensional” forms of graphene [59, 60]. For each of the 3D forms of the properties of the resulting graphene and its applications are completely dependent on the 3D geometry and the fabrication processes involved in the realization of the structure. Here we take a look at some of the widely studied 3D graphene structures, their benefits, and shortcomings.

1.3.1 Metal-insulator-metal linearly stacked structures for 3D graphene

The graphene-insulator stacks (Figure 1.6 a, b) are formed in a manner to be similar to photonic crystal structures through the alternating deposition of graphene and a thin insulator layer, where the collective oscillation of Dirac fermions is unambiguously quantum-mechanical [61]. Compared to single-layer graphene, which has a weak dependence of plasmon resonance on the carrier concentration, distributing carriers into multiple graphene layers changes their behavior from conventional semiconductor superlattice with a higher oscillator strength than previously explored single-layer devices. The optically equivalent carrier density in these stacked graphene structures is

larger than the sum of those in the individual layers and given by $n_s^{NL} = \left(\sum_{i=1}^{N} \sqrt{\left| n_s^{(i)} \right|}\right)^2$ [62].

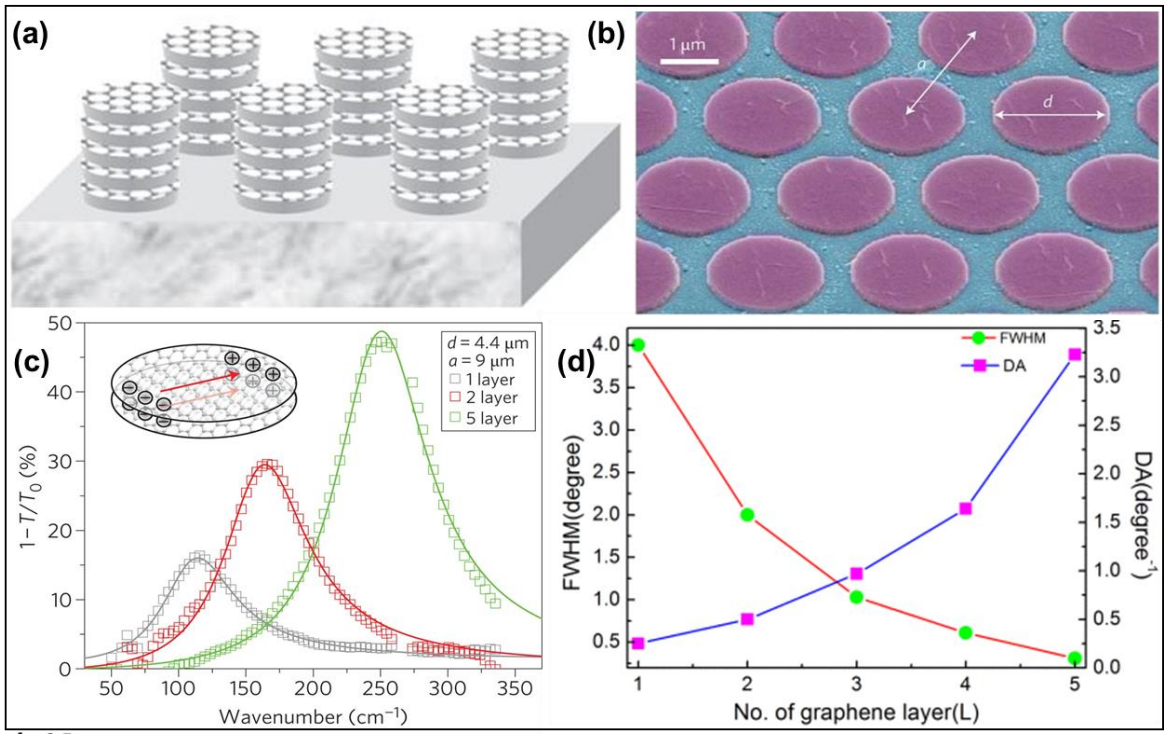

Figure 1.6 (a) Scheme of graphene stacks showing the patterning of the multilayer device into desirable structures. Patterned disk arrays are shown. (b) SEM image (false colour) of a stacked graphene/insulator microdisk array arranged in a triangular lattice (d = 2.6 μm and a = 3 μm. (c) Extinction in transmission, $1-T/T_0$, in stacked plasmonic devices with one, two and five graphene layers [61]. (d) Variation of FWHM and DA with different No. of graphene layer N from 1 to 5 at E_F = 1.0 eV [68].

Thereby, enhancing the plasmonic resonance frequency and magnitude as a direct consequence of the unique carrier density scaling law of the plasmonic resonance of Dirac fermions. Even if the stacks are separated by a large distance such that quantum mechanical coupling cannot take place, there exists an intrinsic gating of graphene layers with each other such that the interlayer spacing can be used to modulate the phase velocity and reflection of the incident light [63,64]. The stacks also benefit from allowing independent control of the complex conductivity of each layer within the stack and enhanced control on the stack's equivalent complex conductivity. These advantages of 3D graphene stacks have used for a variety of advantages such as tunable far-infrared notch filters with 8.2 dB rejection ratios, terahertz antennas, linear polarizers with 9.5 dB extinction ratios, optical switches, and biological sensors with a higher detection accuracy, DA (reciprocal of full width at half maximum, FWHM) [65-68].

1.3.2 Porous scaffold-like composite structures for 3D graphene

The first introduction of 3D graphene was in the form of 3D graphene aerosols fabricated by a freeze-drying method [69] This was followed closely

by self-assembly and template-directed fabrication of 3D graphene-based aerogels, hydrogels, organogels, sponges, and foams [70-73] (Figure 1.7). Here, sponges and foams are interchangeably used by researches with the only distinguishing factor being the degree of reversible compression allowed by them. These types of 3D structures offer two distinct advantages especially for energy applications. Firstly, as opposed to 2D graphene, the 3D structures avoid restacking, which would otherwise cause the electrocatalytic properties to degrade by acting as a barrier to active sites and increase the resistance to mass transfer [74]. Secondly, the surface area for these porous structures increases as they favor rapid mass [75]. These advantages have prompted the application of these 3D graphene structures in biomedical equipment, supercapacitors, fuel cells, and other energy storage and conversion devices [76-80]. The 3D graphene foams upon annealing induce currents in their walls that rapidly attenuates in resistive networks to convert into thermal energy [81]. Thus, delivering them with superior optical properties through stronger absorption intensity, broader qualified bandwidth, and much lower density for THz applications such as optical communication, sensing, imaging, shielding, and ultrafast photonics [82-84].

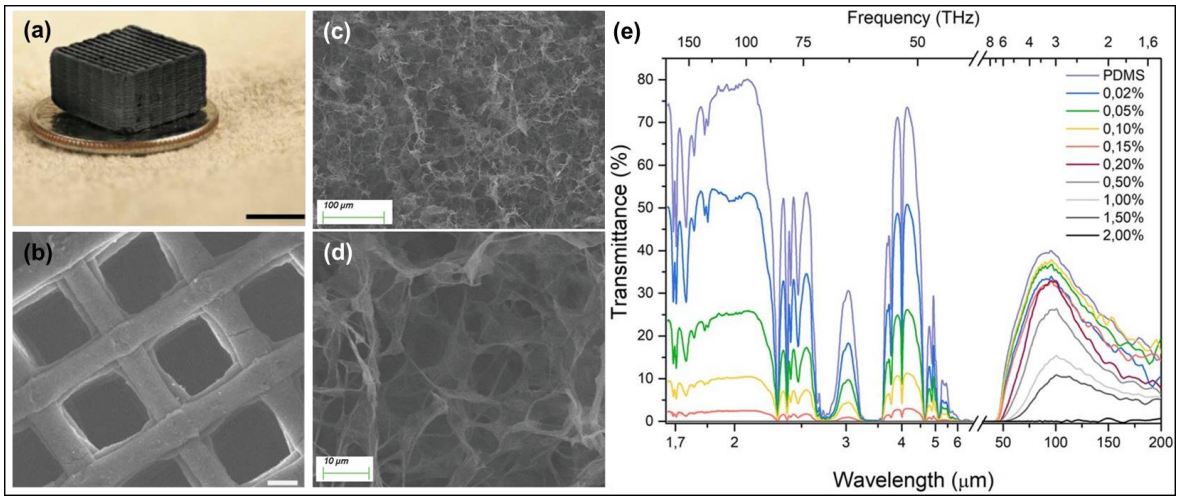

Figure 1.7 Morphology and structure of graphene aerogels microlattice with (a) Optical image and (b) SEM images [60]. (c, d) SEM images of graphene foams with different scales [84]. (e) Transmittance spectra of graphene-PDMS composite in the wide spectral range (1400 nm–200 μm) [83].

1.3.3 Template-driven hybrid geometries for 3D graphene

The 3D hybrid graphene structures are fabricated primarily by two techniques (Figure 1.8). Firstly, by directly transferring graphene onto a substrate with pre-deposited nanoparticles or prefabricated 3D nanostructures like pyramids and nanopillars, where graphene forms a uniform coating on the surface of the substrate, achieving 3D graphene-based nanostructures [85-87]. Another approach that has been investigated involves growing graphene on a

3D nanostructure, such as nanowire, by using chemical vapor deposition (CVD) [88]. This may be followed by etching of the initial nanostructure after the growth to result in a suspended 3D graphene structure. The underlying template used in both these approaches is usually metallic and forms an active layer. The graphene transferred onto the gold pyramid and nanorod structures have been shown to boost the hot spot density for surface enhanced Raman scattering (SERS), such that graphene electrons at the plasmon hot spots contribute to a large fraction of the plasmon modulation in the visible regime. Each additional electron changing the plasmon scattering intensity by about one thousandth [87], resulting in an enhancement factor of over 10^{10} for label-free single molecule sensing [85]. Even in the absence of underlying metal plasmons, the graphene plasmons in these 3D structures can be rapidly excited with a higher efficiency for both s and p polarizations [89]. On the other hand, the graphene nanorod structures that are CVD grown on nickel demonstrate broad troughs in their conductance curve with a varying gate voltage [88]. Thus, signifying that the 3D structures are less susceptible to the substrate bias, which could be explained as a consequence of weaker capacitive coupling due to the cavity created inside tubular graphene structures [90]. These characteristics of templated 3D graphene have been shown to have unique benefits in the applications of graphene for photodetectors, optical modulators,

polarizer, phototransistors, and plasmon resonance sensor [91-94].

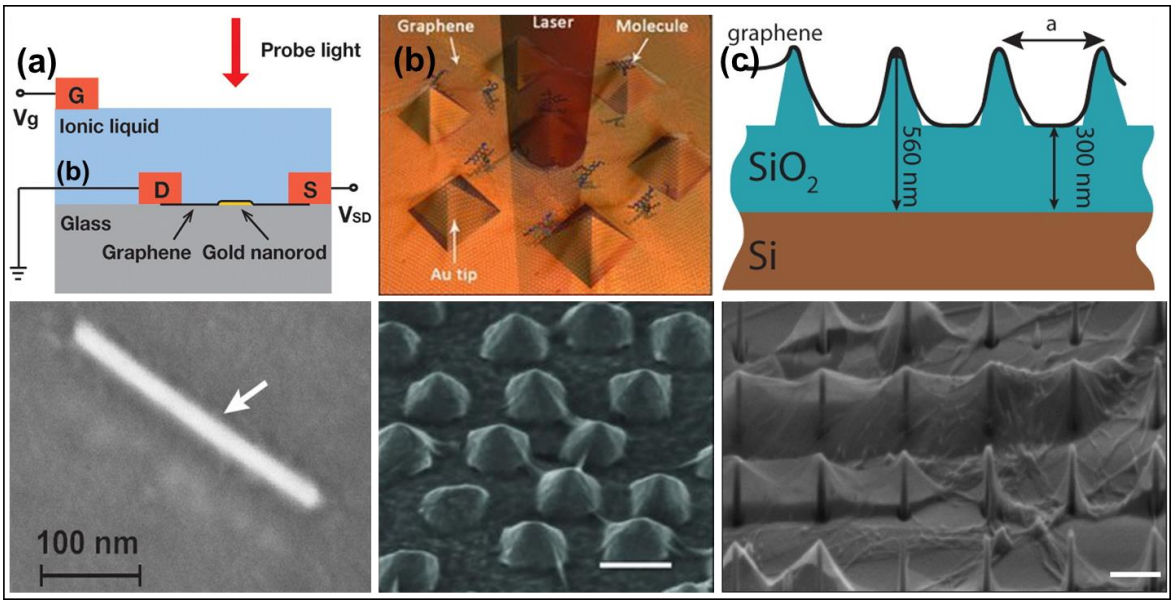

Figure 1.8 Schematic illustrations and SEM images of the 3D graphene hybrid structures showing (a) 3D graphene structures fabricated on gold nanorods [87]. (b) 3D graphene structures fabricated on hexagonally arranged gold nanopyramids [85]. (c) 3D graphene structures fabricated on silica nanopillars [89].

1.3.4 Corrugated and wrinkled structures for 3D graphene

The graphene wrinkles (Figure 1.9a) can be fabricated with a high uniformity through an array of fabrication processes such as optical forging through pulsed laser beams [95], strain engineering [96,97], heat-induced

contractile deformation of the underlying substrate [98], graphene transfer onto a substrate decorated with nanoparticles [99], differential thermal expansion coefficients of graphene and substrate [100], thermal-vibrations and interatomic interactions in the C-C bond [101], and rapid evaporation of aerosol droplets [102]. Electrical transport measurements in graphene ripples with a width lower than 10nm have shown an intrinsic bandgap of 0.1 eV with an on/off ratio in wrinkled graphene field effect transistors (FET) of 30 and a resistivity of ~56.8 kΩ/sq [103]. The electronic properties of these graphene wrinkles are a strong function of their geometrical parameters namely, height, shape, folding angle, (Figure 1.9b) which in turn controls the path taken for electron transport whether it is across, over or tunneled through the wrinkles [104]. The larges surface area and negligible doping effects from the substrate make them an ideal candidate for enhanced chemical reactivity useful in nanoelectronic applications [105]. Near-field imaging of plasmons in wrinkled graphene (Figure 1.9c) has shown significant plasmon reflections when the height of the wrinkles is larger than the plasmon wavelength [106]. The separation distance of the wrinkle tip from the substrate also leads to a variable doping profile across the wrinkle for additional modulation of the plasmon reflection. The plasmonic properties of these graphene wrinkles can be utilized for nanoscale tunable dampers in photoelectric information detectors,

transmitters, and modulators [107]. For smooth wrinkles, the dielectric environment mediates plasmon scattering with a strong suppression when graphene is placed between two dielectrics with the same refractive indices. In contrast, for sharp corrugations, the graphene plasmons are strongly reflected even for wrinkles much smaller than the plasmon wavelength [108].

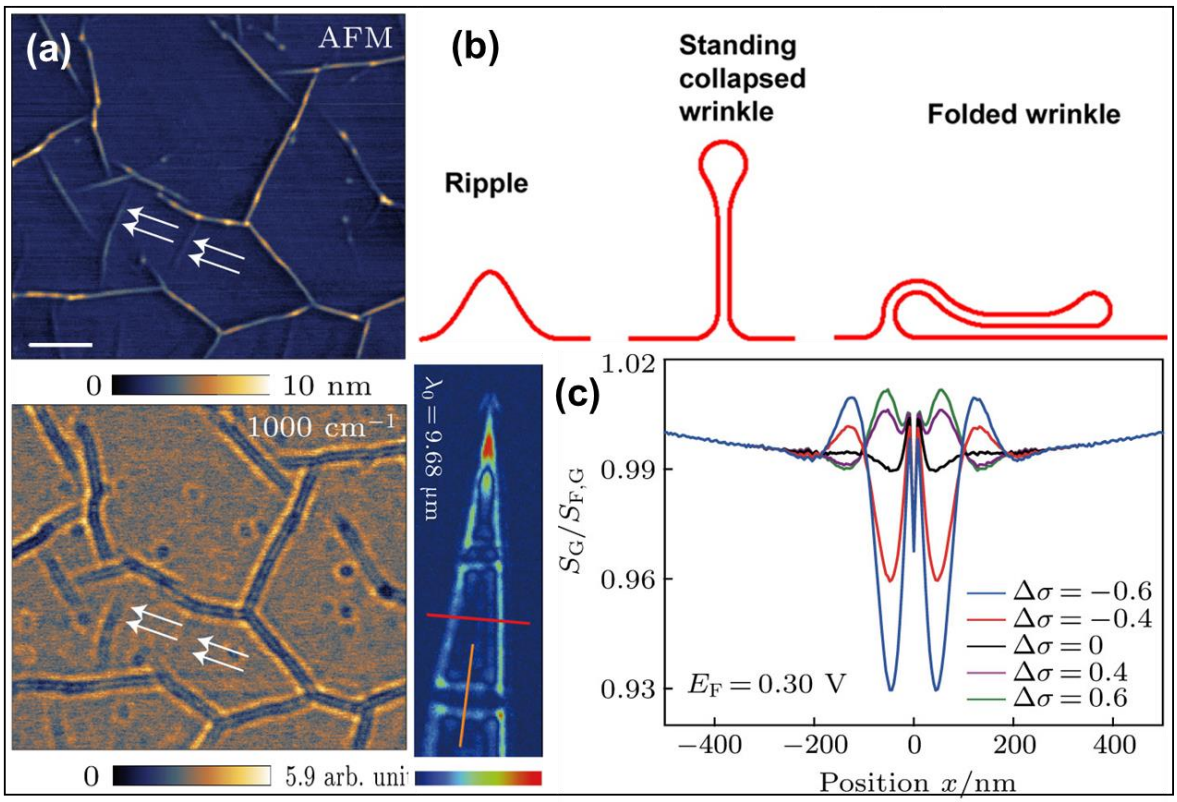

Figure 1.9 (a) AFM topography and infrared near field amplitude image at 1000 cm^{-1} of graphene wrinkles on SiC substrate. (scale bar is 500 nm) [106]. (b) Schematic illustration of three classes of graphene wrinkles [104]. (c) Near-field optical signal profiles of graphene wrinkles with different optical

conductivities at a wrinkle position. Wrinkles with increased or decreased optical conductivity give different line shapes. [107].

1.3.5 Bubble structures for 3D graphene

3D graphene nanobubbles (Figure 1.10) could be formed intrinsically as an adverse by-product of the fabrication process or through extrinsic engineering of the graphene form. Intrinsically, when placed on a substrate, due to the impermeable nature of graphene, there may be gas molecules may be trapped underneath it to form bubbles such that the number of gas molecules, elastic properties of graphene, and the interfacial adhesion between graphene and substrate control the bubble diameter and height [109]. Extrinsically, the bubbles can be formed by the etching of the underlying substrate that causes released gases to get trapped within graphene such as HF or irradiation-based etching of SiO_2/Si substrate under graphene [110]. Another extrinsic technique utilized templated graphene assembly onto polymethyl methacrylate (PMMA) latex spheres [111]. An advantage of the former technique is through the control of graphene bubble geometry by an external electric field through electrostatic interactions, allowing their application in adaptive-focus lenses, supercapacitors, and even pressure

sensors for low-cost artificial skin [112-115]. The optical activity within them is especially attractive due to the potential for graphene nanobubbles on hexagonal-boron nitride (h-BN) substrates to act as an effective plasmonic cavity for trapping plasmons with sub-hundred-nanometer spatial confinement [116]. Hybridization of the graphene plasmons with the longitudinal optical phonons of h-BN can lead to an enhancement of the optical band at 817 cm^{-1} [117]. The suspended bubbles preserve the longitudinal h-BN modes while suppressing transverse optical h-BN modes. Furthermore, the highly confined hotspots for an ideal platform for plasmon-enhanced IR spectroscopy of nanoscale objects. The targeted biomolecules can be encapsulated inside the bubbles preserving an aqueous environment to monitor structural changes in molecules while they grow within the volume of bubbles.

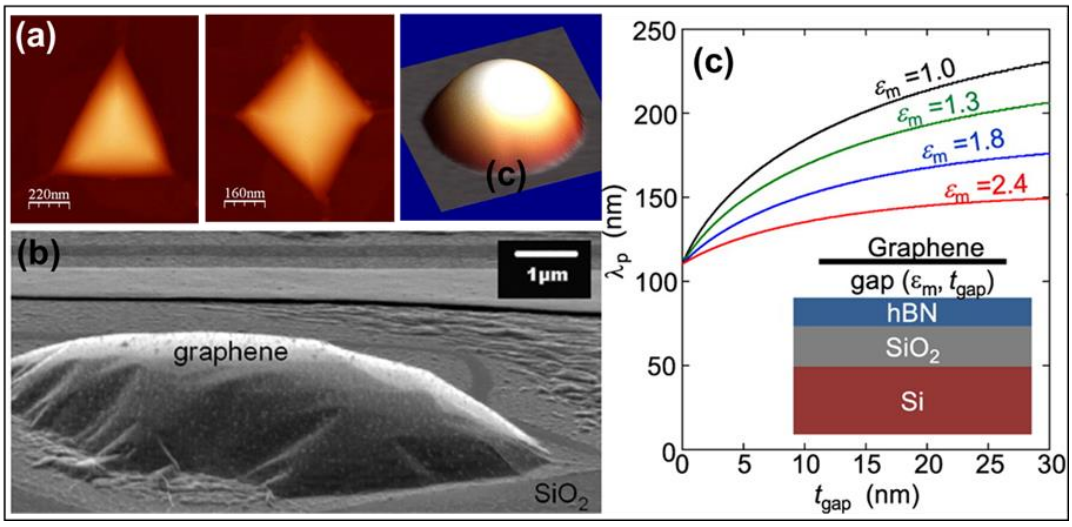

Figure 1.10 (a) AFM topography scan of triangular, square, and spherical bubbles on BN substrate [112]. (b) SEM image of a single layer graphene flake

after exposure to HF vapor, showing the microscale graphene bubble [110]. (c) Theoretical calculations of the local plasmon wavelength (λp) and dispersion diagrams of a modeled heterostructure with the height of the bubble. [116].

1.3.6 Macroscopic art-inspired structures for 3D graphene

Two paper-based art forms that originated in Japan, are well known worldwide namely, Kirigami (the art of cutting and stretching paper into 3D forms) and Origami (the art of folding paper into 3D forms). Both these art forms have been widely investigated for the development of nano and microscale devices [118]. When replacing the "paper" with graphene to yield the 3D structures via Kirigami, the most important design parameter becomes easy bending and crumpling denoted by large values of Föppl–von Kármán number, γ, which is the ratio between in-plane stiffness and out-of-plane bending stiffness [119]. The kirigami graphene pyramids have been shown to provide ballistic behavior for higher absorption of kinetic energy through multi-step dissipation mechanisms, enhancement of stretchability by 10 times compared to pristine graphene, and four orders of magnitude tunability of thermal conductivity [120-122]. No studies to date have been performed on the

plasmonics in these graphene structures, however, the electronics properties have been shown to be strongly dependent on the degree of elongation of the kirigami graphene structures [123]. At a small degree of stretching, the effective coupling between localized states is strongly reduced; but there occurs resonant tunneling at longer elongations. The kirigami structures enable the realization of coupled quantum dot array systems through alternating miniband and stopgap structure in the transmission, which has also been shown to realize negative differential conductance within certain energy levels.

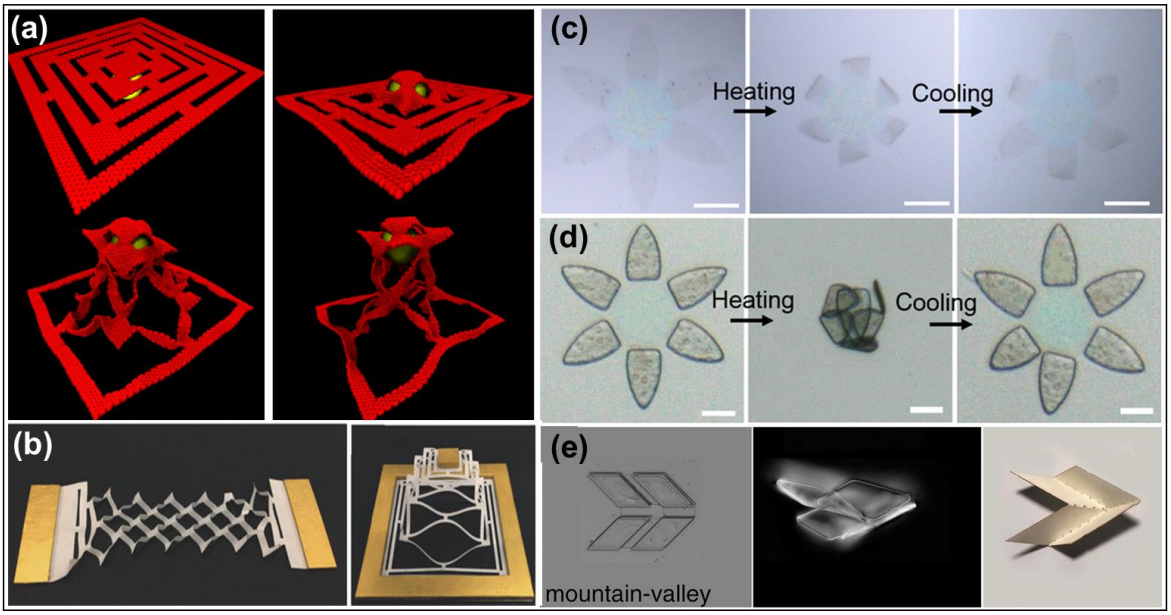

Figure 1.11 (a) Molecular dynamics snapshots showing different stages of ballistically impacted single-layer graphene kirigami pyramid [122]. (b) Stretchable graphene kirigami structure and its application in stretchable transistors. The paper models show the geometries of graphene kirigami

deformed in 2D or 3D [119]. Reversibility of the temperature-induced self-folding for origami graphene with (c) only graphene and (d) graphene with rigid SU8 petals for better stability and reversibility but with increased thickness [130]. (e) Graphene–glass bimorphs can be used to fabricate numerous 3D structures at the micrometer scale such as the bidirectional folding motifs [128].

Origami-based 3D graphene structures have been investigated to a larger extent than kirigami structures due to their energy applications [124]. The origami-inspired structures can be formed through different water absorption/desorption, hydrogenation, differential near IR absorptions, and heat-based thermally responsive folding [125-127]. The complex origami techniques have yielded diverse programmable graphene robots that can adopt predesigned shapes, walk, turn a corner, and create nanocages for storage and release of chemicals [128]. Moreover, they have been proposed for spintronic applications because of enhancement in spin-orbit interaction due to the curvature of the origami-inspired structures, which allows them to carry spin-polarized currents and have gaps in the electronic spectrum in the presence of weak magnetic fields [129]. The electronic properties of the 3D graphene origami structures are also affected much like in kirigami-inspired structures

with the current-voltage (I-V) curves transforming to non-linear. The structures enable shifting of the Dirac point upon folding and an increase in the resistance with the folding crease due to their behavior as a tunnel barrier for the current flow [130].

1.4 Quick summary

Table 1.1 is a quick summary of all the current 2D and 3D techniques to enhance or tune the intrinsic properties of graphene from nanoscale to centimeter scale. The table lists the geometry achieved, dimensionality, advantages, applications, and the disadvantages for a clear comparison between the existing methods.

Table 1.1 2D and 3D approaches for enhanced graphene properties

Configuration	Type	Materials	Advantages	Application	Disadvantages
Nanoribbons	2D	Pure graphene	Strong edge scattering, direct SPP	Optical and electronic devices	Low tunability, Substrate coupling effects
Nanodisks	2D	Pure graphene	30% stronger absorption	IR Plasmonic biosensors	Diffusion-limited sensing
Tapered triangles	2D	Pure graphene	20 times higher tip confinement	Adsorbed molecule at tip - sensing	Limited spatial coverage and point sensing.
Nanogap plasmons	2D	Graphene-dielectric array	Large surface-area coverage	Waveguide, sensing	Low quality factor spectra
Acoustic plasmons	2.5D	Graphene-metal-dielectric	Perfect 100% absorption	IR molecular spectroscopy	Low near-field enhancement
Linear stacks	3D	Graphene-insulator-graphene	High tunability of plasmon resonance	Antenna and communication devices	Low sensitivity and figure of merit
Porous scaffold	3D	Graphene oxide, graphene composites	Rapid mass transfer and catalysis	Energy storage & conversion	Low 2D Raman band, high defect count
Templated structures	3D	Graphene-metal or graphene-insulator hybrid materials	Low substrate coupling, UV enhancement of 10^{10}	Photodetectors, modulators, and polarizers	Lower doping tunability, No-uniform, high stress.
Corrugated wrinkles	3D	Pure graphene	Chemical reactivity, large plasmon reflections	Tunable dampers for communication devices	Short plasmon propagation length, difficult integration.
Nano and Micro Bubbles	3D	Pure graphene	Plasmon hotspot inside the bubble	Adaptive-focus lenses, artificial skin	High pressure inside bubble, injection of molecules.
Art-inspired Kirigami	2D-3D	Pure graphene	10 times more stretchable, negative cond.	Coupled quantum dot arrays	Hard to integrate and maintain
Art-inspired Origami	2D-3D	Pure graphene, graphene -SU8, graphene-glass, graphene oxide	Spin-orbit interaction, nonlinear resistance	Programmable robots, FET, spintronics	Microscale or larger, low uniformity & predictability

Chapter 2

Three-dimensional Coupling in Self-Assembled Metamaterials

2.1 Limitations of existing 3D graphene technologies

The previous chapter established some of the unique advantages and applications of 3D graphene structures but also revealed some of their disadvantages. The linear stacks of graphene show a high detection accuracy but suffer from a corresponding lower sensitivity and figure of merit (FOM). Moreover, graphene foams, aerogels, and other scaffolded structure cannot be fabricated out of pristine graphene and are usually composite structures with a high defect density where plasmon resonance cannot be induced. The pure graphene structures forming the graphene nanorods, wrinkles, and bubbles where the plasmon resonance can be induced still suffer from short plasmon propagation lengths with a low quality-factor (Q-factor) of resonance, non-uniformity and high stress in their geometry, and lower tunability of their

plasmon wavelength. The plasmon hotspots in each of these 3D structures are not rapidly accessible by the targeted molecules due to the impermeability of graphene while the fabrication processes place stringent requirements on alignment and the underlying substrates.

The 3D configurations have demonstrated an ability to overcome some of the conventional limitations in 2D graphene structures, but they also come with their own set of severe drawbacks for plasmonic vibrational spectroscopy applications. The art-inspired graphene origami is perhaps one of the ideal candidates for further development of 3D graphene, but the current microscale forms do not reveal anything about the optical and electronic properties of graphene. Recently, these origami-inspired approaches have evolved from millimeter (mm) to nanometer (nm) scale into self-assembled polyhedral metamaterials and mass spectrometers especially suited for tri-axial sensing technologies [131,132]. In this chapter, we detail how the three-dimensional coupling in such self-assembled structures can reveal new optical phenomena and achieve unique advantages for device applications.

2.2 Advantages of 3D sensing through self-assembled polyhedrons

The vast potential of the emerging 3D sensing technologies across a wide range of industries has prompted a desire to realize single devices with full 3D awareness. The development for a lot of these 3D devices has followed cues from 3D sensors already existing in the five human sensory organs that allow humans to see, hear, feel, smell, and taste as well as equally developed and even far superior forms in the plant and animal kingdom [133]. 3D-structured sensors, compared to the 1D or 2D, inherently offer unique, advantageous spatial sensing capabilities in the directional measurements and the positioning of sensing source. While a cubic arrangement is utilized as the predominant structure in 3D sensing systems, we are not limited to a cubic arrangement when constructing 3D sensors. Non-polyhedral, 3D-structured can have a partial spatial coverage in terms of sensing capability with restriction mainly resulting from the fact that their 3D-structured sensing components are bounded on a substrate or noncubic surface [134-137].

The 3D polyhedral sensors form an ideal platform to measure 3D spatial information in a 3D space (Figure 2.1a). The polyhedrons enable simultaneously probing of the displacement in position, orientation, and

directional information in the Cartesian coordinate system. Their fabrication as free-standing sensors separated from the substrates allows them full spatial sensing coverage, which otherwise cannot be achieved in other bound 3D sensors. Unlike macroscale sensors, novel fabrication strategies (origami-inspired self-folding, Figure 2.1b) are required to realize the sub-millimeter-sized cubic sensors [138-140]. The fabrication of orthogonally aligned 3D sensors is especially attractive through the origami procedure due to the simplification of the conventional multistep fabrication procedures such as layer-by-layer lithographic patterning and monolithic integrations. One class of these 3D sensors stems from 3D transformation of traditionally 2D split-ring resonator (SRR)-based metamaterials. In the following section, we explain the properties of SRRs that have attracted so much attention and the need for their 3D transformation.

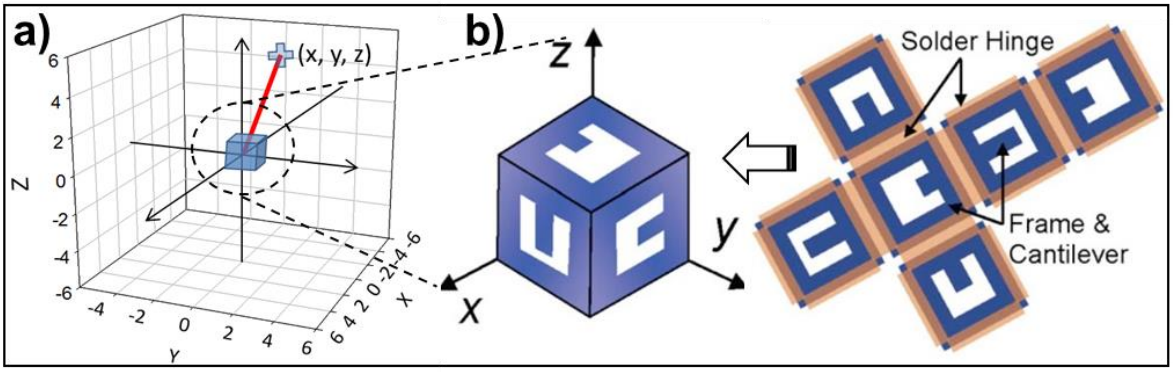

Figure 2.1 (a) Schematic of a 3D orthogonal sensor with triaxial sensing ability. (b) Schematic diagram of a three-axis cantilever cubic device. [133].

2.3 Properties and limitations of 2D split-ring resonator-based metamaterials

Split-ring resonator (SRR) based metamaterial structures have been extensively studied because of their relatively sharp spectral resonances as well as their ability to manipulate electromagnetic waves and produce strong confinement of the magnetic (H) field within the arms of the resonator and the electric (E) field confinement within the split. The split contributes capacitance to the resonant frequency which is directly proportional to the relative permittivity. The confinement of the E field within the capacitance-controlling split makes it a hotspot that has higher sensitivity than the surrounding areas where the electric field is much weaker. Hence, when a SRR is exposed to a biomolecule (Figure 2.2a), a large shift in resonant frequency is seen as a function of the relative permittivity of the external molecule near the split (Figure 2.2b) [141]. The dependence of the resonant frequency on the aforementioned parameters has allowed SRRs to be used in a wide range of sensors to detect microorganisms [142-144], strain [145], dielectric constants [146], and displacement [147] without the effects of ambient temperature and pressure. Especially, THz SRR-based biosensors offer an attractive avenue for the development of small-scale, label-free detectors capable of being

introduced orally or intravenously due to their microscale dimensions, which are comparable to that of most microorganisms, and the nonionizing nature of THz radiation [148,149].

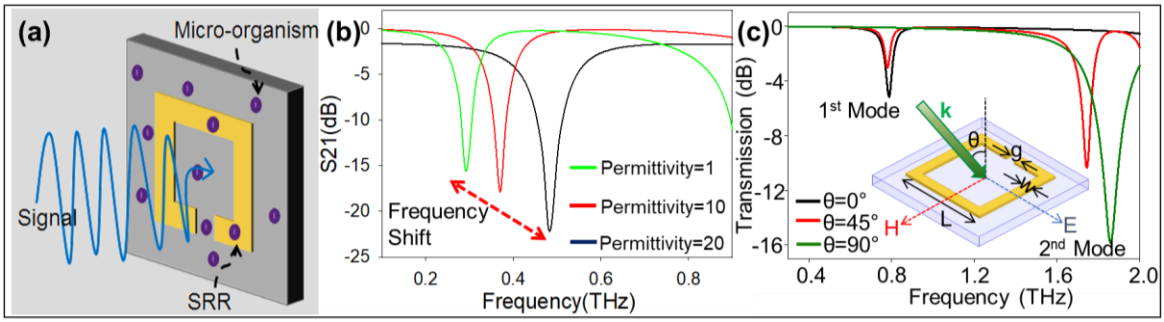

Figure 2.2 (a) Illustration of permittivity change due to microorganisms in the sample. (b) Simulated response for change in resonant frequency with permittivity of surroundings (c) Transmission characteristics of a 2D C-shaped split-ring resonator showing the angular dependence of incident THz light [155].

However, the polarization dependence of the SRR transmission response poses a major drawback. For example, when the H field is polarized perpendicular to the split-containing arm of the resonator, the structure is in first mode (magnetic resonance). However, when the E field is polarized perpendicular to the split-containing arm of the resonator, the structure is in second mode (electric resonance). As the SRR is rotated from 0° to 90°, the first mode decreases and the second mode increases (Figure 2.2c); the reverse

phenomenon takes places on rotating from 90° to 180°. The maximum first mode transmission amplitude (T_θ) achieved at $\theta = 0°$ decreases as a function of the rotation angle such that transmission, $T(\theta)$, at any angle (θ) is given by $T(\theta) = 1 – (1 – T_\theta)|\cos 2\theta|$ [150]. This presents an ambiguity in the transmission spectrum, such that variation due to the presence of external molecules cannot be discerned from the rotation of structures (SRRs), thus limiting their application as sensors when the orientation of the resonator is difficult to control such as in-vivo detection processes.

2.4 Fully Anisotropic three-dimensional SRR for triaxial optical inclinometers

Research into the simultaneous resolution of rotations across all three-dimensions has gained momentum to analyze the position and orientation of medical microbots [151] that can provide in-vivo detection, diagnosis, and drug delivery to allow fast, minimally invasive treatments. The primary tasks for these devices become the need to collect, transmit, and store a wide range of data as they traverse the body. For maximum efficiency of main circuit components in these limited space and power systems, it is necessary for the

secondary navigation components to be remotely monitored as well as to be reliable i.e. not affected by the temperature and pressure of the environment surrounding the microbots [152]. Thus, opening the route to SRR-based micro-machined angular sensors due to their environmentally invariant resonance, low on-chip power, angle-dependence of spectrum, and remote sensing capabilities.

2.4.1 Design of full anisotropy in 3D cubic SRR

When the incident wave is parallel to an SRR ($\theta_y = 90°$), a very weak resonance is observed (Figure 2.3 a,b). Using a cubic point of symmetry form a face-centered SRR lattice (Figure 2.3e) such that for any rotation a measurable transmission exists even for $\theta_y = 90°$ because at least two resonators have the incident wave perpendicular to them (Figure 2.3f). However, resonators of fixed length, L, on cubic structures do not transduce an angle variant response for 180° rotation around any axes. ($\theta°$ is not distinguishable from $\theta \pm 180°$ and $-\theta°$), such that the transmission spectrum for 30°, 150°, 210°, and 330° perfectly overlap each other (Figure 2.3 g,h). Thus, limiting the sensing range to 180° for 3D cubic SRRs.

2.4.1.1 Variable length 3D cubic SRR

One solution here is to replace the single dimension SRR with resonators of varying sizes. If there are 3 resonators of length L_1, L_2, and L_3 on each face (Figure 2.3i), there exist three different resonant frequencies for the cubic structure (Figure 2.3j). If we choose SRRs of length $L_1 = 72$ μm, $L_2 = 54$ μm and $L3 = 36$ μm resonates then their 1^{st} mode resonant frequency becomes 0.28 THz, 0.38 THz, and 0.52 THz, respectively.

This, in turn, causes a transmission where the first three peaks at different frequencies represent the fundamental (1^{st} mode) resonance of each resonator and the amplitude of each of the three peaks can give the angle of rotation. For such a cubic SRR, angle θ° is distinguishable from $\theta \pm 180°$ and -θ° such that the transmission spectra for 30°, 150°, 210°, and 330° are visibly different from each other (Figure 2.3k). However, their sensing range remains limited to 180° as the resonators give the same response for rotations of angle 0° and 180° along any axis (Figure 2.3l). Hence, the cubic inclinometer with resonators of varying length can sense rotations from 0-360° about all three-axes except for the special case where $\theta_x = \theta_y = \theta_z = 180°$.

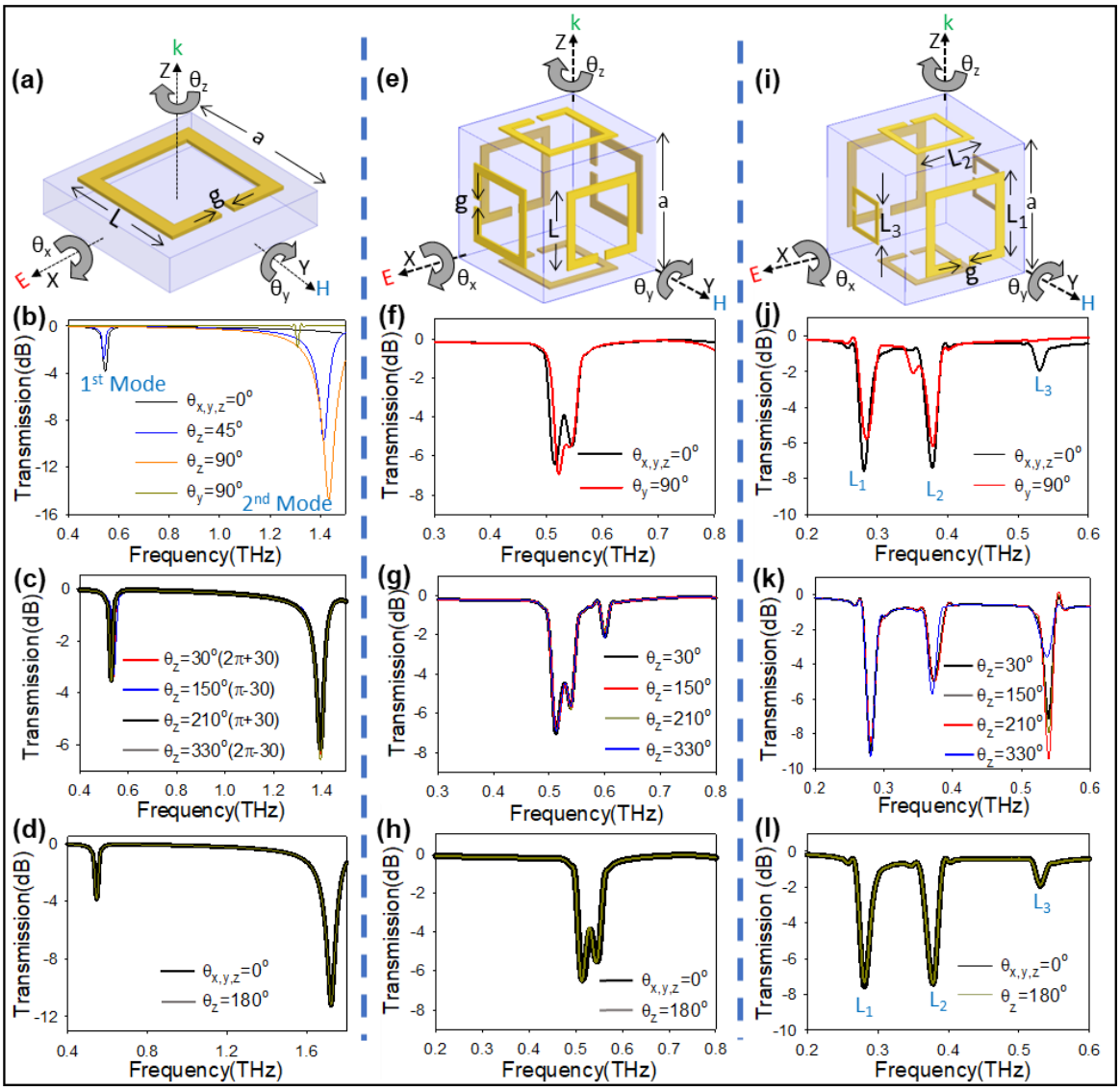

Figure 2.3 Illustration of two- and three-dimensional split-ring resonators (SRRs) and their simulated transmission response. (a) A conventional, two-dimensional SRR with L = 36 μm, g = 4 μm, and a = 48 μm, that can be rotated along the X-, Y-, and Z-axis at angles θ_x, θ_y, θ_z degrees, respectively. (b) The weak transmission observed when rotated about Y-axis (θ_y) as opposed to the strong first mode ($\theta = 0°$) and second mode ($\theta_z = 90°$) (c) Overlap of the first

resonance at 0.52 THz for rotations of 30°, 150°, 210°, and 330° about the Z-axis. (d) Transmission for the initial position ($\theta = 0°$) and ($\theta_z = 180°$), with isotropy for any angle θ and $n\pi \pm \theta$ ($n = 1, 2$). (e) A cubic three-dimensional split ring resonator with $L = 36\ \mu m$, $g = 4\ \mu m$, and $a = 110\ \mu m$, capable of maintaining a high signal to noise ratio (SNR) when rotated along all three-axes. (f–h) Simulated transmission response of the cube showing, (f) the high but ambiguous transmission response when rotated about Y-axis, (g) an isotropic transmission response for any angle θ and $n\pi \pm \theta$ ($n = 1, 2$) similar to the 2-D resonator, and (h) perfect overlap of the transmission at 0° and 180°. (i) A cubic rotation sensor with varying resonator length along each axis with $L_1 = 72\ \mu m$, $L_2 = 54\ \mu m$ and $L_3 = 36\ \mu m$ while 'g' and 'a' are kept constant as before. (j–l) Simulated transmission response of the cube showing, (j) the ability of the cube to maintain the high transmission for Y-axis rotation, (k) significant changes in transmission between rotations of angle θ, and $n\pi \pm \theta$ ($n = 1, 2$), and (l) special case of a 180° rotation that perfectly overlaps the $\theta = 0°$ initial position [153].

2.4.1.2 Variable angular offset in cubic 3D SRR

To extend the sensing range, it is necessary to break the 180° symmetry in the transmission response for at least one of the resonators, such that the entire cube loses its 180° isotropy. A solution here is to individually tilt each of the resonators about their axis so L_1, L_2, and L_3 are now tilted at angles β_y, β_z, β_x, respectively (Figure 2.4a) causing a change in their transmission amplitude. It can be clearly seen that two resonators (L_2 and L_3) demonstrate a period of 180° (Figure 2.4b), whereas the L_1 resonator does not demonstrate any symmetry in its transmission amplitude. For respective Z- and X-axis rotations of $L_2 = 54$ μm and $L_3 = 36$ μm (β_z and β_x increase), the first mode amplitude decreases till of 90° and increases beyond it due to a transition from first mode to second mode when tilted from 0° to 90° and vice-versa from 90° to 180°. L_3 resonator has the incident wave (k) parallel to the plane of the resonator causing a lower transmission amplitude. The resonator with $L_1 = 72$ μm defined along the Y-axis is also parallel to the incident wave, but the resonator (L_1) undergoes a resonance condition with the plane of the magnetic field (H) lying parallel to the plane of the resonator. This polarization produces strong electrical and magnetic resonances within the SRR at its fundamental resonant frequencies but without the conventional 180-degree period. The electrical resonance disappears only for $\beta_z = 0°$, whereas the

magnetic resonance never reaches 0 dB. For all increments of β_y from 0° to 200°, a resonance amplitude ranging from 10 to 4 dB was seen for the 1st mode of the L_1 resonator.

The electrical resonance (second mode) of the L_1 resonator occurs at 0.52 THz, same as the magnetic (first mode) resonance for the $L_3 = 36$ μm resonator. The transmission amplitude at 0.52 THz is thus a superimposition of these two individual waveforms, the resonators cannot be called as coupled since they continue to resonate at their individual resonant frequencies as in the absence of the other. This superimposition of the waveforms enhances the ability of the cubic structure to distinguish angles for all values of θ and ($n\pi \pm \theta$, $n = 1,2$) except for $\theta x,y,z = 0°$ (0° and 180°), where the electrical resonance (2nd mode) for the L_1 resonator goes to zero. Only at $\beta_y = 0°$, 180°, the transmission amplitude of the resonator (L_1) with the magnetic field plane lying parallel to the plane of the resonator demonstrates a change of 1.2 (dB), a small change that gets easily masked by the smallest coupling with the L_2 and L_3 resonators, forcing the perfect overlap of the transmission response for $\theta x,y,z = 0°$, and $\theta z = 180°$.

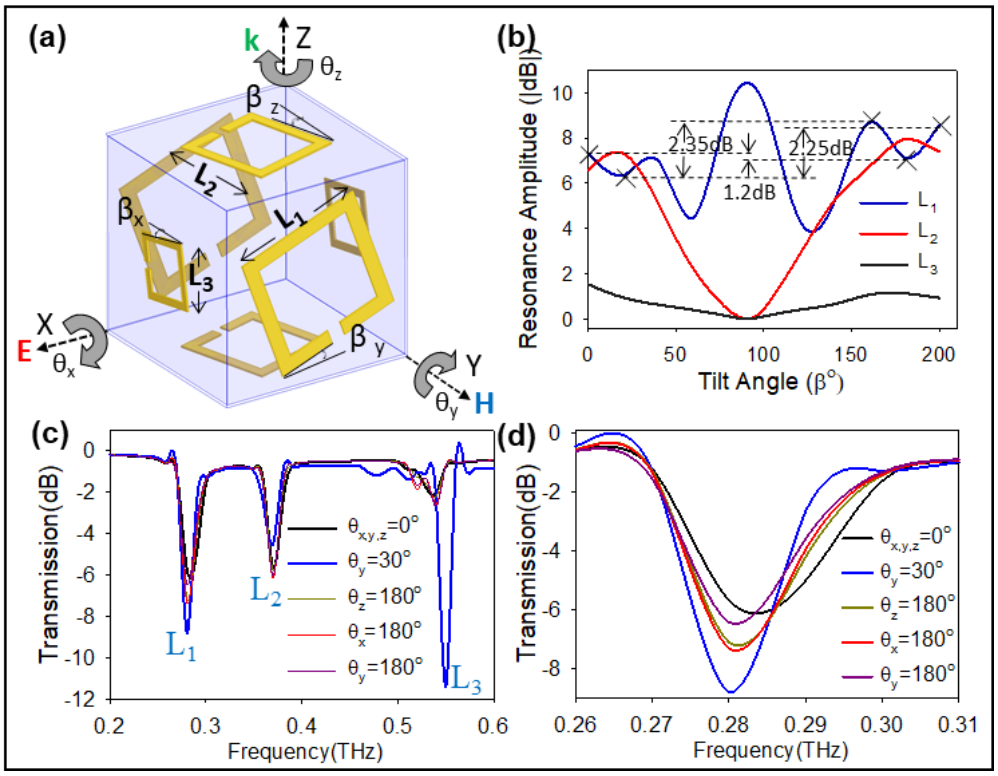

Figure 2.4 Effect of the angular offset on the anisotropy of the 3D inclinometer. (a) Cubic rotation sensor with an angular offset of β_x, β_y, and β_z for each resonator L_3, L_1 and L_2, respectively. (b-d) simulation results for the cubic sensor. (b) The variation in the first mode resonance strength as a function of the angular offset obtained by placing only 1 of the 3 resonators at a single time to avoid couplings; L_2 and L_3 have a 180° period but the L_1 resonator has no symmetry in its transmission (c) Graph showing the anisotropic effect of adding angular offset; the resonator L_1 demonstrates a significant change in amplitude for a 180° rotation about any axis. (d) Zoomed in graph of (c) showing the variance in transmission of the L_1 resonator [153].

If the resonator is now tilted by an angle of β_y then, on an 180° rotation of the cube around the Y-axis from the initial position, the total rotation experienced by the L_1 resonator changes. If $\beta_y = 20°$ at the initial position, then on rotating the cube by $\theta_y = 180°$), the effective angle of the L_1 resonator changes to 200° configuration with a change in transmission of 2.25 dB between 20° and 200°. Similarly, when the cube is rotated by 180° along the X-axis ($\theta_x = 180°$), the L_1 resonator with $\beta_y = 20°$ initially, it now experiences an angle of 160° configuration causing a total change of 140° corresponding to a change of 2.35 dB change in the transmission amplitude between the two configurations. Similarly, a 180° rotation about the Z-axis ($\theta_z = 180°$) causes a 320° change in the position for the L_1 resonator that causes a 5.45 dB change in the transmission amplitude [153]. It could be argued that for a rotation of $\theta_y = -20°$, and $\theta_y = 160°$, the cubic structure will once again reach the non-tilted structure resulting in the original $\beta_y = 0°$ and 180° configurations, respectively.

However, when tilted about the Y-axis at $\beta_y = 20°$, the coupling of the L_1 resonator with L_2 and L_3 changes, such that the small difference previously seen in the transmission response of the L_1 resonator between $\beta_y = 0°$ and 180° positions is no longer masked by the coupling with L_2 and L_3 resonators, leading to a distinguishable amplitude difference of 2.66 dB between $\theta_y = -20°$, and $\theta_y = 160°$, overcoming any ambiguity in the transmission response (Figure

2.4c,d). Each resonator is tilted about its axis to respond to all the polarization directions of the light with tilt angles (βx, βy, βz) chosen to maximize transmission at initial cube position of $\theta x,y,z = 0°$.

2.4.1.3 Full 360-degree sensing range in cubic 3D SRRs

Following the addition of the angular offset,180° isotropic limitation of the SRRs can be overcome to resolve rotations of any angle θ about various axes and even for angles $180 \pm \theta°$. When the resonator is rotated from the initial position by an angle of $\theta_z = 180°$, the L_1 resonator shows a large change in the transmission amplitude, whereas the L_2 and L_3 resonators retain their initial transmission. While for rotation along the Y-axis (θ_y) by a random angle, the resonators L_2 and L_3 demonstrate a large change in the transmission amplitude (Figure 2.4c). A lower change is seen (~2 dB) for the transmission amplitude of the L_1 resonator (Figure 2.4d) on 180° rotations than previously discussed (2.25 to 5 dB) due to the minor coupling between the planar resonators on each cubic face, which attempts to mask change in L_1 transmission.

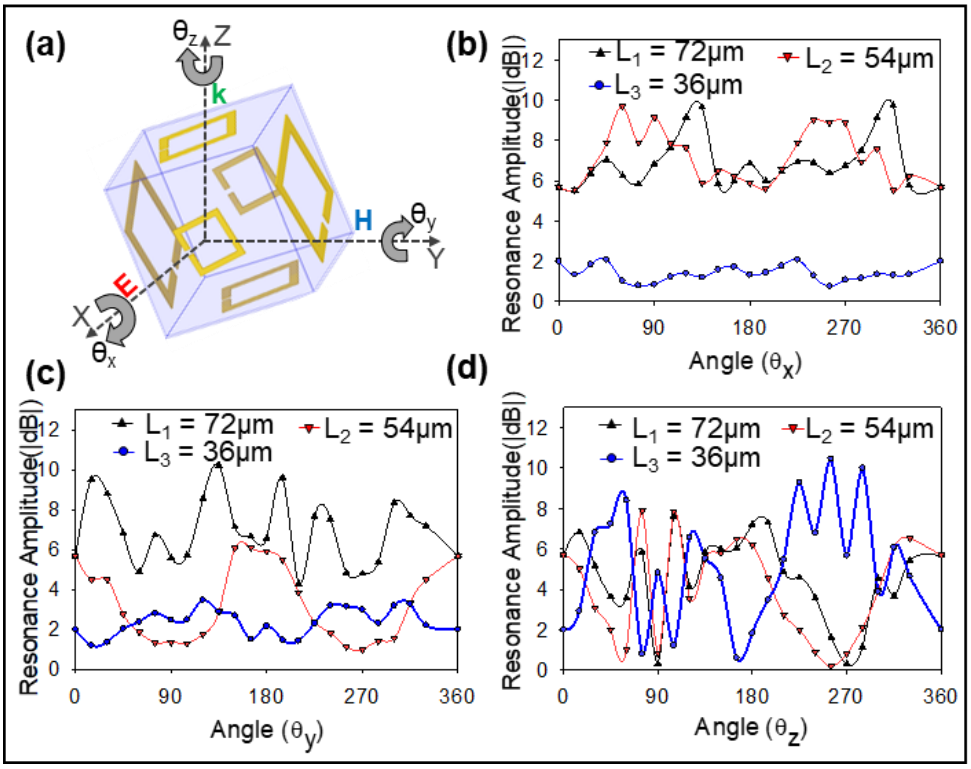

Figure 2.5 Simulation results for the rotation of the 3D cube. (a) Cubic inclinometer rotated about X-, Y-, and Z-axis at angles θ_x, θ_y, and θ_z, respectively. Variation in resonance strength of each resonator obtained by simulating rotations along (b) X-axis, (c) Y-axis, (d) Z-axis in steps of 15° from 0-360° proving that for no two angles do the values of all three resonators overlap each other. The resonance amplitudes are obtained at the resonant frequencies of the L_1 (0.28 THz), L_2 (0.32 THz), and L_3 (0.52 THz) resonators [153].

The cubic sensor can be along each axis to form angles θx, θy, and θz along the X-, Y-, and Z- axes (Figure 2.5a). Rotations of 0° to 360° in steps of

15° are performed from along X- (Figure 2.5b), Y- (Figure 2.5c), and Z-axis (Figure 2.5d) with magnitude of the transmission peaks measured at 0.28, 0.32, and 0.52 THz. The transmission amplitudes of all the resonators can be calibrated to resolve the rotation angle. The simulated transmission amplitude of all three resonators does not show the exact same value for any two rotation angles about X-, Y- or Z-axis, thus removing any ambiguity in the measurement of the angle of rotation of the cubic sensor. The SRR lengths were chosen as 72 μm, 54 μm, and 36 μm since their 1st mode resonance does not spectrally overlap. Distinct values need to be given for the three tilt angles to break the 180° coupling symmetry; thus, resonators 72 μm, 54 μm, and 36 μm were tilted at angles $\beta y = 20°$, $\beta z = 15°$, and $\beta x = 10°$ about their axis, respectively. The lowest tilt angle ($\beta x = 10°$) was assigned to the L_3 SRR since at the initial position of the cube it has the lowest transmission amplitude of the 3 SRRs and decreases further with increasing tilt angle. For the L_2 SRR, the transmission amplitude increases between 0°-20°. However, if we choose 20° as the tilt angle for the L_2 SRR, then the L_1 SRR would need to be 25–30° which will reduce its transmission amplitude significantly and due to its large dimension will make it difficult to accommodate on the face of the cube with a periodicity similar to the L_2 and L_3 SRR. Thus, the tilt angle of 15° was chosen for L_2 SRR and a tilt angle of 20° for L_1 SRR.

2.4.2 Fabrication of cubic SRR inclinometers

One important fabrication requirement is for any additional components apart from the SRR (e.g. the cube) to be transparent within the frequency range. The 500 μm sized cube with tilted SRRs was fabricated using a self-assembly process [154]. The 300 nm thick gold (Au) SRRs were patterned on a cubic surface with SU-8 2010 (MicroChem) panels and SPR 220–7.0 (MEGAPOSIT) hinges. On top of the electroplated Au SRRs, 10 μm thick SU-8 panels and 21 μm thick hinges for the cube of SPR 220–7.0 positive photoresist are patterned. The 2D structure before self-assembly consists of six SU-8 panels, Au SRR arrays on each face of the panel, and SPR 220 polymer hinges (Figure 2.6a). The SPR 220 hinges to reflow under high temperature and generate a surface tension force that triggers the self-assembly to fold the structure (Figure 2.6b). On cooling, the SPR 220 hinges became solid again and secured the 3D cubic structure (Figure 2.6c). The fabrication process has two advantages, first, only the Au SRR is present as the resonant material (Figure 2.6d). Second, the entirely polymeric composition of the cube ensures that no noise or coupling of the SRRs to the cube frame can distort the spectrum. Following the reflow of the SPR 220 polymer hinge, the 2D net

forms the 3D cubic structure (Figure 2.6e), with two faces containing a 5 × 5 array of 72 μm (tilted at 20°), two faces containing a 6 × 6 array of 54 μm (tilted at 15°), and two faces containing a 9 × 9 array of 54 μm (tilted at 10°) Au SRRs on the outside of the cube. Through uniform heating, the 2D planar structures can be folded uniformly by a surface tension force generated by the hinge material into 3D cubic structures within several seconds to a few minutes depending on the temperature applied to the hinges. The resulting cubic structure is mechanically and thermally stable under 100 °C (the melting point of the re-solidified polymer hinges).

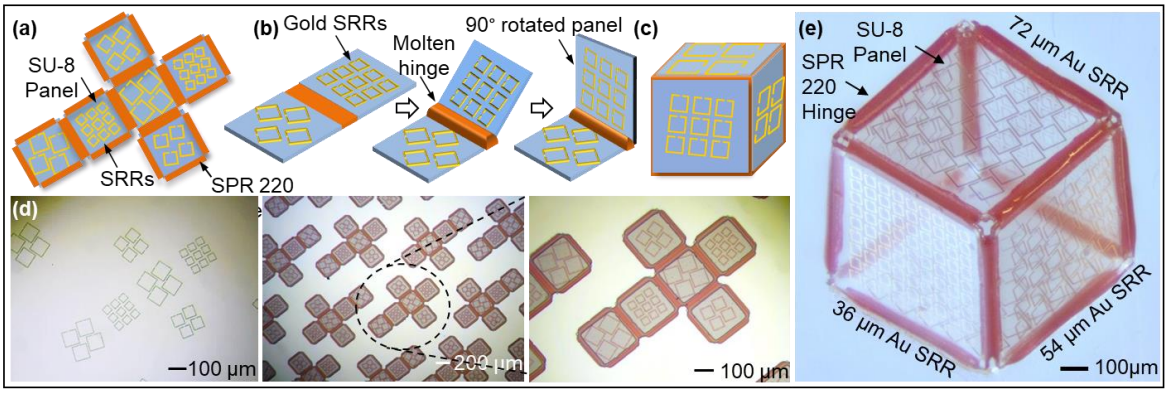

Figure 2.6 Fabrication process for the Triaxial inclinometer. (a) Illustration of the two-dimensional planar configuration before the self-folding is initiated, showing the SU-8 panels, the Au SRRs and the SPR 220 hinges (b) Illustration of the self-folding process, demonstrating the melting of the hinge causing it to flow and generating a surface tension force that slowly lifts up and folds the panel to a 90° angle (c) Illustration of the folded 3D cubic structure through

surface tension driven self-assembly, where the SU-8 panels form the faces of the cube once the hinges re-solidify (d) Optical images of the fabrication process for the cubic SRR inclinometer, starting with the patterning of Au SRRs, followed by the deposition of SU-8 panels and the SPR 220 hinges. (e) Optical Image of the 500 μm three-dimensional cubic inclinometer consisting of 5×5 array of 72 μm resonators (tilted at 20°), 6×6 array of 54 μm resonators (tilted at 15°), and 9×9 array of 36μm resonators (tilted at 10°). Resonators on the opposite faces are identical. [153].

2.4.3 THz spectroscopy of cubic SRR inclinometers

The sensor was characterized using terahertz time-domain spectroscopy (TDS) (0.2 THz to 0.8 THz). A single cube was attached to a piece of double-sided Scotch Tape (material transparent to THz wave) and was placed at the center of a circular aluminum aperture of diameter 3.8 mm (Figure 2.7a). A THz pulse generated from a commercial GaAs emitter passed through the aperture and cube and was received by a detector. The cube was placed such that at the initial position, the face of the cube with resonators of length 72 μm and resonant frequency 0.33 THz faces the incoming light. The aperture of diameter 3.8 mm generates a cutoff frequency of 0.07 THz which results in

maximum transmission drops of 0.8 at the initial 0° position (Figure 2.7b). The measured transmission response has the same 3 resonant frequencies representing each resonator as the simulated spectrum. The cube was attached to a rotational mount so that the rotation of the cube along Z-axis could be precisely controlled. Rotations performed for randomly chosen angles show the ability of the cube to distinguish between various angles. On rotating the cube by an angle of 180°, the transmission amplitude changes (Figure 2.7c). The cube demonstrated a large change in transmission amplitude for at least one or more resonators on random rotations (Figure 2.7d). The cube was rotated in steps of 20° from 0° to 360° and the transmission amplitude of each of the resonators at their resonant frequency was plotted with respect to the angle of rotation (Figure 2.7e). The amplitude of each resonator varies under rotation with no complete overlap. Thus, by finding the amplitude of all three peaks, the angle of rotation can be detected.

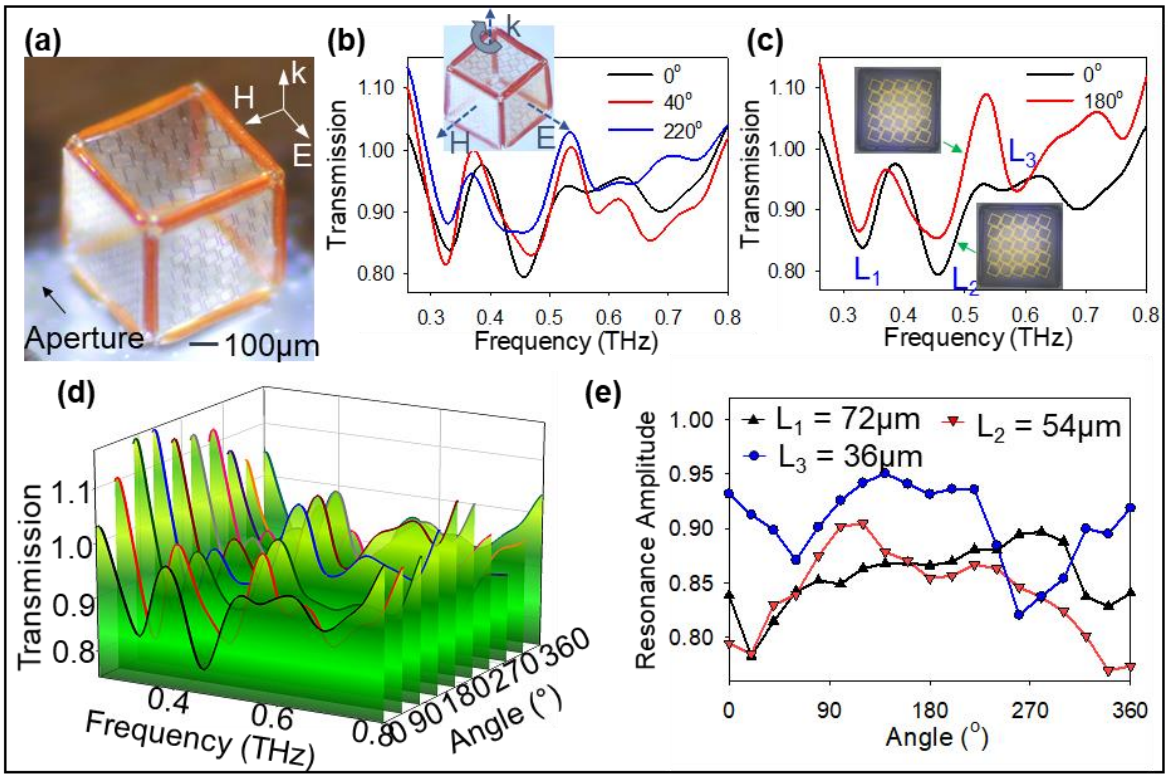

Figure 2.7 THz TDS measurement results for the cubic inclinometer. (a) Optical image of the experimental setup. (b) Measured transmission response demonstrating a clear change in transmission and breaking of the 180° isotropy of the cube. (c) Measured transmission response displaying the ability of the cube to distinguish various angles when rotated about any axis through a change in transmission. (d) Measured frequency spectra of the cubic structure observed while rotating the cube about the direction of wave vector (k) in steps of 40° (e) Measured variation in the transmission response at the fundamental resonant frequency of the 3 resonators defined on the faces of a cube when rotated along the wave vector (k). [153]

2.5 Fully isotropic octagram split-ring resonators

In the previous sections, we discussed the need to avoid the ambiguity in SRR transmission response from the angle variance when applying them for biological sensing. In this section, the design of an angle invariant SRR is detailed along with its fabrication and measurement.

2.5.1 Design of Octagram SRR for full isotropy

2.5.1.1 C-shaped and Symmetric SRR structures

As explained in the previous section, a 2D conventional SRR can never deliver a perfect overlap or perfect disorder. A step forward is superimposition in a unit cell with four resonators (Figure 2.8a) where two of them (SRR1 and SRR3) have a magnetic field perpendicular to the gap (first mode), while the other two (SRR2 and SRR4) have an electric field perpendicular to the gap (second mode). In such a configuration, during rotations of the structure about the z-axis, decrease in first mode resonance of SRR1 will be compensated by a proportional increase in the first mode for SRR2 and vice versa for the second mode as well. SRR3 and SRR4 ensure that the resonators within the unit cell

couple equally in all directions. While this configuration corrects for z-axis rotations, other issues arise when 3D rotations of the SRR substrate are applied; the first mode resonance shows a large change in the resonant frequency, as well as the transmission amplitude (Figure 2.8b). Therefore, the 2D SRR structures even with varying orientations within a unit cell cannot provide a three-dimensionally isotropic transmission response.

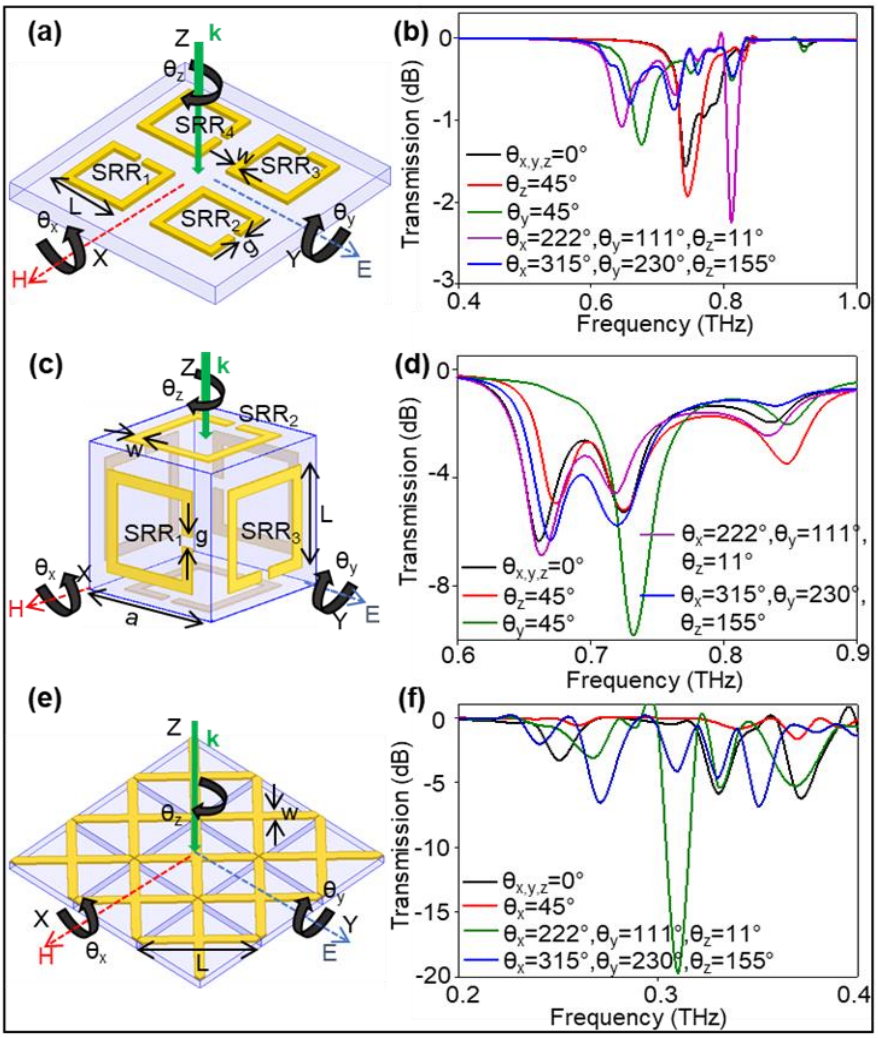

Figure 2.8 2D and 3D coupled SRRs that can be subjected to 3D rotations consisting of (a, b) a 2D array of SRRs demonstrating simultaneous first and

second modes and an anisotropic response for 3D rotations. (c, d) a 3D cube that is structurally invariant for 90° rotations. (e, f) Symmetric two-dimensionally coupled resonators with the unit cell consisting of a 3 × 3 array of X-shaped symmetric resonators. [155]

Even for 3D cubic SRRs (Figure 2.8c), the splits continue to be two-dimensional; this induces nonuniform coupling between the resonators on different faces, resulting in multiple resonance behaviors (Figure 2.8d). In each SRR, the resonant arms containing the split couple strongly to their neighbors owing to the electric field confined within the split. For the cube shown in Figure 2.1c, at the initial position and for rotations about any axes (θ_x, θ_y, or θ_z), a total of two resonators always have the split perpendicular to the direction of the E and H vectors or the wave vector (k) and hence could keep the overall superimposed transmission response invariant for some specific rotation angles. For instance, at θ_y=45°, the structure shows a large shift in first mode resonant frequency as well as the transmission amplitude. This large difference in amplitude between θ_y=0° and 45° can be attributed to the change in the resonance of the SRR1 resonator. At the initial position (θ_y = 0°), SRR1 has the E field perpendicular to the split of the SRR and the incident light parallel to the plane of the resonator, giving it a weaker second mode resonance than if

the light was incident perpendicular to the plane of the resonator. SRR2 and SRR3 have first mode resonance at the initial position; however, since SRR3 has the E field perpendicular to the plane of the resonator and the incident light parallel to the SRR plane, it does not produce any significant resonance. On rotating the cube (θ_y = 45°), the incident light is not completely parallel to SRR1 any longer; thus, it undergoes a stronger second mode resonance, causing an increase in the transmission amplitude. Similarly, SRR3 also undergoes a stronger first mode resonance at θ_y = 45° than at the initial position. For the standalone case a proportional decrease in the first mode resonance of SRR2 should have been seen, thereby keeping the total transmission response constant. However, due to the presence of four SRRs with strong E field within their split at the first mode resonance in close proximity to each other, there exists a strong coupling between them, resulting in an anisotropic resonance behavior.

Symmetric resonators that minimize the switching between the first and second modes of the 2D C-shaped SRRs and compensate for the nonuniform coupling to their neighbors can overcome these limitations. To realize a symmetric array of resonators, an X-shaped configuration on a planar substrate can be considered. Due to the shape dispersing in multiple directions, the resonator at the center of the unit cell couples equally in all directions in the

XY plane (Figure 2.8e). However, the resonator at the edges can only couple to half as many resonators since the resonators at the edges have fewer neighbors than the resonators at the center. This produces multiple transmission drops (Figure 2.8f) corresponding to the resonance of each SRR within the unit cell. The first drop corresponds to the resonance of the SRR at the center of the unit cell as seen by the strong surface current for the center SRR at 0.25 THz. The peaks at higher frequency correspond to the edge and corner SRRs, giving them a higher surface current at a frequency of 0.64 THz. When the 2D non-uniformly coupled cell is rotated along any direction, the transmission response is rendered incomprehensible due to the multiple resonances. Similar results are obtained for the 2D unit cell consisting of nine partially symmetric C-shaped SRRs.

2.5.1.2 3D coupling in octagram resonators

Some of the design considerations become uniform neighbor coupling and minimization of the switching between SRR modes. Folding the symmetric SRR 2D unit cell into a 3D cube consisting of six faces with resonators on each face forces them to couple to their neighbor through the split created at the corner of the cube (Figure 2.9a), thus forming a fully

symmetric eight-pointed 3D star (octagram). The resonator split on the top face of couples equally in all directions to the resonators on the side walls of the cube, which in turn couple to the resonator on the bottom face. A strong uniform coupling between the segments on each face of the cube at the split causes a high field concentration at the corners. Since the split and resonators couplings are three-dimensional and orthogonal, it is equally affected by the E, H, and k vectors for all orientations of the cube. Thus, the 3D split gives an isotropic transmission response at 0.13 THz and with an angle invariant transmission amplitude (Figure 2.9b) and strong surface currents on all the cubic faces.

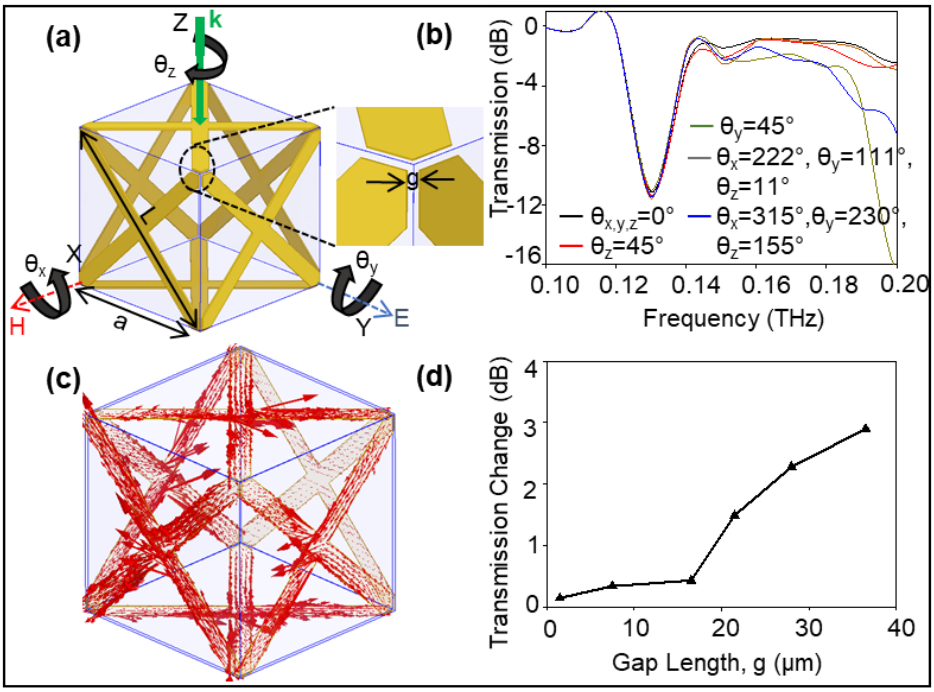

Figure 2.9 (a) Isotropic frequency surface composed of a 3D Au OSRR on an SU-8 cube of length (b) Single isotropic transmission peak at 0.13 THz for the

500 μm cube which is invariant for any rotations of any angle about the x-, y-, and z-axis. (c) Uniform current distribution of the 3D coupled resonator on the faces of the cube with the arrows showing the direction of the surface current. (d) Graph of maximum change in transmission seen between the initial position and the angles in part (b) as a function of the split gap length in the OSRR. [155]

Each segment in the OSRR induces resonance in its neighbor, creating a surface current on the entire 3D resonator surfaces. The coupling is dependent on the split gap such that at small gaps (1.5-16 μm), the strong coupling between the resonators cause the entire cube to act as a single unit with well-defined isotropic resonance (Figure 2.9d). The coupling between resonant pairs decreases as the gap increases ($g \geq 21$ μm), causing them to act as six independent anisotropic resonators. Addition of a 2D gap at the center of each face of the individual resonators of the 3D OSRR also reverts them to non-uniformly coupled anisotropic 2D resonators. Thus, a 3D OSRR with a orthogonal corner split that is equally mediated by the incident light, as well as the magnetic and the electric field polarization, creates a perfectly isotropic and well-defined transmission response [155].

2.5.1.3 Effect of 3D coupling on sensing performance

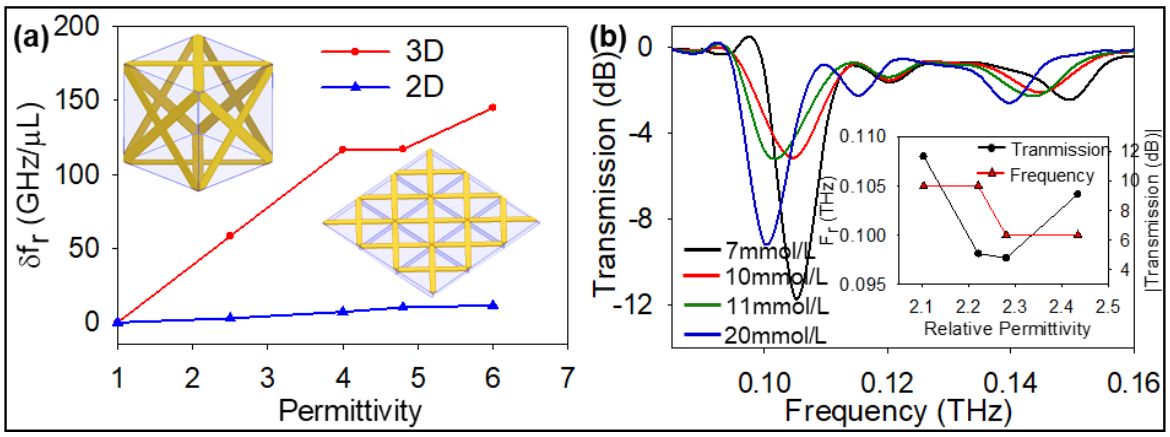

Figure 2.10 (a) Graph showing the shift in resonance per unit volume (δfr) of targeted molecules (as a function of the permittivity due to the molecules) for the 3D coupled OSRR when compared to the 2D coupled symmetric X-shaped SRR. (b) Change in transmission response of the cube due to rising glucose level evaluated at different levels (inset, showing the resonant frequency and transmission amplitude for the permittivity corresponding to each glucose level). [155]

The resonant frequency, $f_r = 1/(LC)^{0.5}$ changes proportionally to the relative permittivity (ϵ_r) of the biomolecule being detected (where L is the inductance due to the gold resonant structure and C is the capacitance of the 2D/3D splits). The permittivity corresponds to any changes in the exposed biomolecule with simulations carried out for free-space permittivity from 1 to

6. For a 2D array of SRRs with small volumes of a target molecule, only one of the resonators may demonstrate a change in resonance, which cannot change the overall transmission response. The strong neighbor couplings in 3D OSRR cause a domino reaction, providing the isotropic 3D coupled OSRR with a much higher sensitivity than the corresponding 2D coupled SRR. This results in small permittivity changes ($\Delta\epsilon_r = 6$) having 10-25 times higher frequency shift for the 3D OSRR as compared to the 2D planar SRR (Figure 2.10a).

To monitor small molecular changes, the detection ability of the 3D OSRR structure was assessed for smaller variations in permittivity (maximum $\Delta\epsilon_r \approx 0.35$). One such example is the monitoring of rising levels of glucose in the blood. Glucose was chosen as an example to assess the performance of the OSRR due to the widely established relationship between refractive index and concentration of glucose in blood [156]. Three are three levels of interest: first, the baseline level before eating (fasting); second, the level after eating that most humans temporarily undergo; third, the critical level, which can result in adverse consequences if not treated immediately. The corresponding maximum change in relative permittivity for the three levels between 7 and 20 mmol/L is only 0.35. At fasting, glucose level is 7 mmol/L and $\epsilon_r = 2.1025$, the resonant frequency of a 3D OSRR was 0.105 THz. After eating level is 10–11 mmol/L and the relative permittivity $\epsilon_r = 2.28$, shifting the resonant frequency

to f_r = 0.100 THz (Δfr = 0.005 THz). The resonant frequency appears to remain constant between 7 and 10 mmol/L and between 11 and 20 mmol/L, representing the relative permittivity range 2.1-2.45 (Figure 2.10b). The actual change in resonant frequency between the concentrations of 7 and 10 mmol/L is 0.002 THz but the spectral resolution for most THz TDS systems is limited to 0.005 THz, making the resonant frequency appear to be constant.

The permittivity change between 7 and 10 mmol/L is accompanied by a transmission change of ~6.6 dB. The small shift (0.002 THz) in the position of the peak maxima causes the large change in amplitude, which subsequently modifies the amplitude at the previous resonant frequency (~5.9 dB change). A similar phenomenon occurs when the concentration increases from 11 mmol/L to 20 mmol/L. In contrast, under similar conditions the 2D array would not be able to transduce any reliable signal since the amplitude change could also be attributed to a change in orientation of the structure. The isotropic nature of the 3D OSRR means that for large changes in permittivity the resonant frequency can be monitored for the detection of the molecules, but even for smaller changes in permittivity that cannot cause a shift in resonant frequency, the amplitude can also be monitored since there are no other parameters except substances around resonators that can cause it to change. Thus, the 3D OSRR with a polarization-invariant isotropic transmission has a

large detection range including large changes in the composition of the substance (permittivity) producing a change in resonant frequency and smaller changes in the targeted substance causing a change in transmission.

2.5.2 Fabrication of octagram SRRs

The self-assembly process described previously can also be used to realize the isotropic resonators. A 10 nm chromium (Cr) adhesion layer followed by a 300 nm thick copper (Cu) layer was deposited using electron beam evaporation on a silicon (Si) ⟨100⟩ wafer. The Cu layer acts as a sacrificial layer, as well as a seed layer for a subsequent electroplating process used for depositing 300 nm thick Au OSRR. Following the electroplating of the Au OSRR (Figure 2.11a), ~10 μm thick SU-8 polymer panels were spin coated and patterned via a conventional photolithography process (Figure 2.11b). Lastly, ~21 μm thick polymer hinges of SPR 220-7.0 positive photoresist were patterned between the panels (Figure 2.11c). The 2D structure was submerged in APS copper etchant 100 (Transene) for 3 hours to etch the Cu sacrificial layer and release the structure from the substrate. The released 2D structures were transferred to water and placed on a hot plate for the self-assembly process. When heat energy is applied to the 2D structure, the SPR

220 hinges melt and reflow, generating a surface tension force to fold the structure. After locking of the hinges is achieved at a folding angle of 90°, the heat source is removed. On cooling to room temperature, the SPR 220 hinges re-solidify and secure the 3D cubic structure (Figure 2.11d). Following the reflow of the SPR 220 polymer hinge, the 2D net folds into the 3D cubic structure, with each face containing the symmetric resonant segments that together form the 3D OSRR with split gap length ~2 μm on the outside of a cube with SU-8 panels.

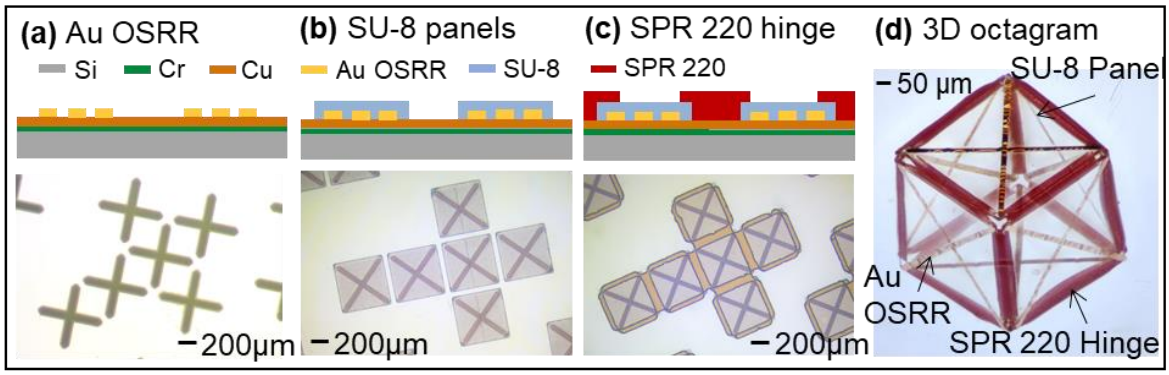

Figure 2.11 Fabrication process for the 3D OSRR. (a) Deposition of a Cr/Cu sacrificial layer by e-beam evaporation on a Si substrate followed by electroplating of 300 nm thick Au OSRR. (b) SU-8 spin coating and patterning by photolithography for the formation of panels with dimensions 500 × 500 × 10 μm. (c) SPR 220 spin coating and patterning by photolithography for 21 μm thick hinges. (d) Self-assembled 500 μm 3D cube with isotropic Au OSRR of

segment lengths 675 μm, width 20 μm, and split gap ~35 μm, patterned on SU-8 panels and folded using SPR 220 hinges. [155]

2.5.3 THz spectroscopy of octagram SRRs

THz time-domain spectroscopy (TDS) (0.1 to 1.0 THz) was performed for the cube after fixing it onto a rotational aperture with a diameter of 3 mm (Figure 2.12a). The cutoff frequency for the 3.0 mm aperture was ~0.1 THz. The normalized transmission response was found by dividing the signal received from the OSRR cube with that of a blank cube without OSRR patterns (Figure 2.12b). Except for the two positions resulting in the largest deviation, the remaining 12 measurements at different random positions were used to estimate the final value of the resonant frequency and transmission. The first mode resonance was measured using the 3 mm aperture and was found to have an average resonant frequency of 0.19 THz and transmission of 0.698. The maximum change in the first mode resonant frequency for the various values of θ_x, θ_y, and θ_z from 0° to 360° (12 different orientations) was found to be ±0.0045 THz (2.3%), whereas the corresponding maximum variation in transmission was ±0.055 (8.4%). This demonstrates the isotropic transmission response of the 3D OSRR due to the uniform coupling between the resonators

through the 3D gaps. The 2.3% change in resonant frequency and the 8.4% change in amplitude as opposed to the perfectly isotropic response of the simulated OSRR could be attributed to variation in thickness of the materials and small ripples in Au OSRR, and non-uniform boundary spacing applied by the circular aperture to the cube. The higher order modes (occurring between 0.3 and 0.5 THz) could not be observed with an aperture diameter of 3.0 mm since only 33% of the area of the aperture is covered by the cube, generating a large amount of noise to view the weaker higher order modes; however, different aperture shapes and sizes can be fabricated that allow optimal measurement of the isotropic response of higher order modes.

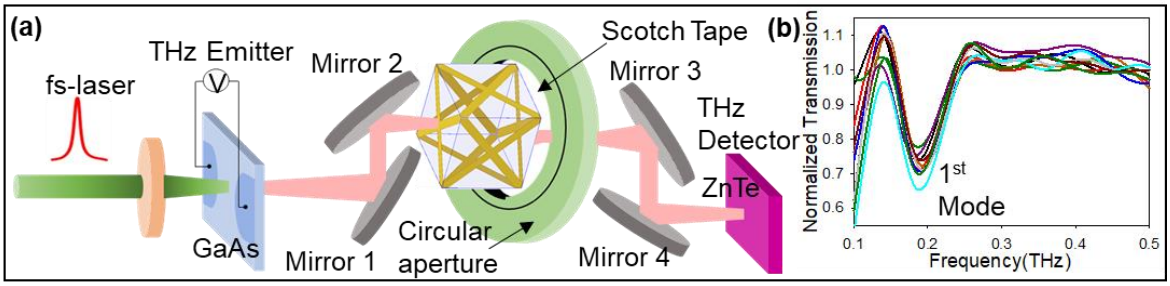

Figure 2.12 (a) Schematic of the THz time domain spectroscopy (TDS) setup showing the GaAs THz emitter and the ZnTe detector. (b) Transmission characteristic of the 3D OSRR measured by THz TDS while rotating the aperture and cube along the angle θ_z using circular apertures of diameter 3 mm. [155]

2.6 Orthogonal coupling and nanomaterials

The previous sections detailed the benefits of orthogonal 3D coupling in SRR-based materials. The specific design of the coupling mechanisms can deliver both isotropic and anisotropic metamaterials that find a large range of applications. In these 3D metamaterials, while the design of the active resonant materials was given heavy consideration, the underlying materials that formed the cubic only received a consideration of being transparent to the incoming light. But, for a truly efficient and state-of-the-art system, it is necessary for each element to be utilized and perform to the highest extent. For example, SU-8 used as the panel material is a biocompatible polymer [157]. On the other hand, the hinge material (SPR 220) can cause in-vivo inflammation. However, the SPR 220 biocompatibility can be improved by surface modification techniques like anticoagulant immobilization on carbodiimide activated surfaces or deposition of a thin layer of Polyethylene (PE) on the hinges, the nanometer thickness of the biocompatible polymer layers does not impact the self-folding yield [158,159]. Moreover, the hinge material can be replaced with a layer of polycaprolactone (PCL), which has demonstrated similar self-assembly properties [160, 161]. The cubic structures can be further encapsulated within a biocompatible polymer shell along with other microbot

components to avoid triggering an immune response. While these simple material integrations make the cubic structure bio-compatible they do not enhance the sensitivity or their resonance response.

Recently, 3D hinge-based self-assembly has also been carried out for nanomaterials like graphene oxide (GO) that preserve their intrinsic properties after transformation into 3D [162]. The oxygen functional groups in GO especially allow the formation of multilayered (laminate) structures and provide opportunities for tailoring its chemical functionality, offering tunable electrical, optical, and electrochemical properties. The fabrication via the self-assembly process yields hollow 3D micro-polyhedral structures configured with 2D GO materials, which incorporates the permeation-driven tunability of multilayered 2D materials into 3D geometry (Figure 2.13a). The unique chemical structure of GO imparts its amphiphilicity properties. The hydrophobic properties originate from the C-C graphene structure and hydrophilic properties from the oxygen functional groups, allowing π–π stacking for hydrophobic molecules and hydrogen bonding for hydrophilic molecules. The hydrated GO layer acts as a molecular sieve that does not allow molecules of radii greater than 0.45nm to pass through it. Thus, resulting in a perfect platform for attracting all classes of targeted molecules for increased sensitivity. Using a similar self-assembly process as detailed previously for

SU-8 cube-based metamaterials, GO can be incorporated through a solution-based dispersion (Figure 2.13b). A key factor to note here is that within the OSRR, the highest sensitivity area (highest electric field) exists at the corner splits. For the highest enhancement of the sensing properties, it is necessary for the nanomaterials to exist at the corner, which given the combination of top-down and bottom-up fabrication in the origami process can be easily achieved (Figure 2.13b, inset). Due to the high affinity and disorder in GO layers in water, this self-assembly was carried out in air on a filter paper because the rough texture of the paper minimizes the surface adhesion once the hinge is melted for triggering the folding (Figure 2.13c). Thus, the self-assembled 3D metamaterials that incorporate conventionally 2D nanomaterials can realize ultra-high detection limits and sensitivity devices with a high yield (Figure 2.13d).

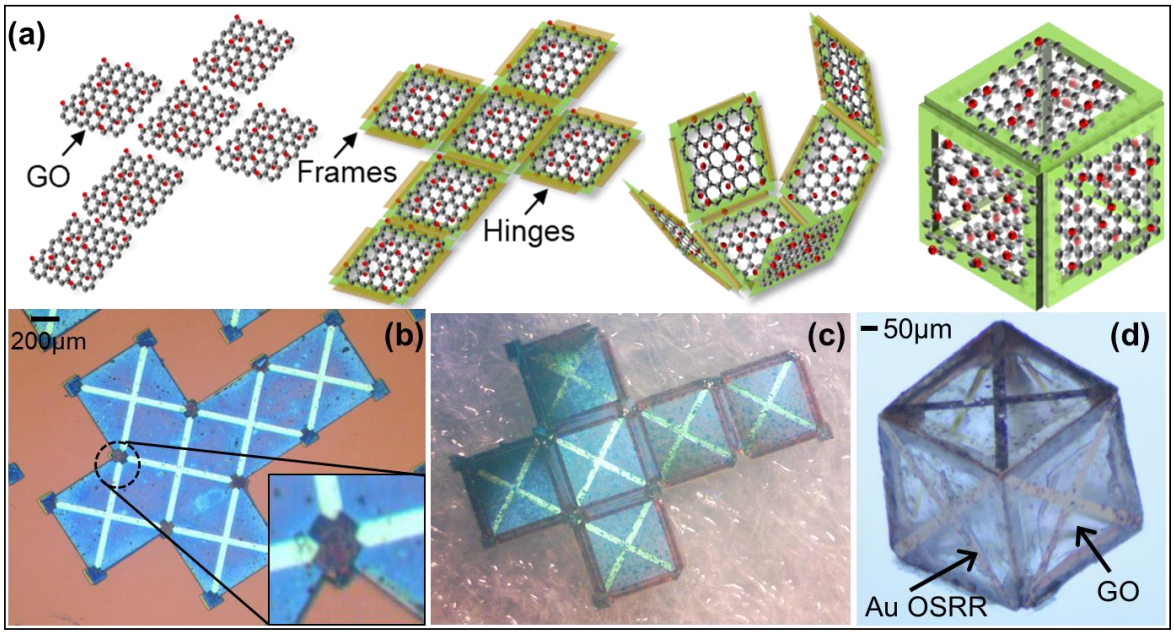

Figure 2.13 (a) Illustration of a self-assembly process for free-standing 3D GO structures showing the 2D structure, halfway folded, and completely folded geometries. [162] (b, c) Optical microscope images of the 2D structures before self-assembly on (b) substrate and (c) filter paper. (d) The self-assembled 3D OSRR incorporating the GO nanomaterial on the surface of the cube.

Chapter 3

Plasmon Coupling and Hybridization in 3D Graphene

3.1 Simulation and design process for 3D graphene

The limitations of conventional 2D graphene have prompted research into 3D graphene as detailed in Chapter 1 with another set of advantages and disadvantages. Taking a cue from the benefits of self-assembled polyhedrons for SRR-based metamaterials as a result of 3D couplings and nanomaterials as explained in Chapter 2, the technique can have benefits from application to other nanomaterials and metamaterial systems such as plasmonics in 3D graphene. To achieve non-spatially constrained near-field enhancement, a hybridized plasmon technique is introduced that benefits simultaneously from two coupling modes (out-of-plane stacking and in-plane coupling) by adopting properties of hollow three-dimensional (3D) nanoarchitectures. In this chapter,

the effect on plasmons in graphene as a result of the 3D coupling is studied for its unique properties and advantages.

The simulations for the plasmon resonance modes were carried out using the Comsol RF module (version 5.2a), with the conductivity of graphene as given by the Kubo formula. A transmission drop was seen at the plasmon resonant frequency for each of the 3D graphene nanoarchitectures. Analysis of the E-field at resonance in the spatial region around the 3D nanoarchitectures was performed with the output E-field normalized to the incident E-field to obtain the near-field plasmonic enhancement (Figure 3.1). The near-field enhancement under each polarization (I_g) was obtained by taking the square of the ratio of the electric field at the resonant frequency of graphene (E_g) to that of the incident electric field (E_o), such that $I_g=(E_g/E_o)^2$; the resulting enhancement was plotted as a color map in natural log scale along virtual cross-section planes placed at different intervals throughout the 3D geometries. Due to software limitations, the cross-sectional planes cannot be cylindrical or tilted; hence, to analyze the fields on the surface of pyramids and tubes, several horizontal cross-sectional planes were placed inside them at small intervals to create a virtual surface at the periphery of the 3D geometries for field visualization.

The total edge field (in volts) was computed by taking the integral of the field (V/m) along the edge. The edge enhancement at the periphery of the structures (P_g) was calculated as the square of the ratio of the total edge field in the presence of graphene and without graphene. One unique phenomenon that can take place in 3D coupled plasmonic geometries is the appearance of giant surface and volume modes, which can be termed as surface (S_g) and bulk volumetric (B_g) enhancements. These can be calculated as ratios through integrals over the surface and defined volumes of the 2D and 3D architectures to provide total surface field ($V \cdot m$) and total volume field ($V \cdot m^2$), respectively. Unlike solid 3D structures with graphene draped over them that can only achieve minimal 3D coupling through adjoining edges, the hollow polyhedral geometries allow a stronger out-of-plane coupling of the field within their volume and adjoining faces, thus, giving rise to surface and volume enhancement modes that are also easily accessible due to their hollow architecture.

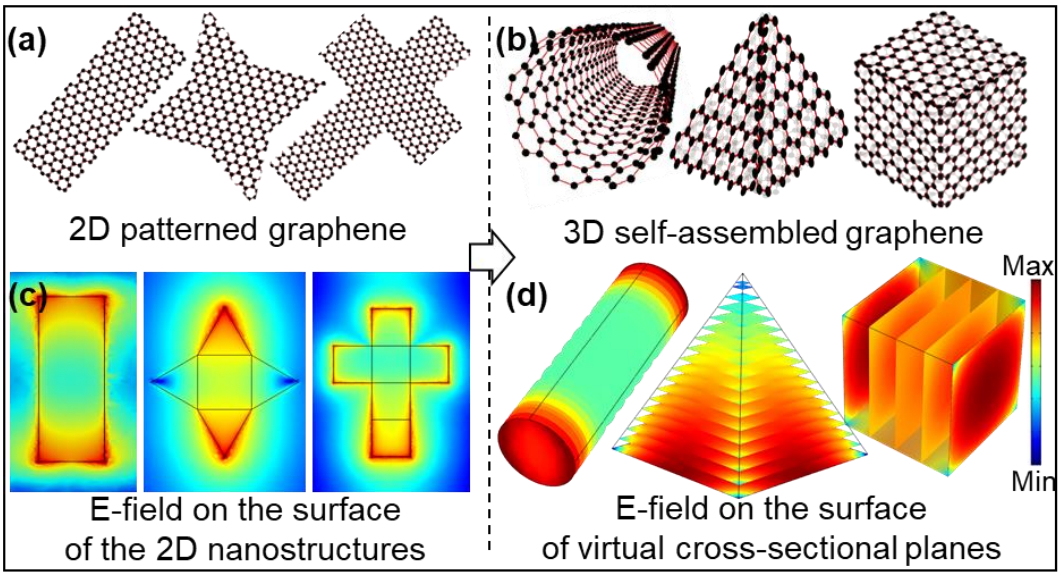

Figure 3.1 Illustration of (a) diverse 2D ribbons, and (b) the corresponding self-assembled hollow 3D graphene architectures including, cylindrical nanotubes, 4-faced square nanopyramids, and 6-faced nanocubes. The enhanced E-field is plotted on (c) the surface of the 2D graphene structures, and (d) the surface of virtual cross-sectional planes placed inside the 3D nanoarchitectures. The E-field is plotted on the surface of the 2D graphene structures, and on the surface of virtual cross-sectional planes for the 3D nanoarchitectures. [183]

3.2 Orthogonal coupling in 3D graphene cubes

Based on the previous sections, the first and easiest graphene structure to discuss becomes orthogonally coupled hollow 3D graphene cubes.

3.2.1 Coupling effect on 3D graphene spectra

To study the influence of the geometric shape (i.e., 2D and 3D) on graphene's optical properties, the transmission spectra of the 2D and 3D graphene-based structures are simulated using COMSOL (RF module, ver. 5.2). In all simulations, the dimension (L) of 500 nm graphene was used. For modeling analysis, the graphene conductivity was calculated using the Kubo formula assuming the graphene relaxation time is 0.35 ps and the graphene doping is 0.4 eV. Figure 3.2a contains transmission spectra for the graphene ribbons and 2D graphene boxes, assuming that boxes are open (i.e., box lacks graphene sheets at two opposite faces, forming a long square tube), the length of the ribbons and the boxes is infinite. As shown in Figure 3.2a, pronounced dips in the transmission spectra are clearly seen, which correspond to the geometrical resonances of the surface plasmons in the graphene. It is well-known that the frequency of the geometrical resonances in graphene ribbons scales as $L^{-1/2}$. This explains the blue shift of the plasmon resonance in the case of transverse electric (TE) excitation of the ribbon compared to the transverse magnetic (TM) case (Figure 3.2 for ribbon cases).

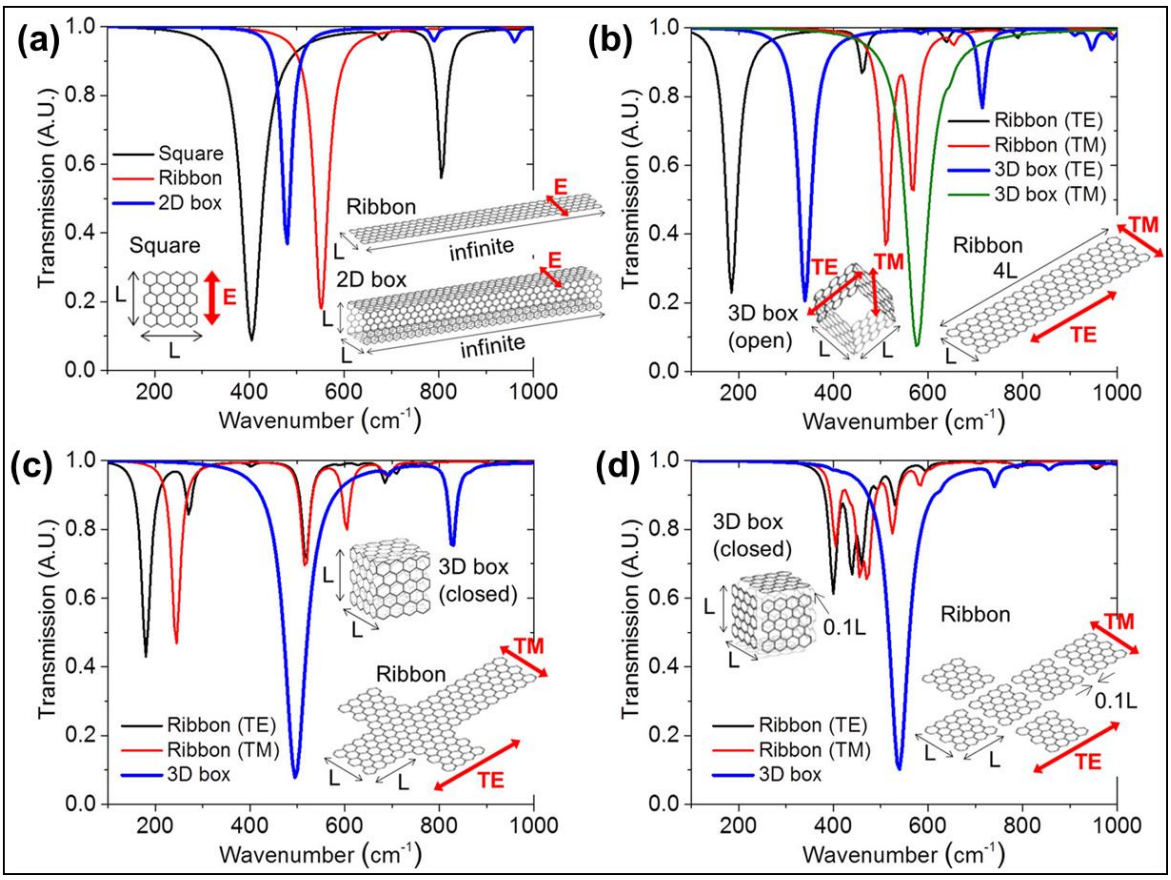

Figure 3.2 Transmission spectra for 2D and 3D graphene-based structures as a function of wavenumber (in cm–1). In all simulations, the dimension, L, is 500 nm. The polarization of the electric field is indicated by red arrows. Transmission spectra for (a) a graphene square, an infinite graphene ribbon, and a 2D, infinite, four-faced graphene hollow box without graphene on two faces; (b) a finite ribbon of length 4L and a 3D open box formed by folding up the 4L ribbon; (c) a six-faced continuous graphene before and after assembly; (d) a six-faced discontinuous graphene (gaps between graphene patterns are 0.1L) before and after assembly. The 3D graphene-based box shows the

superior single resonance peak overcoming the multiple nonuniform coupled modes of a 2D structure. [182]

By folding a graphene ribbon into a 3D open box, plasmons are effectively limited to the faces of the box. The geometric plasmon resonances at each of the faces in 3D are similar to that of the 2D graphene square. However, the coupling between plasmons (plasmon hybridization) at each of the faces in the 3D open box leads to the splitting of the geometric resonances, which reveals itself as a blue- or red-shift of the resonances in the transmission spectra (Figure 3.2b). The transmission spectra for six-faced continuous and discontinuous graphene ribbons/3D boxes are presented in Figure 3.2c, d, respectively. In the continuous ribbon case before self-assembly (Figure 3.2c), plasmon resonances are on the whole length of the ribbon (i.e., 3L for horizontal or 4L for vertical), depending on the wave polarization. The response of the continuous closed 3D box (six faces, Figure 3.2c) is similar to that of the 3D open box (four faces, Figure 3.2b), except for the plasmon in all six faces coupled to each other (for open box, only four faces are coupled). When the discontinuous ribbon is formed with graphene squares separated by 50 nm (0.1L) gaps (Figure 3.2d), the plasmon resonance modes change due to the nonuniform hybridization that exists between the individual squares along

the 3L and 4L directions. The non-uniform hybridization leads to multiple closely spaced resonances with small dips in both TE and TM excitations (Figure 3.2d). It should also be noted that the assembled graphene cube generates only a single resonance in transmission spectra since the geometrical symmetry of the cube causes the uniform plasmon hybridization at each face.

3.2.2 Coupling effect on near-field in 3D graphene

The electric field distributions in these 2D and 3D structures are of particular interest and provide further insight into plasmon hybridizations (Figure 3.3). For a 2D graphene ribbon (Figure 3.3a,b), the distribution is that of conventional plasmon dipolar resonances with fields concentrated at the edges of the ribbon. The graphene cross ribbon pattern (Figure 3.1c–f) continues to demonstrate an electric field similar to that of the 2D graphene ribbon (Figure 3.3a,b). However, under TE excitation (Figure 3.3c), the fundamental resonance frequency and the field at resonance correspond to the resonance of the ribbon of length 4L (north and south edges), while the two squares in the 3L direction (east and west edges) do not demonstrate a high field due to their resonance frequency being higher; the reverse phenomenon takes place for the TM excitation (Figure 3.3d). For the discontinuous 2D

graphene patterns (Figure 3.3e,f), the electric field distribution further supports the theory of multiple resonances in the transmission spectrum. The non-uniform coupling within adjoining graphene strips enhances the electric field within the gaps of the graphene. This enhancement of the field within a given gap is highly dependent on the number of graphene surfaces surrounding it and the polarization direction of the electric field.

For the 3D open box with 4 faces, the electric field pattern under TM excitation (Figure 3.3g) differs from that of the 2D graphene ribbons (Figure 3.3b) to a great extent. Instead of the electric field rapidly decaying away from the 2D graphene surface (Figure 3.3b), the electric field in the 3D open box extends into the void between the graphene faces (Figure 3.3g). The 3D distribution shows the uniform reduction in the field as it moves from the edges to the center of a face without any graphene, creating circular electric field spots due to the symmetry of the structure. The distribution of the plasmon electric field in the case of 3D six-faced cube (3D closed box) provides further insight into the hybridization of the plasmons in 3D structures. To explore the effect of the packing density, the 3D closed box is studied with three different gap sizes between the faces: no gap (Figure 3.3h), 50 nm gap (Figure 3.3i), and 150 nm gap (Figure 3.3j). One can clearly see circular interference patterns on the cube faces, which are orthogonal to the polarization of the electric field

(Figure 3.3h–j). As the faces of 3D cubes are orthogonal to the electric field polarization, the surface plasmons cannot be excited directly by the incident wave. Rather, they are generated by the fields of the surface plasmons excited on the neighboring faces. The uniform constructive and destructive interferences of the plasmon produce the above-mentioned circular interference patterns (Figure 3.3h–j). The electric field intensity and the diameter of the maxima at the center of the face increase as the gap decreases due to increased interaction between plasmons generated at the neighboring faces. For a continuous graphene cube in Figure 3.3h, the diameter is slightly bigger than the size of the face of the cube which leads to the interference maxima occupying nearly the entire face. Thus, the uniform orthogonal coupling from all directions renders unique optical properties in 3D closed and open box structures indicating the potential of these devices for the fabrication of ultrasensitive, compact molecular sensors.

Exposing a graphene-based sensor to a foreign substance(s) (e.g., particles and molecules) changes the optical response (resonance frequency in the transmission spectrum) of the sensor depending upon the characteristics of the target substances. A problem is that the multiple closely spaced resonances seen in the transmission spectra of the 2D graphene arrays (Figure 3.2d) could mask the frequency shift induced by the target substances. However, using the

3D structure (with a single resonance in transmission spectrum) as a sensor allows the detection of the foreign substances without complications arising from closely spaced resonances. The detection of a target by an optical sensor is to a large degree determined by its spatial overlap with the excitation optical fields. Particularly, for high sensitivity, it is necessary to increase the sensing area to the entire volume of the targeted substances, in order to detect very minute concentrations of the target that may be far away from the sensor surface. Thus, a very strong electric field extending into the bulk of the substances containing the target is required for ultrasensitive detection.

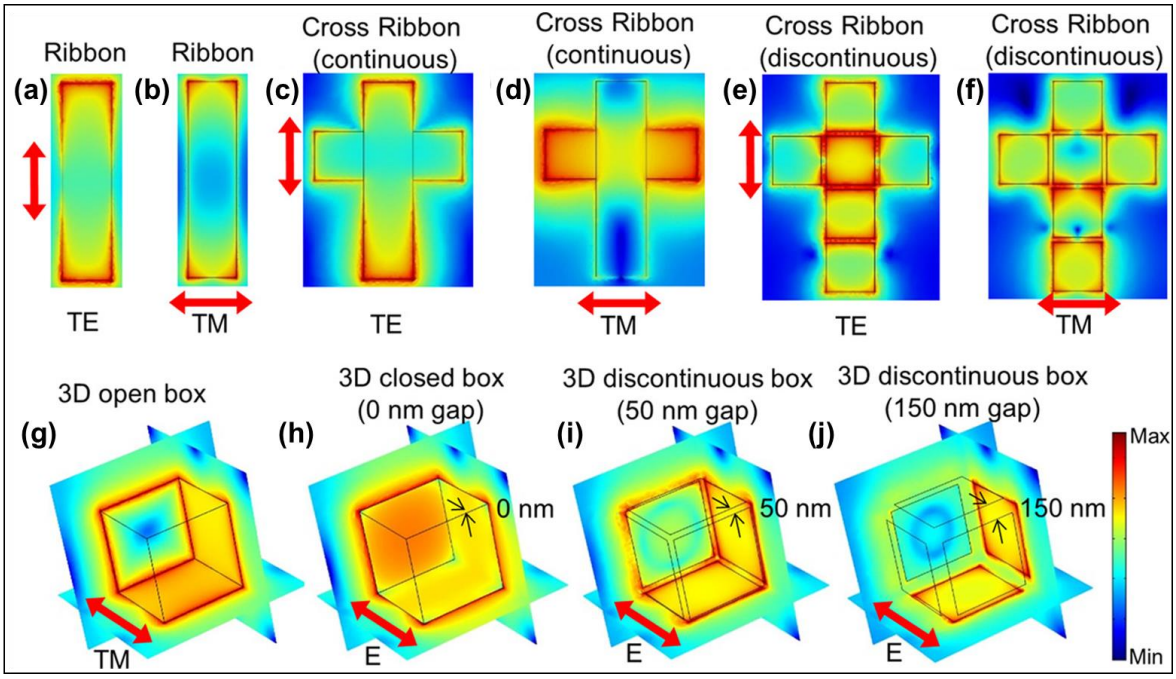

Figure 3.3 Simulated electric field distribution for various graphene resonators at the frequency of a fundamental resonance. (a,b) Electric field distribution for a ribbon of length 4L. (c–f) Transformation of the distribution from the

uniform 2D ribbons when patterned into nonsymmetric structures and the nonuniform electric field distribution in the case of discontinuous closely spaced patterned arrays. (g–j) Variation in the plasmon coupling and electric field in the case of (g) 3D four-faced open box under TM mode, (h) 3D six-faced closed box of continuous graphene (0 nm gap), and 3D closed boxes of discontinuous graphene separated by a gap of (i) 50 nm and (j) 150 nm. [182]

This concept can be realized by transforming 2D graphene into 3D graphene-based structures, which generates volumetric light confinement induced by 3D plasmon hybridization in 3D graphene-based structure (Figure 3.4). The sensing area of 2D planar graphene is limited to the region close to the graphene face because the electric field is localized only on the surface and rapidly decays as one moves away from the 2D graphene face (Figure 3.4). However, the 3D open box structure induces a nontrivial spatial distribution of strong electric fields, resulting from the 3D plasmon hybridization in graphene. The electric field enhancement at the surface of 3D graphene is ∼four times higher than that of the 2D ribbon as well as the minimum field enhancement at d = +250 nm at the middle within the 3D open box is close to the maximum enhancement obtained from a 2D ribbon surface (d = 0 nm). This result shows the sensing area can be further extended into the void within the open box,

creating a high sensitivity optical scanner. For instance, a graphene-based, 3D, (blood-) vessel-like tube with a strong electric field at the inner/outer surfaces and within the void (or cavity) can be used to sense, with sensitivity higher than that of 2D planar sensors, a substance in the fluid as it flows through the inside of the 3D open box by monitoring for any change in this field.

The circular interference patterns at the faces of 3D closed box graphene cubes demonstrate the importance of the cubic structures for the development of plasmonic devices that allows for efficient manipulation of the electric field and for the creation of focused hotspots, which may also lead to high sensitivity. Unlike the 3D open box, the 3D closed box graphene generates a highly confined electric field within as well as outside of the cubes due to coupling in all directions. When looking at the electric field enhancement inside and outside the cube, the uniform plasmon coupling from all directions creates strong electric field enhancement (∼230) at the surface of the graphene (Figure 3.4 at d = 0). The uniform coupling reduces the decay of the field enhancement with a minimum value of ∼100 (inside cube at d = +250 nm) and ∼80 (outside cube at d = −250 nm) at a distance of 250 nm from the surface; which is more than two orders of magnitude higher than that of the 2D ribbon (∼1 at d = ± 250 nm). This result implies that by utilizing the highly confined electric field, the 3D closed box graphene can be used as a sensor with high

sensitivity to detect and/or secure the targeted substances while maintaining their integrity due to the impermeability of the graphene membranes.

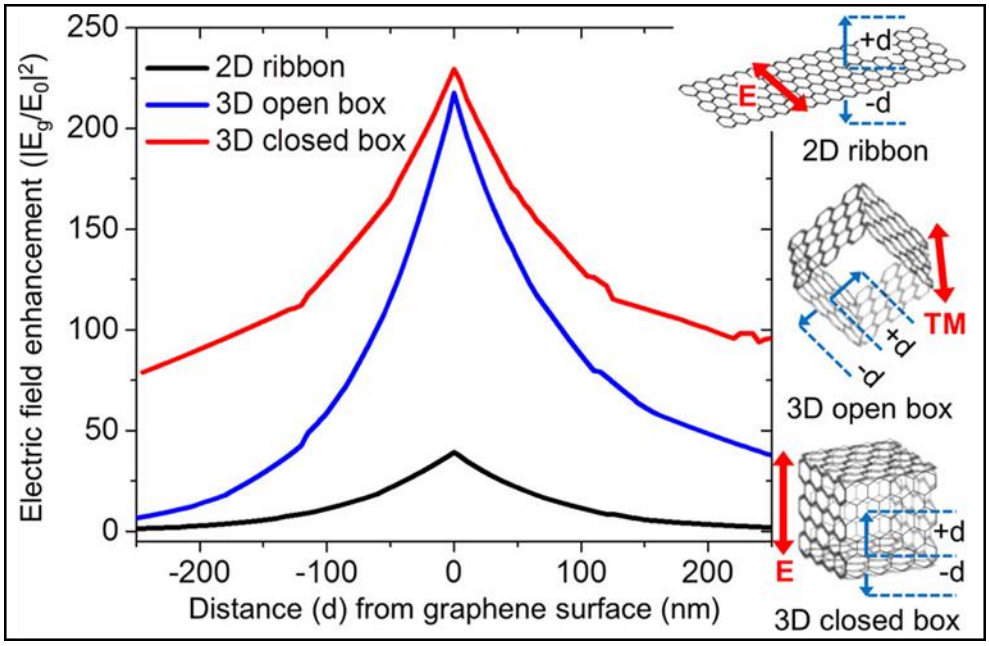

Figure 3.4 Variation in the simulated electric field enhancement (where, E_g is the electric field in the presence of graphene and E_0 is the incident electric field) as a function of distance (d) along an imaginary line drawn perpendicular to the graphene surface. In 2D ribbon case, the line passes through the geometrical center of graphene ribbon. The distances are measured below (−250 nm) and above (+250 nm) the graphene surface. For the 3D open box, the line is perpendicular to the direction of polarization of incident electric field and passes through the center of the graphene faces on the bottom of the box. For the 3D closed box, the line is parallel to the direction of polarization of incident electric field and passes through the hotspot created by the plasmon

hybridization. The distances are measured from the outside the box (−250 nm) to the center of the box cavity (+250 nm). The illustrations depict the orientation of the line with respect to the field. The uniformly coupled plasmons in the 3D structure reduce the electric field decay with distance as compared to 2D graphene (ribbon), leading to the strong electric field that exists inside the 3D open box (from 0 to +250 nm) and inside/outside of the 3D closed box (from 0 to ±250 nm). [182]

3.2.3 Geometrical parameters within 3D cubes

The 3D plasmon hybridization in cubic graphene leads to large hotspot surfaces of enhanced electric (E) field on the surface perpendicular to the direction of polarization of the incident E-field. The maximum enhancement spreads over the entire hotspot surface of the cube (Figure 3.5). To increase the enhancement at the vertices of the cubes, the size of the cube is scaled (Figure 3.5a), which also causes an exponential increase in the total surface enhancement (S_g) obtained across all the surfaces, *i.e.*, parallel to the incident E-field and perpendicular to the incident E-field (Figure 3.5b). Furthermore, the increased intensity of the hotspot surface also results in a proportional increase in the volumetric field (Figure 3.5c) induced within the volume of the

cube causing an increase in the enhancement by an order of magnitude (Figure 3.5d). Thus, scaling the size of cubic graphene architectures exhibits an order of magnitude increase in point enhancement (I_g) for 50 nm cubes compared to 500 nm cubes, while simultaneously inducing a 4-fold increase in the surface enhancement (S_g) between the two sizes.

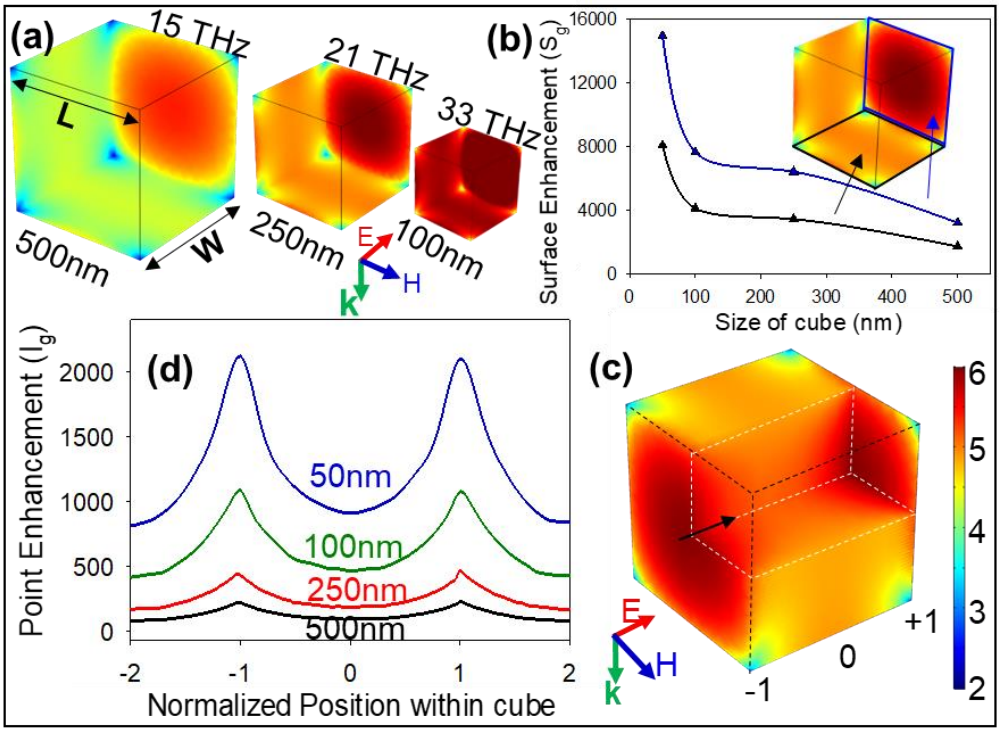

Figure 3.5 Simulation results for 3D graphene cubes for varying size and dimensionality. (a) Simulated plasmonic field enhancement for the 3D graphene cube showing the changes in the enhancement on the surface of the cube for changing size of the cube from 500 to 100 nm, increasing the resonant frequency from 15 THz to 33 THz. (b) Graph showing the exponential increase in the total near-field enhancement on the surface of the cube, Sg, that is parallel to the polarization direction of the incident E-field (black line) and the

hotspot perpendicular to the polarization direction of the incident E field (blue line) with a decrease in size of the cube while maintaining L = W. [183]

The circular shape of the hotspot is caused by the symmetry and equal length (L) and width (W) of the structure in all directions. We can define a dimensionality parameter for the cubes as $\alpha_c = L/W = 1$. As the value of α_c for the 3D cubic structure is changed, the enhancement across the surface of the hotspot demonstrates a behavior opposite to that in 3D pyramids. At small dimensionalities ($\alpha_c < 1$), the length of the graphene surface is insufficient to produce the maximum enhancement at the center of the hotspot (Figure 3.6a, L = 125 nm). When the dimensionality parameter is increased (α_c = 2, 4) by increasing L with constant W = 250 nm, the uniform interference from the edges of the adjoining surfaces leads to an enhanced hotspot surface (Figure 3.6b).

At α_c = 2 (L = 500 nm), the maxima created at the center of the surface encompasses the entire graphene face with nearly uniform intensity, $I_g \sim e^6$ the shape of the hotspot changes to an elongated circle due to the dissimilar length and width of the cubic structure (Figure 3.6a). The hotspot surface demonstrated a maximum radius for the hotspot surface nearly 6 times the plasmon wavelength, resulting in a small decay in the enhancement near the

edges of the hotspot surface for the cube with α_c = 8 (L = 2000 nm) (Figure 3.6a). The maximum radius and intensity of the hotspot also result in a 3-fold increase in the point (I_g) and total volumetric (B_g) field enhancement for the cubic graphene between α_c = 0.5 and 4 (Figure 3.6b).

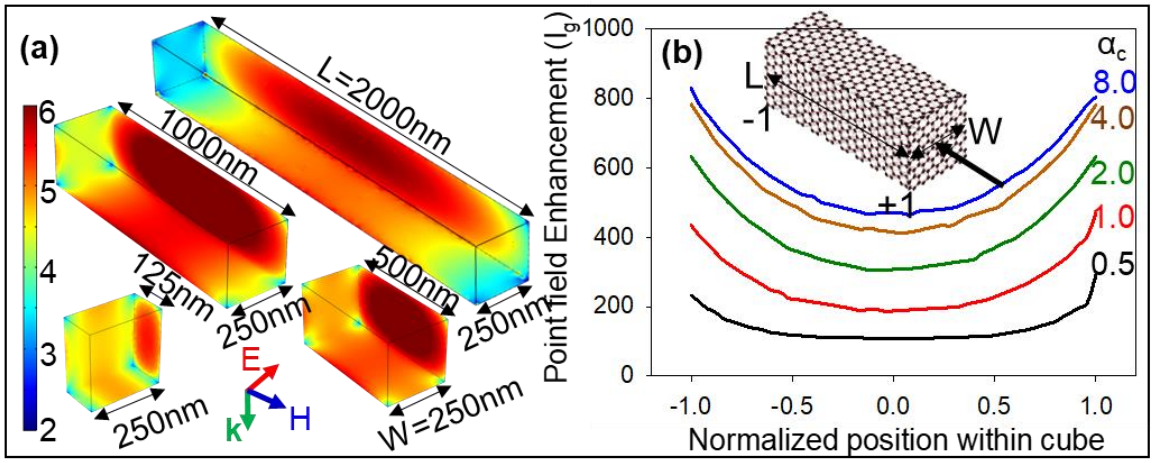

Figure 3.6 Enlargement in area and increase in intensity of the hotspot surface created by the plasmon hybridization in a 3D cube due to the increase in α_c from 0.5 to 8.0 for a constant W = 250 nm and increasing L = 125, 500, 1000, and 2000 nm. (d) Variation in the intensity of enhancement, I_g, along the length of the cube for each value of α_c; the intensity was obtained for positions at the center of the cube along the direction indicated by the arrow, and the normalized position was found by dividing the actual position by the length of the cube. [183]

3.2.4 Edge-dependence of resonance in 3D cubes

The edge effect in 2D graphene nanoribbons are straightforward and easily explained, however, in 3D graphene nanostructures, the extra dimensionality supports coupled modes that are strongly affected by edges but in a complex manner. For a 6-faced closed 3D cube, the uniform plasmon hybridization from all direction leads to a highly coupled hotspot field with a strong uniform intensity on the graphene surface perpendicular to incident E-field. In the absence of uniform interference from all directions, this surface of graphene does not support any plasmon resonance modes due to its perpendicular orientation with respect to incident E-field polarization. The completely closed 3D structure consists of 12 edges with edges on adjoining faces uniting together, if gaps are added between adjoining faces, the total number of edges for the 6-faced 3D cubes increases to 24. Even in the presence of a gap between the edges, the plasmonic field on neighboring faces acts as a confined source and is able to excite edge plasmons in the graphene surface perpendicular to the incident E-field. The excited edge plasmons exhibit a fringe like behavior creating alternate circular rings of constructive and destructive interference. The intensity of the interference maximum and minimum is strongly dependent on the distance between the edges as shown in Figure 3.7a. When the distance between edges increases from 1% (2.5nm for

a 250 nm cube) to 16% (40 nm for 250 nm cube), the intensity of the corresponding surface maximum encounters a fourfold reduction but retains the circular pattern as a result of the symmetry of the structure. It is interesting to note that for each of the varied length gaps in the 24-edge cube, the ratio of the interference maximum and minimum remains a constant.

Furthermore, as the number of edges and the distance between them is increased, the coupling between them is decreased in the 3D cube. The edges with a 1% gap exhibit the highest amount of coupling between them and can efficiently excite edge plasmons by light confinement in the gaps between two edges, similar to scenarios already investigated for 2D ribbon arrays. The coupled edges increase the electric field at the corners of graphene as well as throughout the edge (Figure 3.7b, c). When the gap distance is increased, the capacitive coupling between adjoining edges decreases and consequently lower edge enhancement occurs than for 1% gap distance (Figure 3.7b). However, even at a 30% gap distance, the normalized edge-based enhancement is nearly 4 times higher than for the closed 3D graphene cube with 0 gaps. The large surface area hotspot in closed 3D graphene nanocubes have been shown to modify the decay of the field away from the surface, giving rise to strong volumetric enhancement inside the volume of the hollow cubes. Since the volumetric field is a direct consequence of coupled plasmon state, the lower

coupling at increased gap distances reduces the fields at the center of the cube and consequently reduces the volumetric field enhancement. Another type of 3D cube that can be self-assembled is open-ended 4-faced cubic structures (Figure 3.7d). The 4-faced structures are particularly attractive due to their potential as rectangular plasmonic flow channels for active sensing of analytes. In the absence of a surface perpendicular to the incident field for uniform plasmon hybridization, the field from the edges of the graphene decays exponentially towards the center. As the gap is increased, unlike the 6-faced cubic structure, not a large change is seen in the maximum electric field intensity at the corners. However, the lower coupled field at the center rapidly decays and a smaller area with a strong enhancement is encountered (Figure 3.7e). The self-assembly technique described previously can be easily modified to incorporate the edge-based cubic structures by simply modifying the 2D pattern before self-assembly and patterning the individual graphene faces with the desired spacing between them.

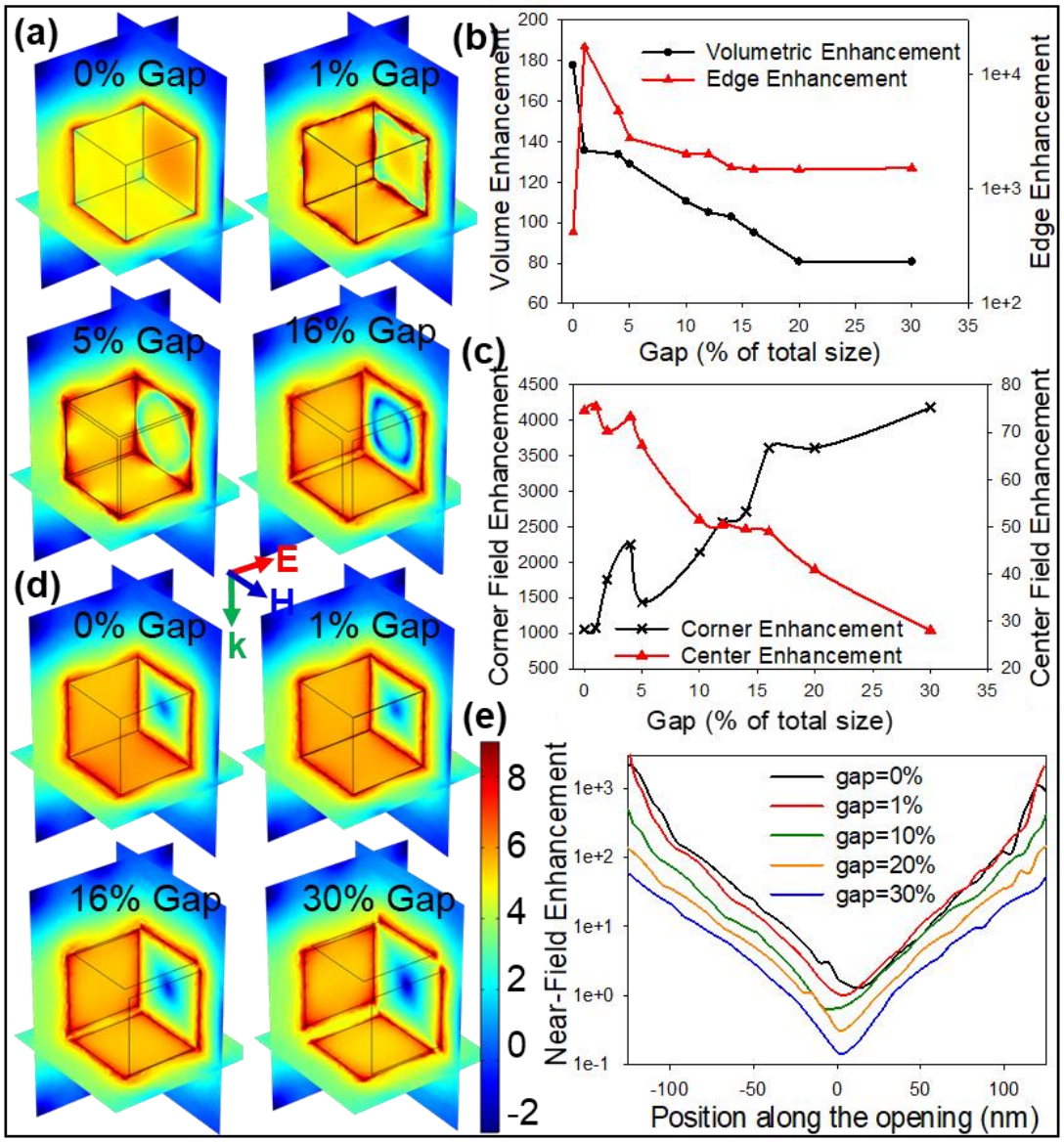

Figure 3.7 (a) Simulated normalized electric field enhancement on the surfaces of the 250nm 6-faced graphene cubes with the gap between individual edges increased from 0% (0nm) to 16% (40nm) showing the concentric interference patterns. (b) Graph showing the decrease in the volumetric enhancement and the increase in the edge enhancement for the 3D hollow cubes with an increasing distance between the edges. (c) Increase in the electric field

enhancement at the corner of faces due to lower coupling and corresponding decrease in the field enhancement at the center of the cubic structure. (d) Simulated electric field at the surface and opening of the 4-faced graphene cube showing the increase in area of the zero-enhancement center when increasing the distance between edges. (e) Graph showing the variation in the field enhancement plotted along the opening of the 4-faced structure for different gap percentages.

3.3 Full 360-degree coupling in 3D graphene pyramids

It is known that plasmons on the slant faces of pyramids propagate toward the apex under TM (transverse magnetic) polarization to constructively interfere at a single point (apex), delivering intense nanofocused fields [163]. In this section we analyze the plasmonic modes in 3D graphene pyramids and their geometrical tunability.

3.3.1 Coupled modes in 3D graphene pyramids

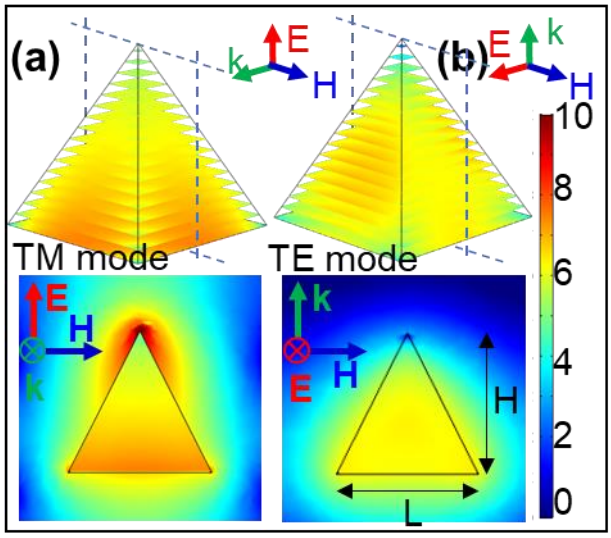

Figure 3.8 TE and TM mode simulation for 3D graphene pyramids. (a, b) Plasmonic field enhancement (log scale) obtained for the 3D graphene pyramid under TM mode (left) and TE mode excitations (right) for pyramids with L = H = 250 nm. The 2D cross-sectional images are obtained by plotting the field enhancement on virtual planes placed at the center of the pyramid as illustrated by the dashed lines. [183]

Primarily, two modes can occur for the pyramid. Firstly, when the incident E-field is polarized towards the apex of the pyramid (TM mode), and secondly, when the incident E-field is polarized across the base of the pyramid (Transverse electric, TE mode) as shown in Figure 3.8, b. For a square pyramid

with equal length (L) and height (H), the resonant modes for the two polarizations exist close to each other in frequency (17.0 THz for TE mode and 18.2 THz for TM mode at L = H = 500 nm) due to the same length of graphene in the direction of polarization. Under TM excitation, a strong field enhancement exists at the apex of the pyramid as a result of the reduced width at the apex. The strong field at the apex decays as the distance from the apex increases; however, at the base of the pyramid, a strong field reappears due to the uniform plasmon interference from the edges of four adjoining faces of graphene (Figure 3.8a). Under TE excitation, a reverse phenomenon takes place as compared to TM excitation, where a strong field is seen only near the base of the pyramid and

decaying towards the apex as a result of the greater edge-based field interference (Figure 3.8b).

3.3.2 Geometrical parameters within 3D pyramids

Modification of dimensions comprising the nanopyramids could achieve highly customized enhancement not limited to classical hybridized TM and TE plasmon modes. For the graphene pyramid, while maintaining equal length of base (*L*) and height (*H*), the height of the pyramids was decreased from 500 to

50 nm. The near-field enhancement within the pyramids increases as the size of the pyramids is reduced (Figure 3.9a,b). A simultaneous change in the length and width of the pyramid causes a proportional change in resonant frequency such that the primary TM mode plasmon resonance for the structures of aforementioned dimensions occurs at 17.0 THz, 24.0 THz, 37.4 THz, and 52.0 THz, respectively. The maximum near-field enhancement that can be obtained for any size of the pyramid is scaled exponentially with the size of the structure as $e^{1/\lambda}$, where λ is the wavelength of resonance at the particular size.

For the 500 nm pyramid, the maximum enhancement ($I_{g,max} \sim 4.4 \times 10^4$) exists at the apex, which is 2 orders of magnitude higher than at the base of the pyramid ($I_{g,min} \sim 100$) (Figure 3.9a). At reduced sizes, the shorter height of the pyramids allows the field at the apex to couple strongly with the base, thereby sustaining the point-based apex field over longer distances (even at reduced plasmon wavelength) within the spatial volume of the pyramid as observed by an increase in the $I_{g,min}$ inside the pyramids (Figure 3.9a, 250 and 50 nm). Hence, the full-360 degree coupling within the pyramids through the slant edges at the apex and between the apex and base causes for the 50 nm pyramids to possess strong enhancement encompassing the entire pyramid structure (Figure 3.9a, 50 nm). Moreover, changes in dimensions of the pyramids not

only sustain the field at the apex over the entire geometry but also exponentially increase the maximum enhancement for the pyramids (Figure 3.9b) as a direct consequence of increased resonant frequency at a smaller size of pyramids. The smaller decay of the near-field enhancement inside the structures and the increase in the maximum enhancement gives an overall increasing total (volumetric) enhancement within the pyramids with decreasing size (Figure 3.9b).

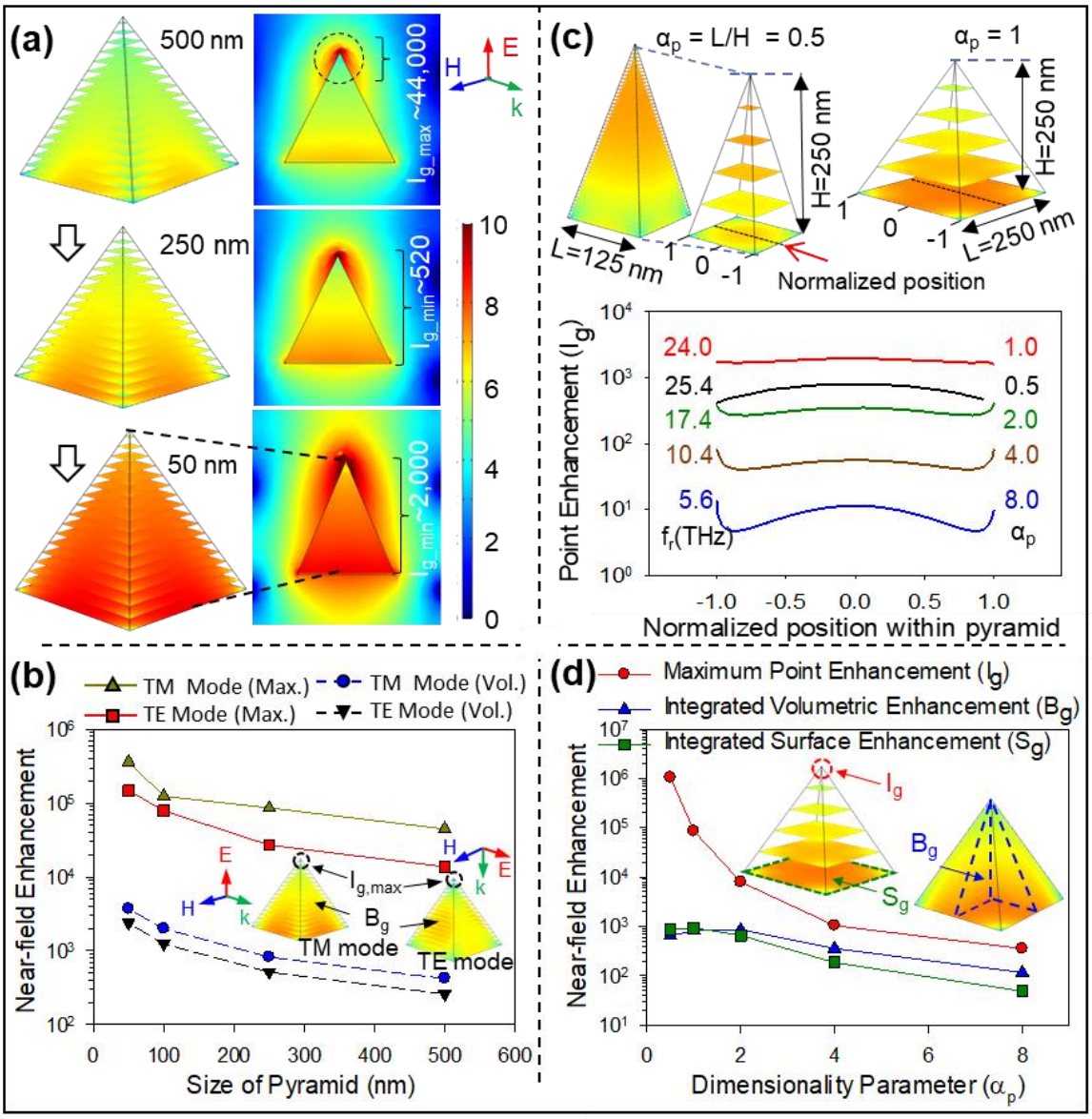

Figure 3.9 Simulation results for 3D graphene pyramids of varying size and dimensionality. (a) 3D color maps and 2D cross-section showing the variation in the field enhancement under TM excitation for varying lengths (*L*) and heights (*H*) of the pyramids from 500 to 50 nm. (b) Graph showing the exponential increase in the maximum near-field enhancement, $I_{g,max}$, at the apex of the pyramid and the volumetric (average) field enhancement, B_g,

within the pyramid for decreasing size of the pyramid under TM and TE polarizations. (c) Graph showing the variation in the near-field enhancement, I_g, at the resonant frequency for variations in α_p, obtained at positions on the base of the pyramid along the direction indicated by the red arrow in the simulated images. The simulated image represents TM mode electric field within the pyramid for $\alpha_p = 0.5$ and 1.0 obtained at a fixed height (H) of 250 nm and varying the length of the base (L). The normalized position is given by the ratio of the actual position and half the length of the base such that the base extends from −1 to +1. (d) Graph showing the variation in the maximum (point) enhancement ($I_{g,max}$), base surface enhancement (S_g), and volumetric enhancement (B_g) as the dimensionality parameter (α_p) is varied by changing the length of the base. [183]

The simultaneous scaling of the length (L) of the base and height (H) of the pyramid proportionally changes the plasmon wavelength and consequently the near-field enhancement. However, depending upon the application it maybe imperative to control the enhancement while preserving the frequency range as in the case of molecular sensing for diminishing concentrations, where the operating frequency is determined by the vibrational frequency of the molecule to be analyzed. In 3D pyramidal graphene, for a constant height, the

plasmon wavelength remains nearly constant; thus, by varying other dimensions in the pyramid (length of base) diverse hybrid modes can be obtained with a nearly constant operating frequency range. When the size of the pyramid is changed by varying the dimensionality parameter ($\alpha_p = L/H$), a smaller change in TM resonant frequency (F_r) is obtained due to a constant size in the direction of the incident E-field polarization. For the simultaneous scaling of length and width, a 35 THz change in resonant frequency was obtained for a 450 nm (500 nm to 50 nm) variation in size. However, for a constant width, the change in the length of the pyramid causes only a ~20 THz shift in resonant frequency for a 1875 nm change in length (L=2000 nm, F_r = 25.4 THz at α_p=8 and L=125 nm, F_r = 5.6 THz at α_p=0.5). At low values of dimensionality parameter ($\alpha_p = L/H$) of 0.5 and 1.0, obtained by decreasing *L* (Figure 3.9c), the narrower slant surfaces of the pyramid structure result in an increased E-field at the slant edges that increases toward the apex. The uniform interference of the fields from the slant edges results in a strong volumetric enhancement and a constant surface enhancement at the base of the pyramid (Figure 3.9c). Thus, even for decreased resonant frequency (at α_p = 2.0) that decreases the maximum enhancement, the 3D plasmon coupling exhibits an increased surface and volumetric enhancements between α_p = 0.5 and α_p = 2.0.

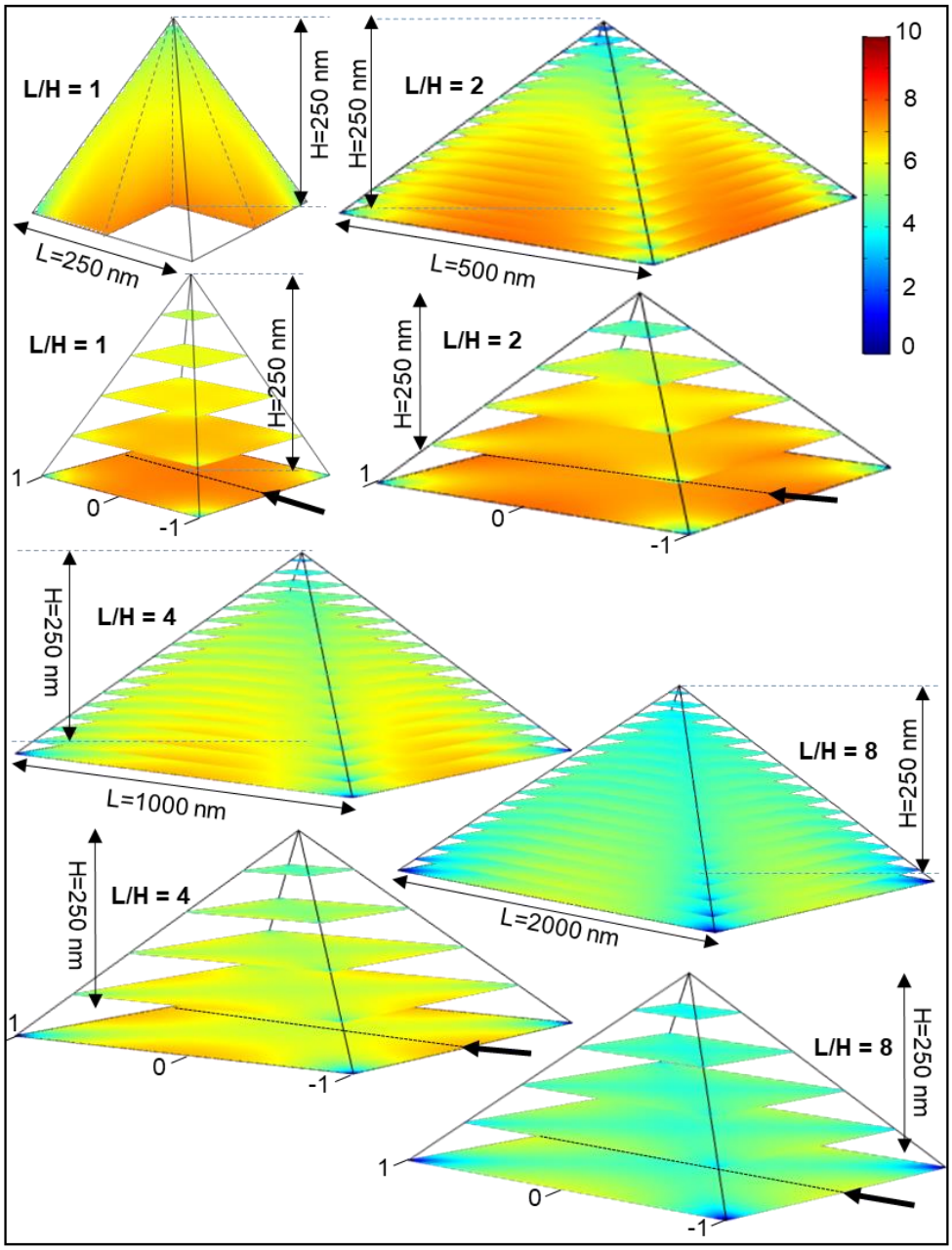

Figure 3.10 Simulation result for 3D pyramids of varying dimensionality parameter. Change in the near-field enhancement (log scale) for 3D graphene pyramid with αp=1, 2, 4, and 8 at constant height (H) of the pyramid (H=250 nm) and varying length of base (L = 250 nm, 500 nm, 1000 nm, 2000 nm). [183]

However, at larger values of α_p = 4, 8 (Figure 3.10), the interference from the edges of the pyramid and the field scattered from the apex is unable to sustain the extreme enhancement across the entire area of the enlarged base and volume of the pyramid (Figure 3.9c). The nearly constant field enhancement of ~2000 obtained at any point on the 3D coupled base for α_p = 1 square pyramids is reduced to ~9 for base of pyramids with α_p = 8. Thus, at α_p = 0.5, 3D couplings between the edges, apex, and base leads to a maximum enhancement ($I_{g,max} \sim 1.05 \times 10^6$) that is more than 3 orders of magnitude stronger than for a pyramid with α_p = 8 ($I_{g,max} \sim 353$) (Figure 3.9d). On the other hand, at small α_p values (0.5–2), large areas of surface enhancement ($S_g \sim 900$) are induced that couple with the apex to cause an increased volumetric field (Figure 3.9d).

3.2.3 Edge-dependence of resonance in 3D pyramids

The introduction of the 3D cubic structure with specific gap sizes requires the modification and redesign of the 2D pattern to be self-assembled. In contrast, a more dynamic control over the gap distance between the edged

can be achieved for in-situ assembled 3D graphene nanopyramids. As the folding angle is increased the edges on the slant faces of the cube move closer to each other, finally touching at a folding angle of 120° for a square pyramid of base length and height equal to 250nm (Figure 3.11a). The folding angle can be easily controlled for the in-situ self-assembled 3D pyramids by controlling the exposure time to the incident ion beams that cause the melting of the polymer hinge for triggering self-assembly.

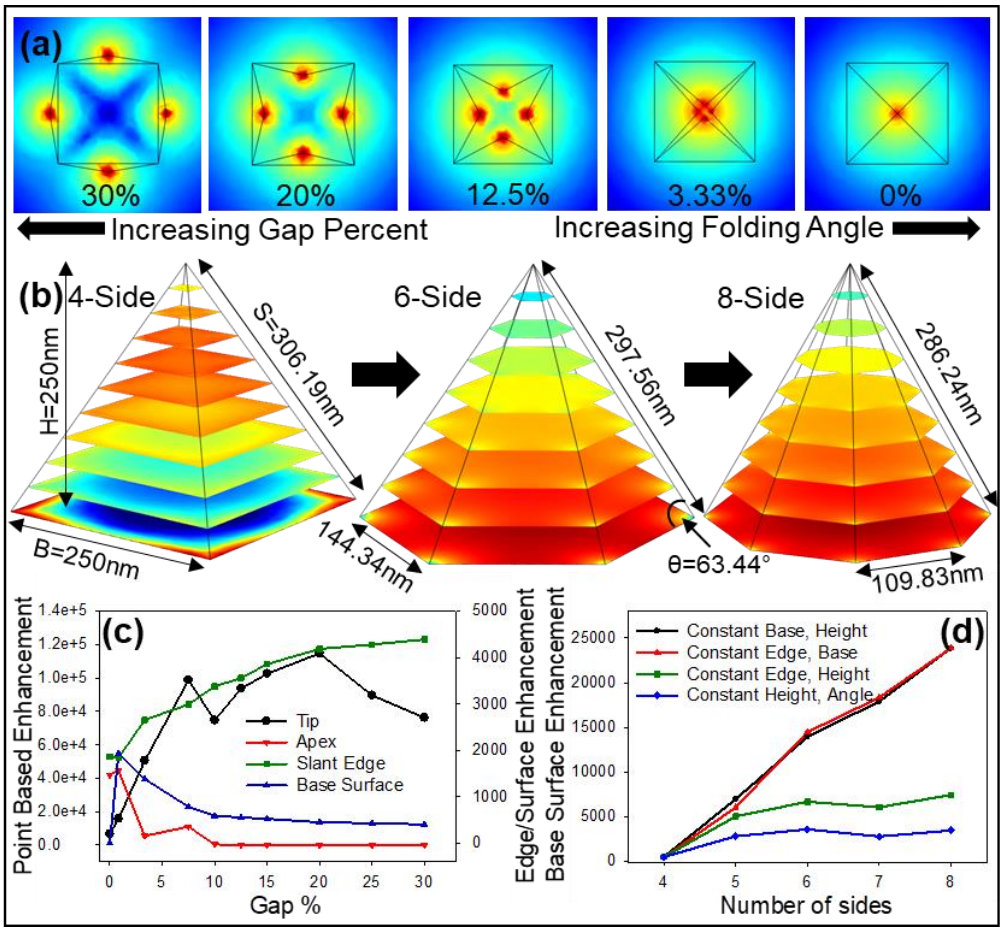

Figure 3.11 (a) Top view images showing the effect of the increasing folding angle which changes the gap between the edges for a 3D pyramid with length

of base and height equal to 250nm. The electric field is polarized into the plane towards the apex of the pyramid. (b) Effect of change in the number of sides for the 3D pyramid when maintaining a constant height (H) and slant angle (θ). (c) Graph showing the increase in enhancement at the edges and tips of the individual triangular faces and the corresponding decreases in the coupled enhancement at the center of the pyramid and at the base surface on increasing the gap distance between edges by lowering the folding angle. (d) Total integrated electric-field enhancement at the base of the structures when the number of slant and base edges are increased from 4 to 8 while maintaining any two geometrical dimensions constant among length of base (B), height (H), length of slant triangular edges (S) or the slant angle of the triangular surfaces (θ).

The gap % can be calculated as the ratio of the difference between current (Φ) and maximum folding angle to the maximum folding angle (gap % = (120- Φ)/120*100). The 3D pyramids with E-field polarized towards the apex undergo an extremely strong point-based enhancement at the apex of the pyramid. The strong enhancement at the apex of the pyramid also gives rise to slow field decay allowing the enhanced E-field to engulf the 3D pyramids and give rise to volumetric and base-surface enhancement. Similar to the maximum

enhancement in 3D cubes, the enhancement at the tip of the triangular surfaces undergoes a strong uncoupled resonance at large gap distances (Figure 3.11c). The field at the apex (center of the gap structure) follows a reverse trend where it decreases for larger gap distances (Figure 3.11c) and has a maximum for the strongly coupled 1% gap structure. Since the electric field at the edges of the slant triangular surfaces of the 3D pyramid is excited by plasmons at the tip and the field at the base of the pyramid is dependent on this field at the apex, they also follow a similar trend with gap distances (Figure 3.11c). The opposite trends of surface and edge enhancement with gap distances allows customization of the enhancement in 3D graphene nanopyramids based on the targeted application.

The enhancement in 3D graphene nanopyramids can further be tuned by the number the edges, and length and angle of inclination of the edges (Figure 3.11b). As the number of edges in the 3D graphene pyramid are increased while maintaining a constant length of base edges (B) and height (H) (Figure 3.12a), the enhancement on the base surface experiences a rapid increase (Figure 3.11d) even though the distance between edges and the base area are increased (Figure 3.13a) while the resonant frequency is reduced from 22 THz to 16 THz. The higher base surface enhancement occurs as a result of decreasing slant angle (Figure 3.12d) which increases the interaction with the

apex and transfers the enhanced electric field from the apex to the base of the pyramid, causing a lower enhancement at the apex of the pyramid (Figure 3.12c).

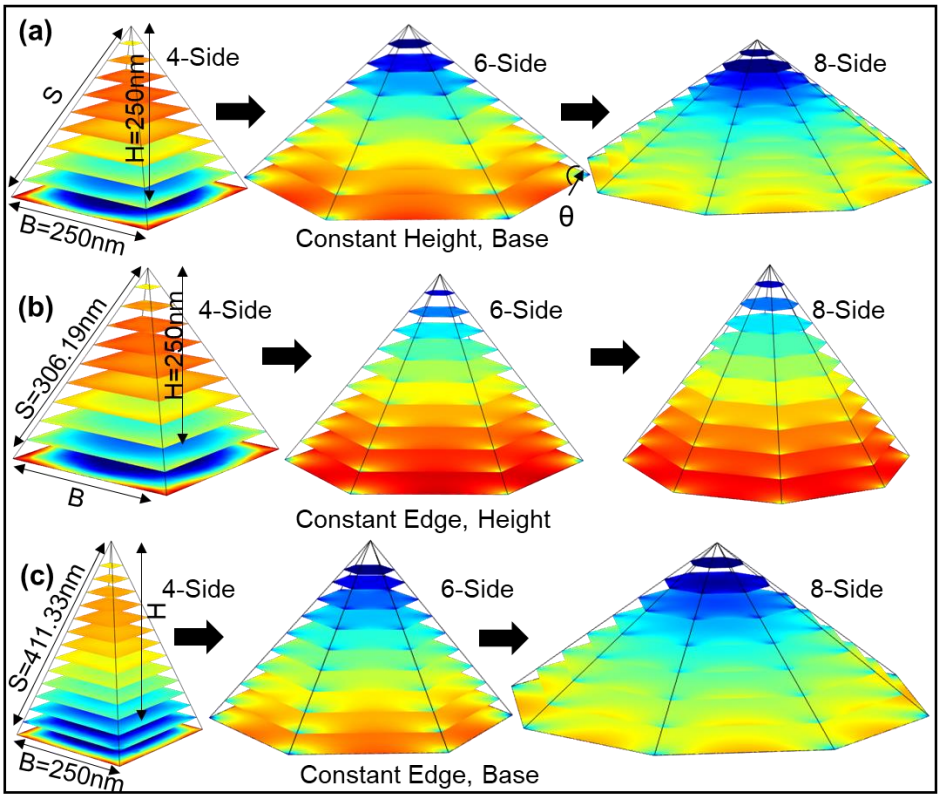

Figure 3.12 Normalized simulated electric field inside the 3D pyramids for varying number of triangular and base edges while maintaining a constant (a) length of base edges and height of pyramid, (b) length of slant edges and height of the pyramid, and (c) length of slant and base edges of the pyramid.

The same argument also holds true for increasing the number of edges while maintaining a constant length of the base edges of the pyramid (Figure 3.13b, Figure 3.11d). However, if the number of edges is increased while maintaining a constant height and slant length or slant angle (Figure 3.11b and Figure 3.13c), the interaction of the apex with the base of the pyramid does not significantly change. Thus, leading to only minor variations in the base electric field which are caused primarily by minor changes in resonant frequency (Figure 3.11d). Thus, modification of the number of edges while controlling the dimensions of the 3D graphene nanopyramid allows an efficient mechanism for the tuning between the strong point-based enhancement at the apex to the large surface-area enhancement at the base. The 3D nanopyramids with a varying number of edges can be easily fabricated by the surface-tension driven self-assembly technique by modifying the 2D pattern using lithography techniques before the melting of the polymer hinge is triggered.

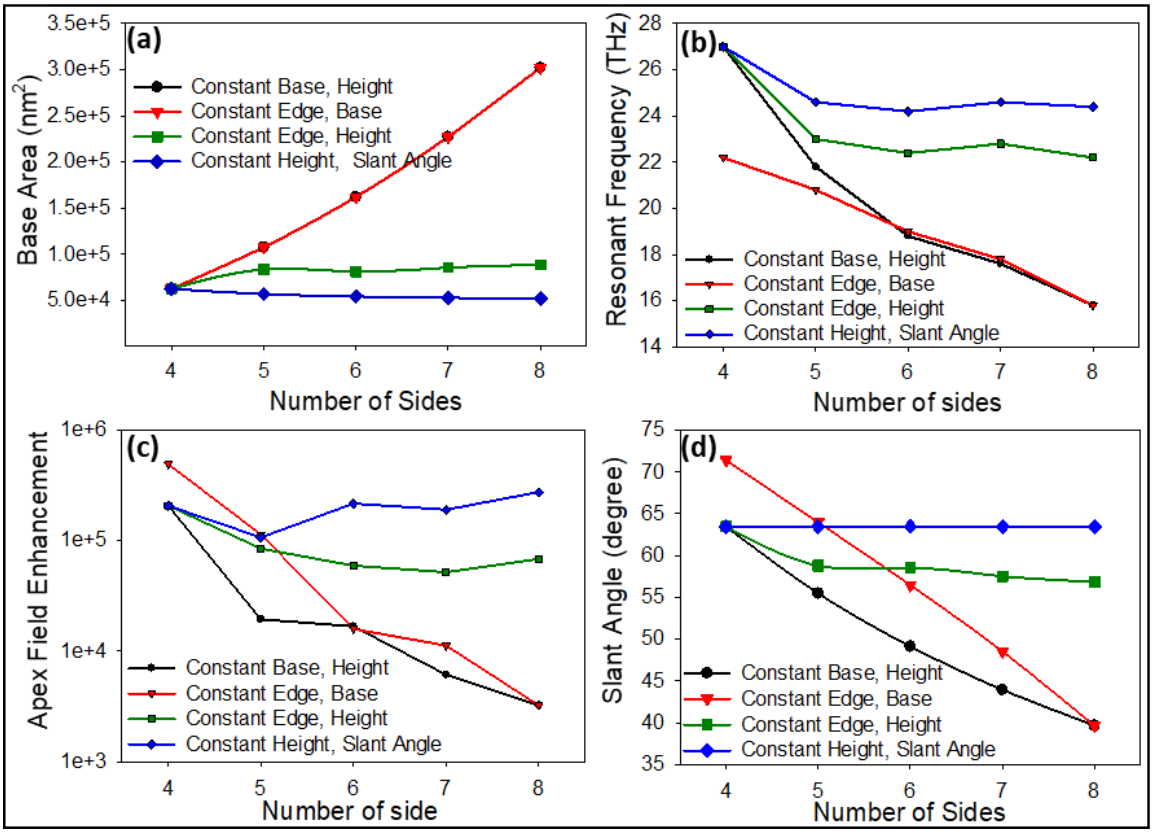

Figure 3.13 Effect of change in number of edges on various parameters for the 3D pyramid including (a) Total surface area of the base of the pyramid, (b) Plasmon resonant frequency, (c) Field enhancement at the apex of the pyramid, and (d) geometrical angle of inclination of the slant surface. The legends refer to the geometrical parameters that were kept constant for the various set of data.

3.4 Radial coupling in 3D graphene tubes

Circular geometries have had varied definitions based on the properties researched within them, some call them 0D, others 1D, but here due to the easy control over the aspect ratio within them, they are called 3D. It should be noted here that these graphene tubes are not carbon nanotubes as they are tightly controlled self-assembled geometries with dimensions much larger than carbon nanotubes. In this section, the plasmon resonances and radial couplings are introduced and analyzed.

3.4.1 Coupled modes in 3D graphene tubes

The strong field enhancement at the edges of the 2D ribbons is significantly modified in the case of curved 3D structures due to the increased field coupling between the opposite edges of the structures. For a 2D graphene ribbon with an incident plane wave, the strongest fields exist at the edges of the 2D ribbon and decay exponentially across the surface of the ribbon. Based on the polarization of incident E-field, the only coupling in 2D ribbons exists across the lateral edges (width) of the nanoribbon (Figure 3.14a); but, due to the large distance between the opposing corners of the ribbon, the field at the

two corners cannot interact. As the curvature is increased to form partially curved tubes, an additional coupling exists between opposing surfaces at the bottom of the tube due to the decreased gap between them (Figure 3.14b, c). Finally, at maximum curvature, two forms of field couplings are induced in 3D graphene tubes (Figure 3.14d). Firstly, similar to 2D ribbons the plasmons along the entire circular edge (circumference) couple to neighboring points along the edge. Secondly, the small diameter of the tube allows the plasmon-generated field to couple across the opening to those points lying radially, horizontally, and vertically across the circumference. The simultaneous edge and radial couplings along the entire circumference form a uniformly coupled mesh across the opening and cause the uniform cross-sectional field at the openings of the tube (Figure 3.14l). The effect of plasmon hybridization in 3D graphene nanotubes is further accentuated when substrate effects are taken into account. Simulations were carried out for 2D and 3D graphene structures in vacuum (refractive index = 1) and a silicon (Si)-like 1.5 μm thick substrate (refractive index = 3.48). A strong degradation and localization of the plasmon near-field enhancement occurs due to the presence of the substrate, limiting the enhanced field to the corners of the ribbon only (Figure 3.14e,i), as opposed to 2D graphene in the vacuum where a uniformly decaying field can be seen across the surface of the ribbon.

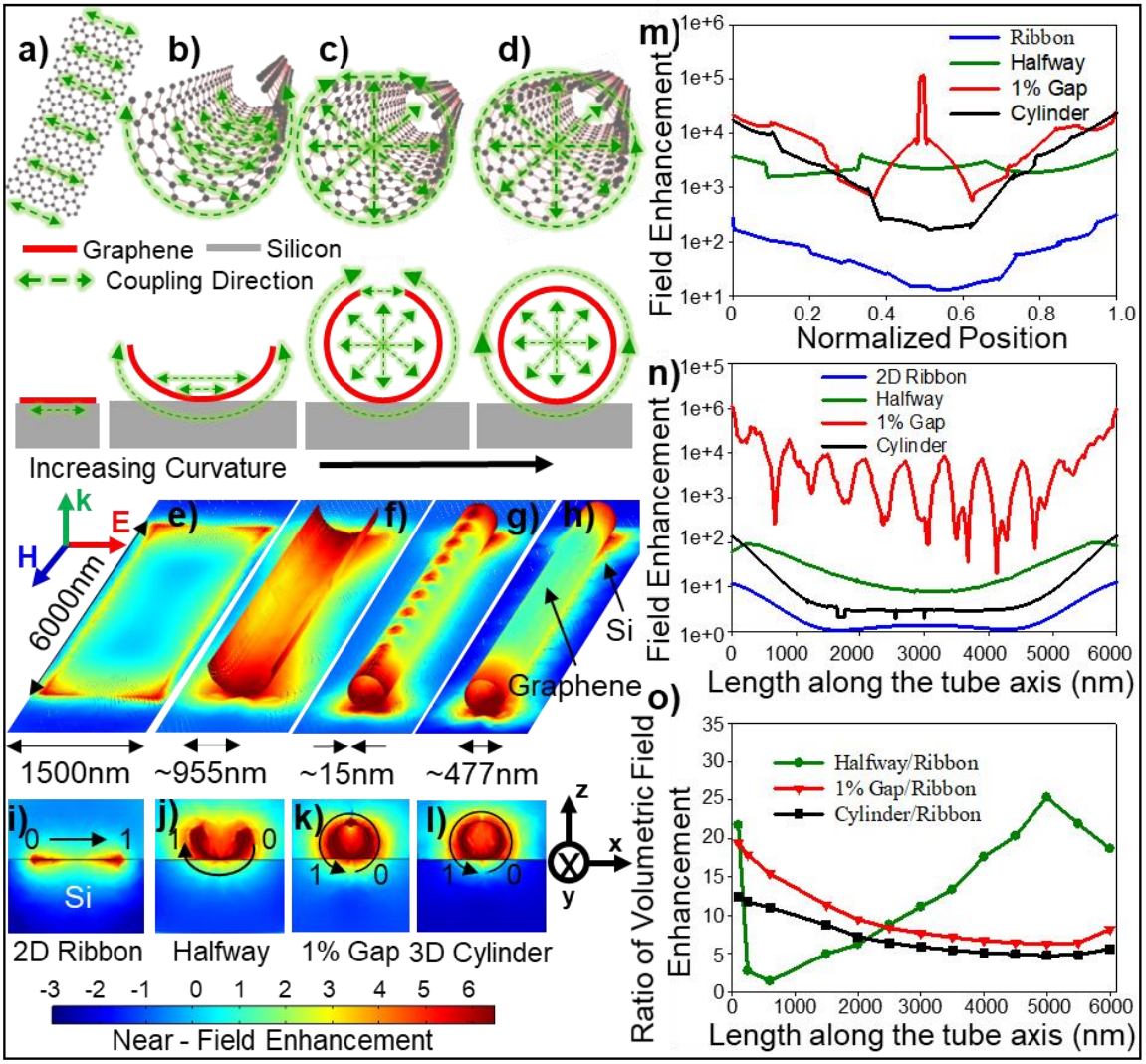

Figure 3.14 (a-d) 3D and cross-sectional schematics illustrating the coupling directions in 2D ribbons and 3D partially and completely curved tubes. (e-h) The near-field enhancement plotted on the surface of a a) 2D ribbon, b, c) partially curved tubes, and d) completely curved tubes. i-l) The cross-section images show the field enhancement in the ZX plane when an imaginary cut plane is placed at the edge of the structures at 6000 nm. m) The field enhancement in ZX plane along the circumference at the ends of the structures

(see the arrow in e-h)). n) The field enhancements at the center of the gap in the halfway and 1% gap curved tubes, at the surface of the completely curved tube along an imaginary edge, and on the surface of the ribbon. A strong propagating mode is seen along the edge of the cylindrical structure with 1% gap. o) The volumetric field enhancements along the length of the 3D structures are analyzed based on their ratio to the volumetric field in a 2D graphene ribbon. Volumetric enhancement is calculated by volume integrals of the field inside the 3D structures and for an imaginary rectangular box of thickness 119nm placed on the 2D ribbon with lengths increasing from 100 nm to 6 μm.

When 2D ribbons are curved, the spatial overlap of graphene with the underlying substrates decreases, leading to a corresponding decrease in the substrate influence on the field enhancement. As a result, the partially (50% curved shown in Figure 3.14f,j and 99% curved shown in Figure 3.14g,k) and completely curved nanotube (Figure 3.14h,l) structures retain a stronger near-field enhancement spreading over a larger area, similar to freestanding graphene structures in vacuum. For the 2D ribbon, the field enhancement at the edges ($\sim 3 \times 10^2$) is two orders of magnitude lower than the enhancement for a graphene ribbon in vacuum, which further decays by an order of

magnitude when moving to the center of the ribbon (Figure 3.14m, with normalized position taken across the ribbon width as shown in Figure 3.14i). On the other hand, for the halfway curved nanotube, a line-type substrate contact (Figure 3.14f,j) leads to minimal spatial overlap, as opposed to 100% surface-area contact in 2D ribbons. The lower overlap with the substrate, stronger field coupling between the points on the circumference of the tube as well as radial field coupling across the nanoscale openings of the tube leads to an enhancement (~5.5×10^3) that is two orders of magnitude stronger than in 2D ribbon and remains constant across the width of the partially curved nanotube (Figure 3.14m, with normalized position taken along the semi-circular circumference as shown in Figure 3.14j). Similarly, the completely curved nanotube (Figure 3.14h) undergoes an even stronger (~2.3×10^4) enhancement, which is nearly two orders of magnitude stronger than for a nanotube in vacuum through additional localized enhancement occurring between the curved graphene and substrate alongside twice as much radial coupling along the circumference at the opening of the nanotube. The simultaneous localization and radial couplings give rise to a virtual cross-sectional area of strong field enhancement at the opening of the completely curved nanotube (Figure 3.14l). The 3D plasmon couplings at the openings of the completely curved nanotubes induce a total integrated edge enhancement

of 1149, which is 13 times higher than the total field enhancement of 87 at the edge of the 2D ribbon. Moreover, the field enhancement induced in the 3D nanotube can be further modified via controlling the gap in the nanotube.

A sub-10 nm gap may exist between the two curved edges joining together which introduces the possibility of edge effects along the length of the structure. Simulations for the 99% curved nanotubes (Figure 3.14g,k) reveal strong interactions between the two edges separated by a distance of only 15 nm that further enhances the coupled field at the center of the gap by an order of magnitude (Figure 3.14m). It should be noted that inside the 15 nm gap of the 99% curved nanotube, the field enhancement is 300 times stronger than the maximum enhancement obtained even at the edge of the 2D ribbons (Figure 3.14m). The geometrically confined field in the partially curved nanotubes exists along the entire length of the nanotubes (Figure 3.14g). This leads to a field enhancement 4 orders of magnitude (Figure 3.14n) stronger when compared to that at the center of the 2D ribbon. Oscillations in the field strength, seen in Figure 3.14n, indicate the highly confined propagating mode existing within the gap of the 99% curved nanotube. The strongly confined, high enhancement, propagating edge modes are particularly attractive for the development of graphene-based optoelectronic devices including plasmonic waveguides to achieve exceptional propagation lengths and figure of merit.

The completely curved nanotube does not show propagating modes, thus, supporting the conclusion that modes observed in the partially curved nanotubes are purely edge modes. However, at the center of the completely curved nanotubes, even in the absence of the edge modes, the 3D coupling enables field enhancement that is an order of magnitude stronger than at the center of 2D ribbons. The strong uniform field enhancement at the openings of the nanotubes induced by radial and edge couplings (Figure 3.14j-l) can also be termed as volumetric enhancement, which is computed as an integral of the field enhancement at the cross-section of the openings. The total volumetric enhancement for the uniform field in a halfway curved nanotube is 20 times higher than the volumetric field in 2D ribbons over the full length (6 μm) of the structures (Figure 3.14o).

3.4.2 Geometrical parameters within 3D tubes

The pyramidal and cubic nano-architectured 3D graphene realize giant hotspot surfaces and extreme volumetric fields; however, for a given wavelength, the maximum point ($I_{g,max}$) and edge ($P_{g,max}$) enhancements are lower than in 2D graphene ribbons. This presents a disadvantage for application in waveguides and interconnects that require high intensity

confined modes for long propagation lengths. The self-assembly of 2D ribbons results in hollow, open-ended, cylindrical 3D graphene tubes that undergo plasmon hybridization even in the absence of adjoining edge and face coupled surfaces that exist in polyhedral prisms. The openings of the tube retain the strong edge enhancements of the 2D ribbon under an incident plane wave; however, the simultaneous coupling of the field at every point along the edge of the openings and points lying radially across the small diameter causes a stronger field enhancement that engulfs the circular perimeter (uniform cross-sectional field) at the opening of the tube (Figure 3.15a). When the circumference ($C = \pi D$, where D is the diameter) is varied between 500 and 50 nm keeping length of the tube $L = 4C$ (Figure 3.15b), the maximum near-field enhancement obtained scales exponentially similar to the pyramids and cubes owing to an increase in plasmon resonant frequency. The strong $I_{g,max} \sim e^{12}$ is concentrated only along the perimeter at the opening of the tube at C = 500 nm. However, at smaller circumferences of the tube (C = 100 and 50 nm), the uniform cross-interference of the field at every point on the circular opening with field from other points on the edge lying radially opposite creates a virtual surface of strong and uniform near-field enhancement across the entire cross-section of the tube opening (Figure 3.15a, cross-sectional views). The near-field at the opening of the tube decays rapidly toward the middle of the tube

covering only 8%, and 16% of the entire length of the tube at C = 50 and 500 nm, respectively. Thus, providing the tube with a lower volumetric enhancement compared to 3D cubes and pyramids, which still increases exponentially at lower tube dimensions due to increased interference and coverage as the size of tube (L and C) is decreased (Figure 3.15b).

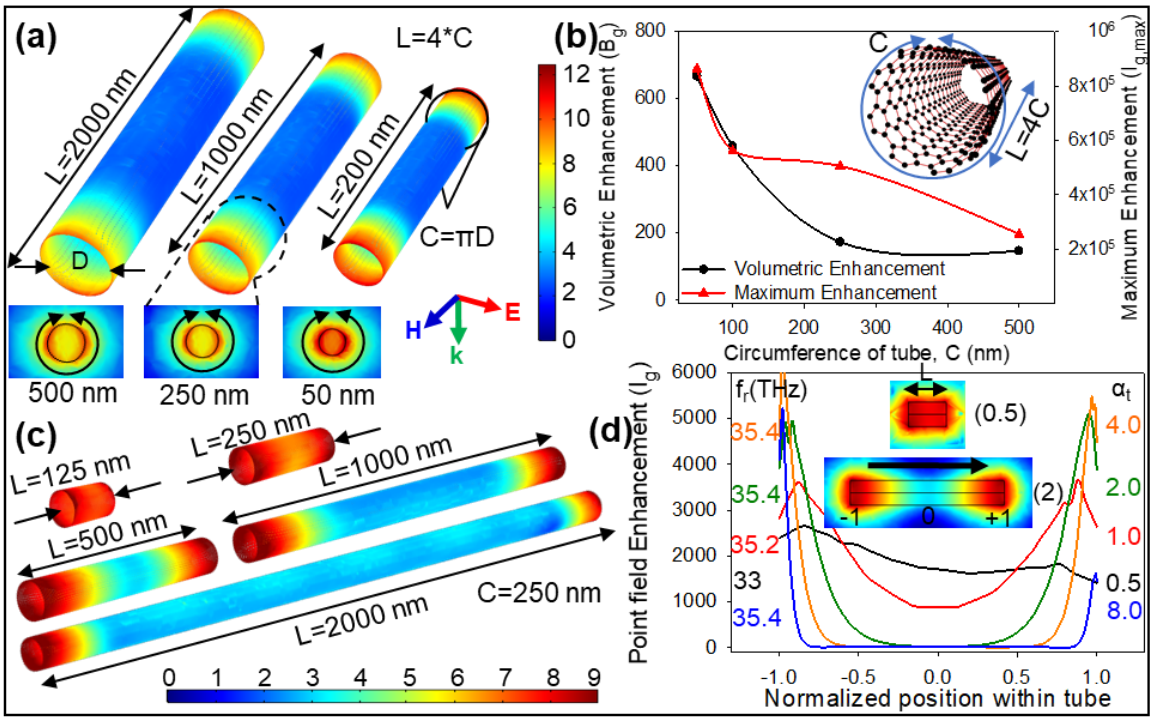

Figure 3.15 Simulation results for 3D graphene tubes for varying size and dimensionality. (a) Simulated near-field enhancement on the surface of the self-assembled tube, with cross-sectional side views at the opening of the tube demonstrating the increase in the enhancement across the length of the tube for decreasing diameter and the uniform circular enhancement at the opening of the tube at C = 50 nm. (b) Exponential increase in the maximum near-field

enhancement and the volumetric enhancement for decrease in the size of the tube while maintaining a constant $\alpha_t = 4.0$. (c) Field enhancement plotted on the surface of tubes for constant C = 250 nm and varying the length of the tube such that $\alpha_t = 8$, 4, 2, 1, and 0.5. (d) Enhancement plotted at the center of the tube across the entire length (as indicated by the arrow) demonstrating the decay to zero toward the middle of the tube for $\alpha_t = 2$, 4, and 8 and the nonzero field at the center for $\alpha_t = 0.5$ and 1.0; the inset depicts the enhancement for $\alpha_t = 0.5$ and 2.0. [183]

For a tube of circumference 250 nm, at $\alpha_t = L/C = 4.0$ the strong near-field enhancement is limited to the perimeter of the circular edge openings, resulting in extreme point and edge enhancement but covering only 11.6% of the length of the entire tube. For higher α_t values (2–8), the openings of the tube are too far apart to result in any interference at the center of the tube, resulting in a strong decay of field toward the middle of the tube, *i.e.*, decaying from ~5000 at the openings of the tube to ~0 at normalized positions of 0.8, 0.6, and 0.4 within the tubes (Figure 3.15d). However, at low values of $\alpha_t = 1.0$, the smaller distance between the openings of the tube facilitates field interference at the center of tube resulting in a strong field at the center that reduces only by a factor of 4 compared to the field at the opening (Figure

3.15d). If the dimensionality parameter, α_t, is reduced to 0.5, the strong interference at the center of the tube due to the smaller length (L = 125 nm) creates a nearly uniform volumetric enhancement across the entire length of the 3D cylindrical tubes. The volumetric enhancement is increased by a factor of 20 between α_t = 4.0 ($B_g \sim 173$) and 0.5 ($B_g \sim 2222$), offering advantages in the detection and monitoring of target specimens, such that the specimens flowing inside the tube can be monitored throughout their life cycle without hindering their natural response by adhesion to the graphene surface.

3.4.3 Edge-driven resonances within 3D tubes

The intensified field at the openings of the nanotubes decays strongly towards the middle of the tube covering only 11% of the total length of the tube. However, if the two corners of the curving 2D ribbon are not allowed to completely touch each other, a partially folded tube structure is created with a small gap slit that runs longitudinally throughout the length of the tube structure (Figure 3.16a). The closely spaced edges on either side of this gap can efficiently launch edge plasmons by confinement of the incident photons. Similar to the 3D cubes, the capacitive coupling and confinement efficiency between the edges is dependent on the distance between the two edges. For

smaller gap percentages, a strong propagating edge mode is seen across the length of the cylindrical tube structure. Thus, transforming the surface enhancement mode in zero-gap cylindrical structure (comparable to one-sided 2D nanodisks) to propagating edge enhancement mode in segmented cylindrical nanotubes.

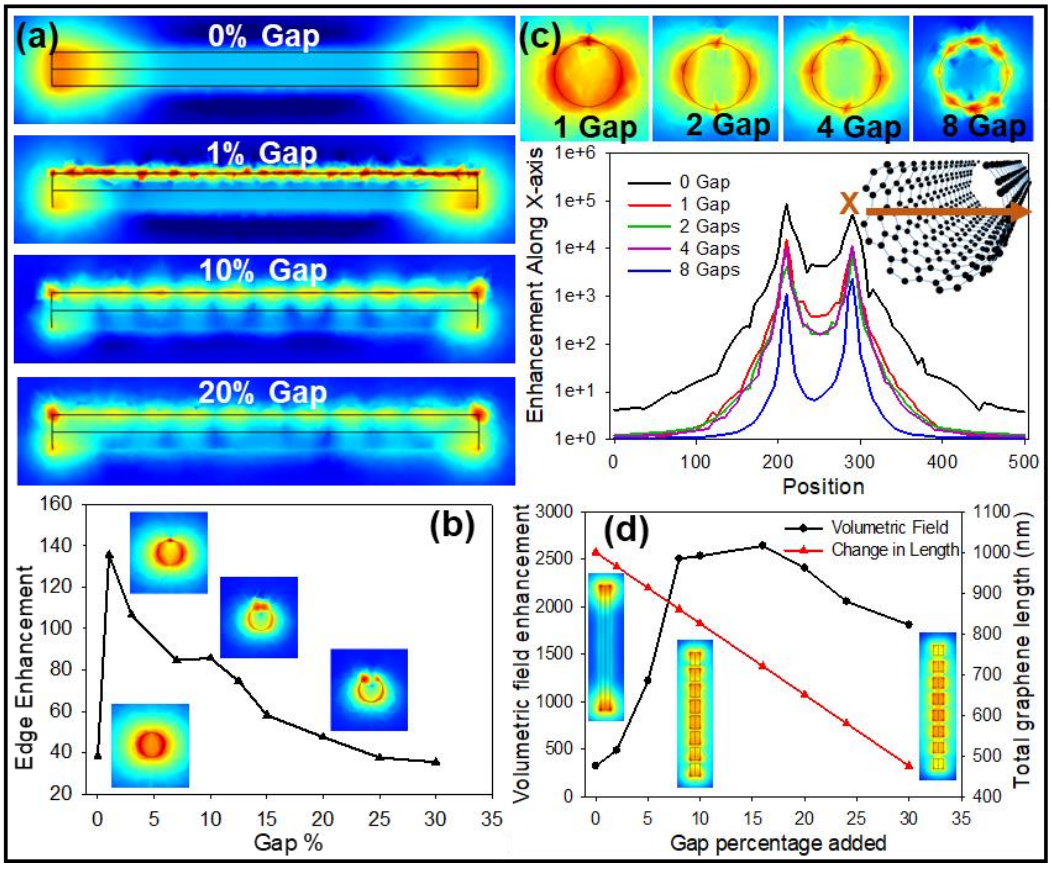

Figure 3.16 Simulated electric-field enhancement plotted along a virtual placed on the edges introduced within the 3D nanotube showing the propagating edge modes. (b) Variation in the edge enhancement for the 3D nanotubes plotted as a function of the gap length introduced, showing the initial

increase in edge enhancement which decreases as the distance is increased. (c) Simulated cross-sectional images of the lower scattered field at the opening of the 3D nanotubes with increasing number of longitudinal gaps. The graph plots the corresponding electric field enhancement along X-direction such that the center of the circular opening exists at X=250nm and radius of the tube is 40nm. (d) Effect of increasing gap sizes when the gap is added in the transverse direction for a tube of constant total length of 250nm and radius 40nm.

Furthermore, as the number of edges is increased by adding more gaps to the 3D nanotubes, the scattering of the field at the openings is strongly reduced to almost 0, instead strongly confined gap edge modes are created which are especially beneficial for achieving targeted fields (Figure 3.16c). A curved ribbon of width 250 nm yields a cylindrical tube of radius ~40nm. For 0 gaps, this tube structure exhibits a strong scattered field even at a distance of 40nm from the circumference. Thus, creating a scattering cross-section twice as large as the cross-section of the tube. However, if the tube structure is fabricated with incrementing edges, the scattered field is confined to the longitudinal gaps of the structure such that for the 8 gap nanotube with 16 edges introduced, the scattered field exists to a maximum length of 5 nm outside the circumference of the tube. Only those gaps that are not perfectly

perpendicular to the incident E-field can launch edge plasmons as demonstrated by the lack of changes in confinement between the 2 and 4 gap 3D nanotubes. It is also important to note that the maximum enhancement for the nanotube structure does not change by the introduction of additional edges. The lower peak enhancement seen in Figure 3.16c is associated with the maximum enhancement being moved to the edges at the gaps introduced in nanotube. For each of the gaps, at the nearly constant plasmon wavelength, the width of the propagating modes remains constant and varies in intensity by the width of the gaps and number of gaps introduced. Similar to the gaps added to the 3D nanotubes in the longitudinal direction, the number of edges can also be increased by the addition of gaps in the transverse direction.

Unlike the longitudinal gaps which affect the surface and edge enhancement, the transverse gaps affect the surface and volumetric enhancement. For a tube of radius 40nm as before and constant total length 1000nm if 8 transverse gaps are introduced, the length of the individual segments within the tube is short enough that the two openings of the segments can couple to each other, introducing a uniform coupled field engulfing the entire segment. At shorter gap distances, the volumetric fields at the edges of neighboring segments can also couple to each other to yield volumetric enhancement extending throughout the length of the tube. This results in an 8-

fold increase in volumetric enhancement between the zero-gap tube structures compared to an eight-gap tube with 16% gap lengths (Figure 3.16d). The volumetric enhancement decreases beyond 16% gap as a lower coupling exists between the neighboring segments that the proportional increase in the volumetric field within each segment cannot overcome. Thus, the addition of transverse and longitudinal edges in the 3D nanotubes can severely modify their enhancement between edge, surface and volumetric enhancement based on the desired application.

3.5 Comparison of the plasmon hybridization in diverse 3D graphene geometries

Even though all three architectures and the 2D ribbon demonstrate a similar trend of exponential increase in enhancements with varying plasmon wavelength (size of the structures), the 3D architectures induce distinct 3D plasmon hybridization modes and field modifications on varying the ratio of dimensions comprising them. The strong point-based enhancement in tubular graphene extends over the entire cross-sectional edge at the openings of the

tubes unlike the enhancement concentrated to single point vertices in 2D ribbons. For pyramids, a lower edge-based enhancement is induced under TE excitation creating a strong field at the base but not at the apex of the pyramid. 3D cubic graphene does not demonstrate strong point and edge-based enhancements compared to other 3D architectures. However, the hotspots in the cubes induce a uniformly strong field enhancement over a large area. For the pyramids under TM excitation, the uniform interference from slant edges in pyramids renders the base of the pyramid with a higher surface enhancement compared to cylindrical tubes. Furthermore, the large hotspot surfaces in cubes and base-apex couplings in pyramids create strong fields within the volume of both these structures, hence, extending conventional point and edge-limited plasmonic field enhancements to large surface areas and volumes based on the type of coupling induced in the 3D nanoarchitectures.

For 2D graphene ribbons with the number of edges varied from 1 (circular disk) to 8 (regular octagon) with a constant length of each edge equal to 250 nm to maintain a nearly constant resonant frequency. The maximum near-field enhancement occurs for the 5-sided pentagon ribbon with 4 edges inclined at an angle with respect to incident E-field, hence, achieving maximum interference from plasmon reflections. The 2D ribbons with 3 and 4 edges contain only 2 edges not parallel to incident E-field and as a result exhibit

smaller field enhancement. The hexagonal, heptagonal, and octagonal ribbons also contain more than 2 edges not parallel to the incident E-field, however, the larger distance between them results in lower constructive field interference as result of rapid field decay. Thus, exhibiting a lower maximum field enhancement as evidenced in Figure 3.17. The lower field enhancements throughout the edges of these ribbons consequently affect the total surface field that can be extracted, giving a maximum surface-based enhancement for the 5-sided ribbon. Unlike, the limited tunability of surface and point modes in edge-driven 2D graphene resonance, the 3D pyramids with strongly coupled resonance through their edges offer a nearly 3 orders of magnitude variation between the surface, edge, and point-modes through tuning of geometrical edge parameters.

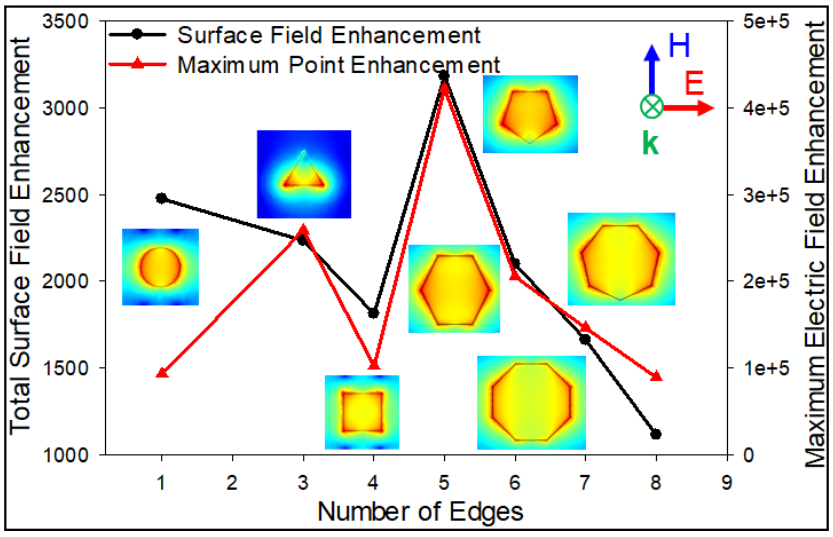

Figure 3.17 Graph showing the effect of the number of edges on the plasmon enhancement behavior in 2D graphene structures with a constant edge length

of 250nm. The number of edges is varied from 1 to 8 and the corresponding maximum electric field is simulated. The corresponding surface field enhancement is computed by integrating the field on the surface normalized to incident wave. The inset shows the polarization of the incident electromagnetic radiation.

The results are summarized in Figure 3.18 comparing the enhancements in 2D and 3D architecture graphene of the same dimensions (similar resonant frequency), which demonstrates that the maximum electric-field, i.e., point-based enhancement, occurs in cylindrical tubes and at the vertices of 2D ribbons, followed by pyramids and last cubes (Figure 3.18, Point). A direct consequence of the maximum point enhancement is the strongest edge-based enhancement induced in 3D tube and 2D ribbon. The edge-based enhancement in tubes and ribbons is followed by pyramids and last in cubes that demonstrate lower edge-based enhancements since their maxima are spread out over larger hotspot surfaces (Figure 3.18, Edge).

Thus, the strongest area-based enhancement occurs in cubes owing to the large hotspot surfaces followed in order by the tapered surfaces of the pyramid, circular surface of the tube, and finally the 2D ribbon (Figure 3.18, Surface). Finally, the coupling between the slant surfaces and the interference

of fields between the apex and base of the pyramid render it with the strongest volumetric enhancement, followed by the large hotspot surface cubes, then the tube with virtual cross-sectional areas of uniform enhancement, and last 2D ribbons with minimal volumetric enhancement (Figure 3.18, Volume).

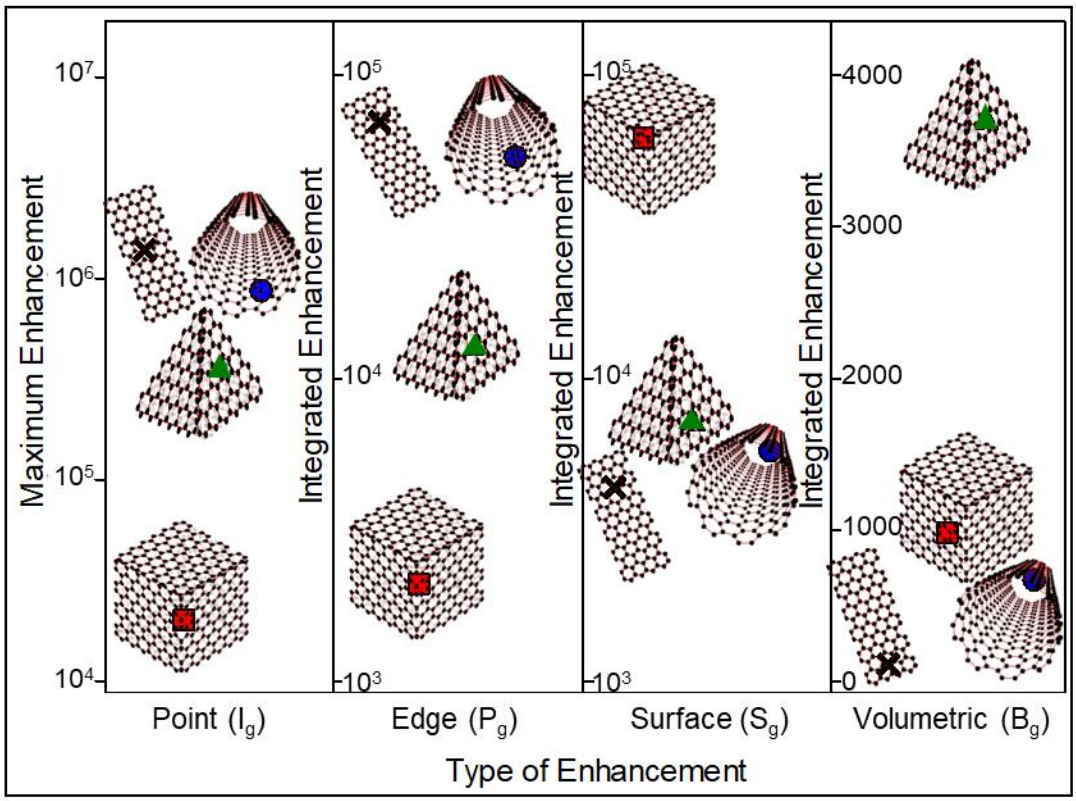

Figure 3.18 Evaluation of plasmonic enhancement modes in 2D and 3D graphene nanostructures. Comparison between the highest intensity of the point-based, edge-based, surface-based, and volumetric near-field enhancement induced in the hollow 3D pyramidal, cubic, tubular graphene, and 2D graphene ribbon. The resonant frequency for each nanomaterial was centered around 45 THz by selecting the geometries to be similar in size. The

symbols behind the graphene illustrations correspond to the location of the actual data values on each of the y-axes. [183]

Chapter 4

Mid-IR Chiral plasmonics in 3D Graphene

4.1 IR vibrational circular dichroism spectroscopy

Chirality or circular dichroism (CD) is defined as the polarization-dependent asymmetric response to incident light caused by breaking of mirror symmetry in materials. For a circularly polarized wave passing through a chiral medium, a differential absorption exists for left (LCP) and right (RCP) circular polarizations, resulting in the transmitted wave having elliptical polarization [164]. For an achiral medium, the wave equation can be broken down into three individual spatial components. However, for chiral media, a cross-coupling exists between the spatial components of the wave. For a wave propagating within a chiral media, this induces different refractive index for different polarizations which in turn causes different propagation constants. For unpolarized light, a uniform refractive index (n) exists for isotropic chiral

media. In the case of LCP (+) and RCP (-), the refractive index for respective polarization is given by the equation $n\pm = n \pm \kappa$, where κ is the chirality parameter.

Chirality can be found in nature as well as in artificial materials and structures [165]. Most biological molecules are chiral in nature with examples that include essential amino acids, DNA, proteins, and sugars. The chiral response of biological molecules can lead to vital information about their secondary structure composition (% helix, sheet, turns, etc.) from the peptide bond region, tertiary structure fingerprint, conclusions about the overall structural features of proteins, conformational changes in proteins caused by binding of ligands, protein folding [166]. Thus, making the chiral response of biological molecules more beneficial than traditional spectroscopy techniques. Chiral responses in biological molecules can be divided into two modes, firstly caused by electronic transitions in UV and visible regime, and secondly, those caused by vibrational modes in the IR regime. Vibrational CD in the IR region is especially attractive since all protein molecules possess a characteristic IR vibration fingerprint without the need for additional chromosphere as in the case of UV- CD [167]. Furthermore, the higher spectral resolution of CD as compared to UV-VIS makes it a highly sought-after research area since a reliable response can be obtained even without electron transitions. However,

the weak absorption of the IR light by the low molecular weight biomolecules leads to low differential absorption signals transduced of the order of 10^{-4}-10^{-5}. Two solutions can be primarily applied to enhance the chiral signal from biomolecules, namely, increasing the path length or concentration of the targeted analyte. However, increasing the path length causes lower wave intensity at the detectors, resulting in a drastic drop in the signal to noise ratio. Thus, CD spectroscopy techniques require higher analyte concentrations in the micro and milligram range to produce a very small differential absorption signal [168]. Several techniques have been investigated to increase the sensitivity for circular dichroism spectroscopy through the use of quantum-mechanical weak value measurements, and minimization of the achiral interactions. Although these measurement schemes offer higher contrast signals, the actual absorbance intensity still remains low. Furthermore, due to the rapid decline in the output signal, several measurements need to be taken to a reliable response. In this chapter, hybrid geometries are investigated that can break the mirror symmetry for high-intensity chiral graphene plasmonics and the resulting geometrical parameters that can control the degree of chirality.

4.2 Theory and simulation setup

The limitations of conventional chiral structures have prompted research into plasmon-enhanced circular dichroism which can reveal far more information that traditional plasmon-enhanced spectroscopy. Similar to plasmon-enhanced surface spectroscopy techniques, geometrically chiral plasmonic structures can be used for the enhancement of the differential absorbance signal [169]. However, the prime candidate for tunable IR plasmonics, graphene, is achiral in nature. One of the primary requirements of chirality is finite rotation and lack of mirror symmetry in the out-of-plane direction, which cannot exist for any 2D materials defined on a planar substrate. A truly 2D material can only interact with the incident field in-plane, allowing no modification out-of-plane; thus, it cannot rotate light in the direction of propagation. This has prompted research into inducing anisotropy in the graphene conductivity by the addition of twisted bilayers, magnetic fields or variable doping under a magnetic field [170-172]. However, each of these techniques deteriorates the conventional graphene plasmonic enhancement in graphene and has only been able to achieve a 2% theoretical chirality due to the 2D nature of graphene [173].

While some theoretical geometries have shown a larger graphene chirality, there have been no routes explained that would allow the fabrication of those complex geometries with the sensitive graphene properties. In the previous chapters, a self-assembly approach was demonstrated as well as 3D graphene geometries were explored to enhance the plasmon response of graphene. Recently, the kirigami and origami approaches have been utilized for metallic chiral structures [174,175]. Combining the self-assembly approaches with 3D graphene properties can achieve a chiral graphene nanostructure with tunable properties for vibrational CD spectroscopy. However, each of these architectures such as the cube, tube, and other forms lead to a symmetric configuration that cannot be used for achieving a chiral optical response (Figure 4.1a,b).

Helical resonant structures have been shown to deliver the strongest chiral properties [176]. In such a helical graphene structure, the axis of the helix lies parallel to the direction of the incident electric field. The plasmon propagation is restricted to a twisted path along the helix in turn producing time-varying electric and magnetic dipole moments parallel to the axis with their resulting emitted electric field perpendicular to each other. The resulting scattered electric field is rotated at an angle with respect to the incident electric field. Thus, the plane of vibration of the resulting electric field, which is a sum

of the scattered and incident electric fields, experiences a rotation that is proportional to the handedness of the helical structure. Using the self-assembly approaches, a similar lateral helix structure can be realized from graphene (Figure 4.1b).

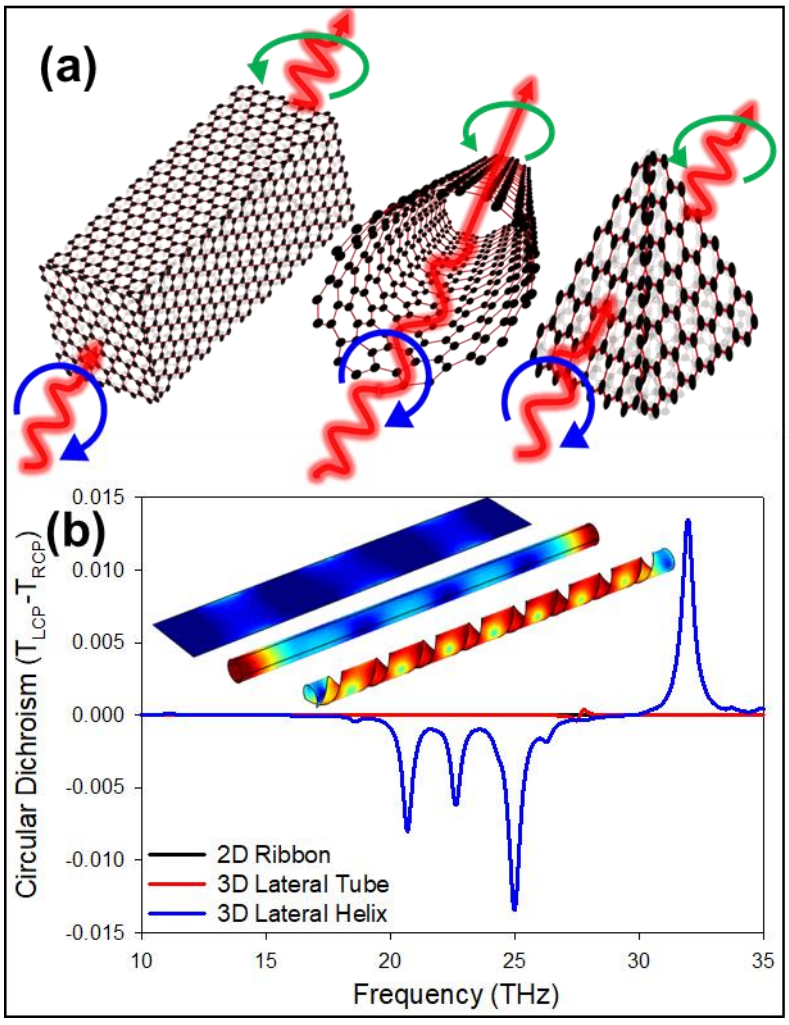

Figure 4.1 (a) Illustration of the 3D graphene-based structures when illuminated by a circularly polarized wave with the output wave having elliptical polarization due to chirality. (b) Achiral response for 2D graphene

ribbons and 3D graphene tube. The lateral graphene helix shows a small chiral response of 1.5% due to the low path length and lateral position.

The measure of chirality within these structures can be simulated using a few different techniques such that the chirality parameter (κ) can be broken into a real part that is determined by optical activity (θ) and an imaginary part determined by ellipticity (η). Optical activity measures the rotation of the incident light by which linearly polarized light changes polarization. Here, the differential absorption (ΔA) between the left and right circularly polarized wave is simulated to reflect the optical activity as given by the relation $\theta = 32.98\ \Delta A$. The left and right circular polarizations are defined for Comsol ports using their Jones matrix. As seen in Figure 4.1b, the chiral response of the lateral helix structure is very low at only 1.5% chirality. However, the response can be increased by over an order of magnitude by orienting the helical structures to be vertical such that the wave is incident perfectly parallel to the helix axis corresponding to the description of chiral helixes above, thus increasing the path length and degree of asymmetry (Figure 4.2).

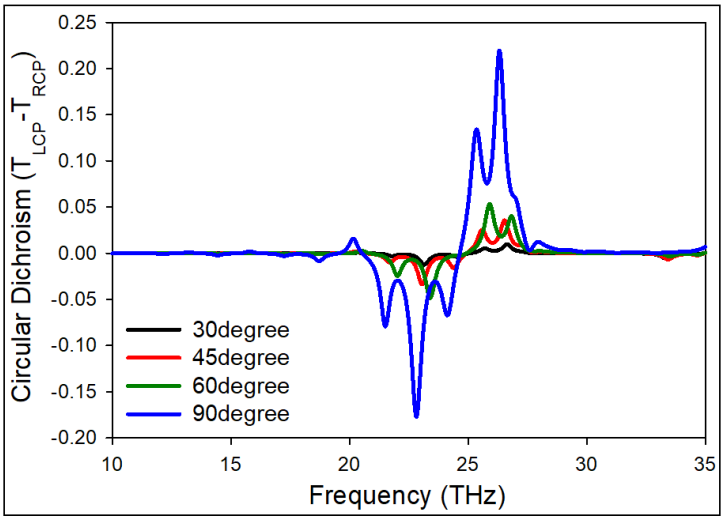

Figure 4.2 Graph showing the increase in chiral response when changing the angle of inclination of the helical structures with respect to the underlying substrate going from lateral to vertical tubes.

4.3 Optical activity in vertically aligned tubular graphene helixes

Based on the discussion in the previous chapter, tubular graphene helixes are investigated to begin the theoretical understanding of chiral graphene structures and the parameters controlling them. One of the driving features of the chirality in helixes is the number of turns in the helix, which in turn controls the number of rotations between the scattered electric field and

the incident electric field and increases the path length over a given length of helix axis.

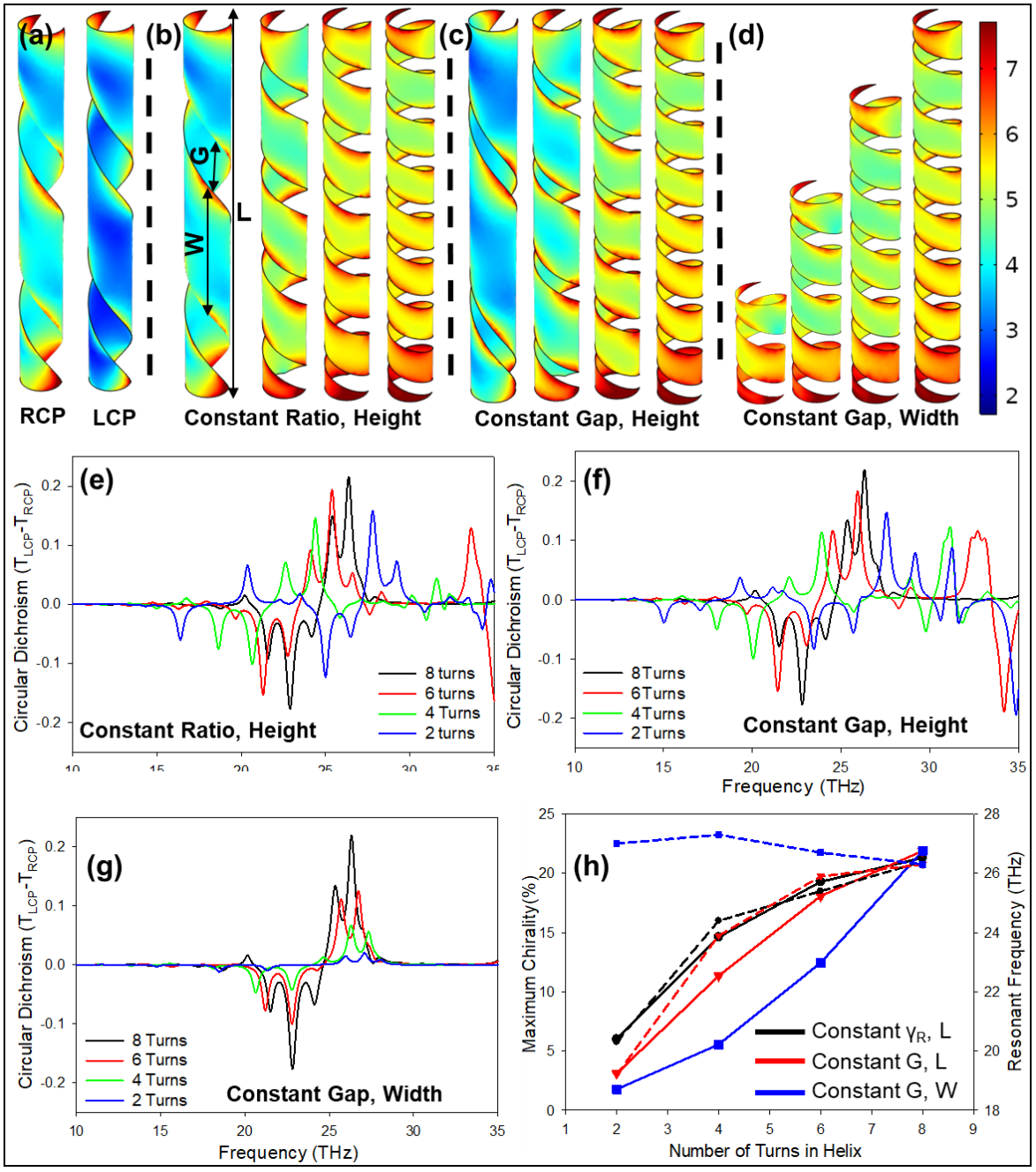

Figure 4.3 (a) Surface near-fields plotted on a helix with 2 turns for LCP and RCP polarizations at the frequency of maximum chirality in their absorption.

(b-d) Surface near-field enhancements plotted on a log scale at the frequency with the maximum absorption difference for varying helical turns while maintaining various geometrical parameters as a constant. (e-g) Differential absorption signal obtained for the LCP and RCP waves for the structures shown in b-d. (h) Graph showing the variation in CD and the resonant frequency (plasmon wavelength) as a function of the helical turns with the varying geometrical parameters.

For the helical graphene tubes with 2 turns it can be clearly seen that for the given handedness, the RCP incident wave induces a stronger plasmon driven surface-field as compared to LCP induced plasmon fields corresponding to a higher absorption seen for the RCP wave in the frequency spectrum at 20.3 THz (Figure 4.3a). The helical structure is formed from seemingly spiral ribbons that are a result of assembling tilted ribbons on the surface of a tube. For such helical structures, three geometrical parameters can be defined i.e. the width of graphene ribbons (W), gap between ribbons (G), and the length of the helix (L) as shown in Figure 4.3b. The number of turns in these helical structures can be varied in three ways to achieve different chiral responses and plasmon enhancement. For a helix of constant height, the number of turns can be varied from 2-8 while either keeping a constant ratio of width to gap (γ_R)

such that both gap and width scale down simultaneously (Figure 4.3b,e) or a constant gap length such that the width decreases as the number of turns increases (Figure 4.3c). At eight turns all the helical structures have the same dimensions with different geometrical parameters at two turns.

For the latter case, a sharper decline is seen in the chiral response (Figure 4.3f) because of the larger values of W and γ_R cause a larger plasmon wavelength, enabling the cross-coupling between the ribbons across the gap that pulls the chiral response down towards that of a lateral tube seen in Figure 4.1. In order to maintain a nearly constant plasmon wavelength across structures of varying number of turns, the turns can be varied while maintaining a constant value of gap and width but reducing the actual helix length (Figure 4.3d). However, in this case the decreasing path length leads to the largest decay in chiral absorption (Figure 4.3g). These results can be summarized as shown in graph for Figure 4.3h showing the linear v/s exponential increase with number of turns between the set with a constant ratio and length compared to the set with constant gap and width.

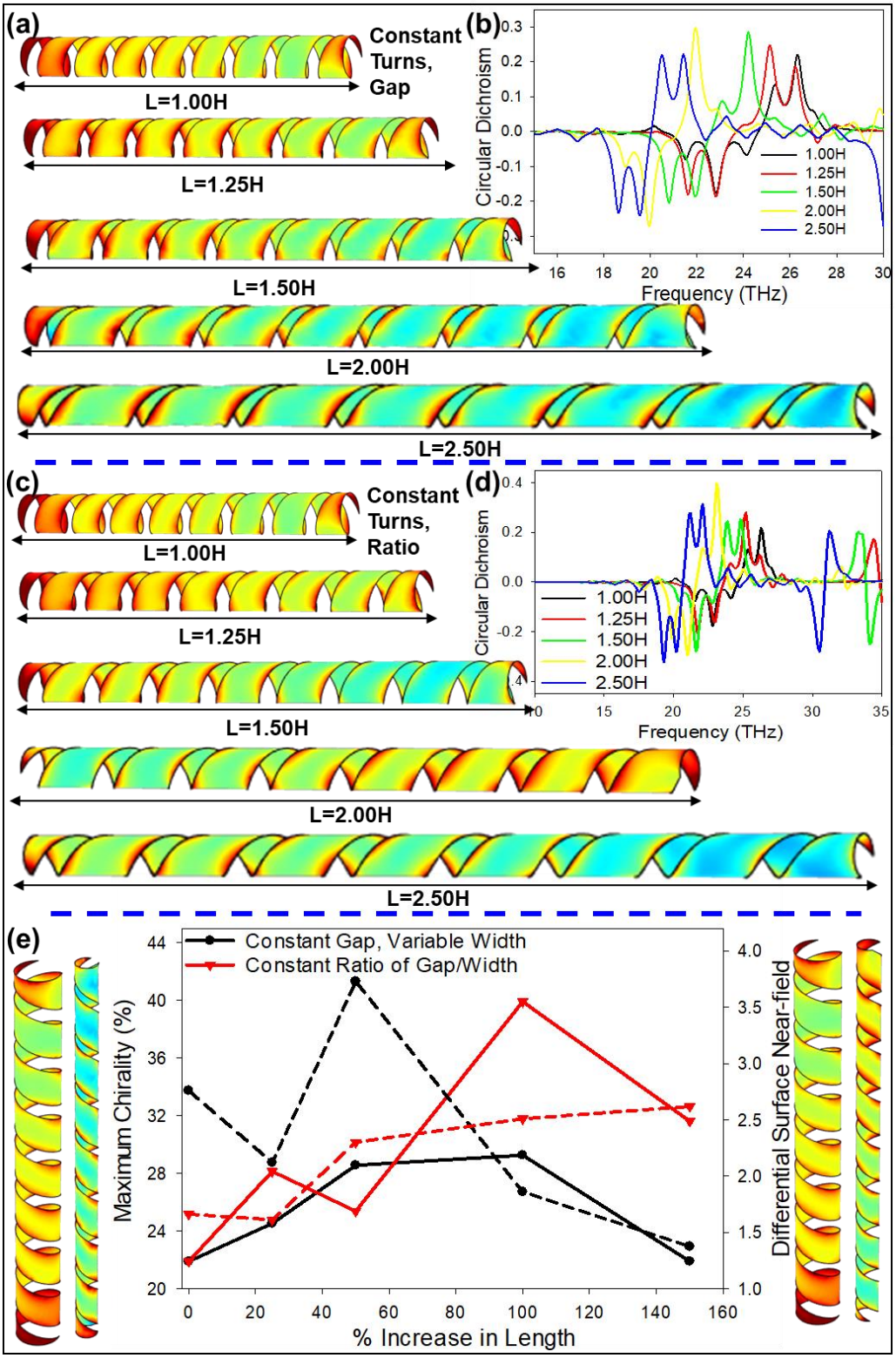

Figure 4.4 (a, b) Surface near-fields and chiral frequency spectrum with increasing length of helix while maintaining a constant gap length and

increasing the width of the ribbons. (c, d) Surface near-fields and chiral frequency spectrum with increasing length of helix while maintaining a constant ratio of the gap and width such that a proportional increase is done in both the gap and width. (e) Summary graph showing the chiral response and ratio of the total surface-field obtained for RCP and LCP polarizations for the different lengths.

The effect of path length (helix length) can be studied in these structures to find the resulting CD response. Similar to the varying of number of turns, varying the length of the helical structures also affects multiple geometrical parameters at the same time. Hence, the increase in length can be realized either through an increase in ribbon width for a constant gap (increasing γ_R) or through a proportional increase in gap and width of ribbons (constant γ_R). In the former case, the increased width leads to achiral cross-coupling between adjacent ribbons much like in Figure 4.3, this is proven by the stronger edge fields compared to surface fields as shown for L=1.50H - 2.50H in Figure 4.4a and a proportional saturation and finally decrease in chirality at L=2.50H (Figure 4.4b). For the latter case, this achiral edge-based cross-coupling happens at only L=2.50H where the plasmon wavelength increases as a square function (as discussed in Chapter 1) but the proportional gap has only been

scaled linearly (Figure 4.4 c,d). These phenomena result in the maximum chirality of ~29% to be obtained for a 100% increase in path length for the first case and a chirality of ~40% for the second case (Figure 4.4e). The small decrease in chirality for some of the increases in path length can be easily explained through mode switching as evidenced by the change in near-field patterns and ratio of peaks in the frequency spectrum.

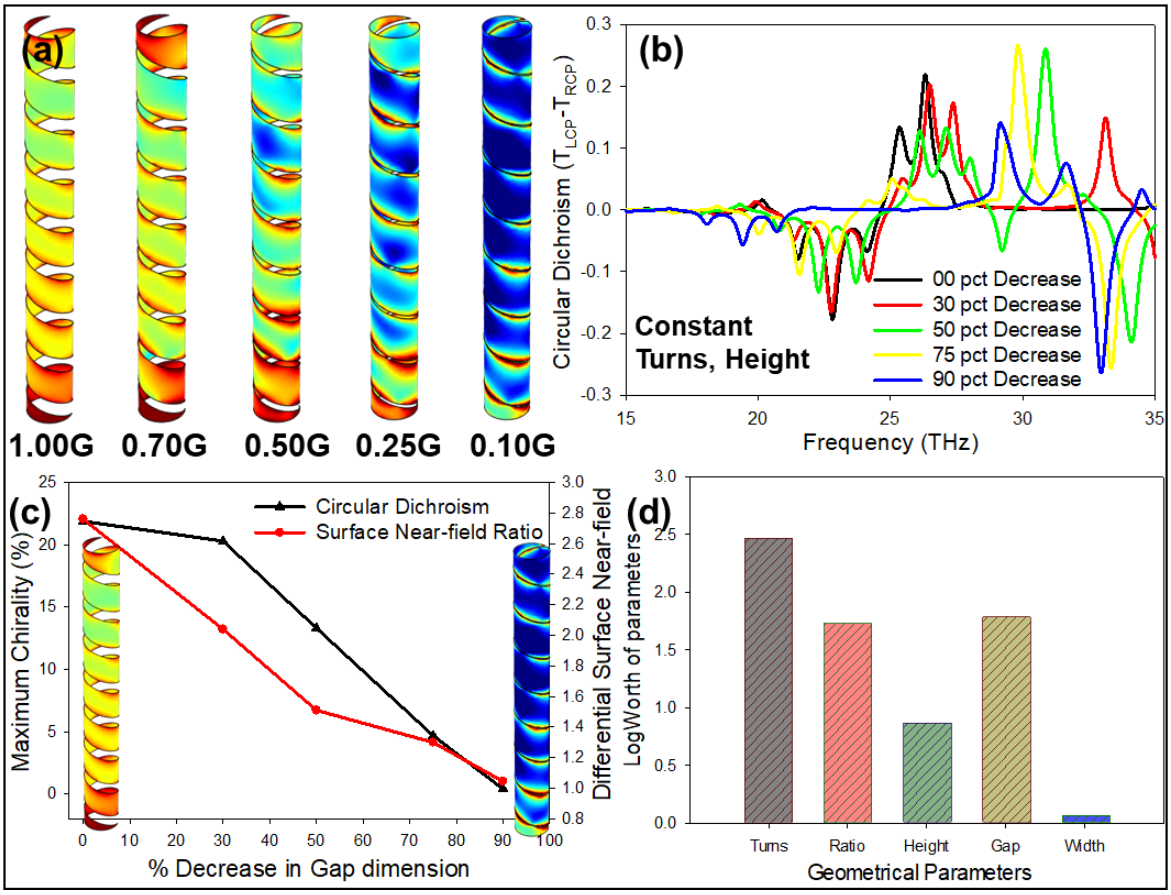

Figure 4.5 (a, b) Change in the surface near-field and optical activity with a decrease in gap length and a corresponding increase in width for a fixed length of helix and number of turns. (c) Graph showing the linear decrease in chirality

with a corresponding exponential decrease in the ratio of the surface near-fields for a decreasing width of gap within the graphene helical tubes. (d) Graph of the multivariable regression analysis showing the impact strength of the various geometrical parameters on the chirality.

The edge-based achiral cross-couplings have been shown to mediate the optical activity to a large extent. This cross-coupling is directly controlled by the gap length or rather the ratio of the gap to width in the ribbons. The surface-fields for RCP polarization switch to edge-fields when the cross-coupling increases at shorter gap dimensions (Figure 4.5a). For a decrease in the gap greater than 30% a sharp decrease in chirality is seen (Figure 4.5 b, c), which explains the previous saturation in chirality increase seen for structures on increasing in length beyond 1.25H in Figure 4.4a. It should be noted here that modes beyond 27THz need to be ignored as they are higher order modes and proportionally higher order modes occur for all gap lengths. It is interesting to note that the linear decrease in optical activity with increasing gap length is accompanied by an exponential decrease in the ratio of the surface fields obtained for RCP and LCP polarizations.

These simulations have shown that there exists a complex relationship between the geometrical parameters that comprise the helical structures due to

the addition of factors that mediate plasmon propagation and coupling. A technique that has emerged as a useful tool to analyze experimental parameters with a complex relationship is through the use of multivariate regression [177]. While this technique has been well-established in the medical industry for statistical analysis of clinical trial outcomes, it has seen a recent renewal of interest for other areas such as computational physics and material science to inform high efficiency devices with minimal experimental verification costs [178-180]. The multivariate regression can be concluded to be on the simplest machine learning techniques, falling under 'Supervised Learning Algorithms' to achieve faster results without the need for complex algorithms as is often the case in nano-optical structures. Using the statistical analysis software JMP Pro 14, the regression analysis was conducted with a multivariate fit model created using "Least Squares" for the resulting chirality to study the "effects" of the geometrical parameters within the helix. The model finds the log worth of each of the "effects" parameters on the desired variable (chirality). For the sake of simplicity based on the theoretical and precise nature of the datasets, the p-value can be assumed to be similar to the statistical "effect size". However, due to the extremely small p-values being hard to coherent, a parameter often preferred is the LogWorth, which is computed as -log10(p-value). The model fit reports the effect summary with LogWorth values

corresponding to each geometrical parameter such that a qualitative prediction can be performed on the “effects” and degree of “effect” of each parameter where higher the LogWorth stronger is the “effect”. The results (Figure 4.5d) show that the number of turns impact the chirality to the largest extent, followed by the gap of the structure, which is also close to the effect of the gap to width ratio. The actual length of the structures and width of the ribbons, which have the highest effect in conventional plasmonics do not show a proportionally strong effect in chiral plasmonics. Thus, for the highest degree of chirality tubular graphene structures with a high turn density (pitch) and large gap dimension are required such that a maximum chirality of nearly 40% is seen for the presently simulated structures and can be increased further as informed by the regression model.

4.4 Optical activity in vertically aligned cubic graphene helixes

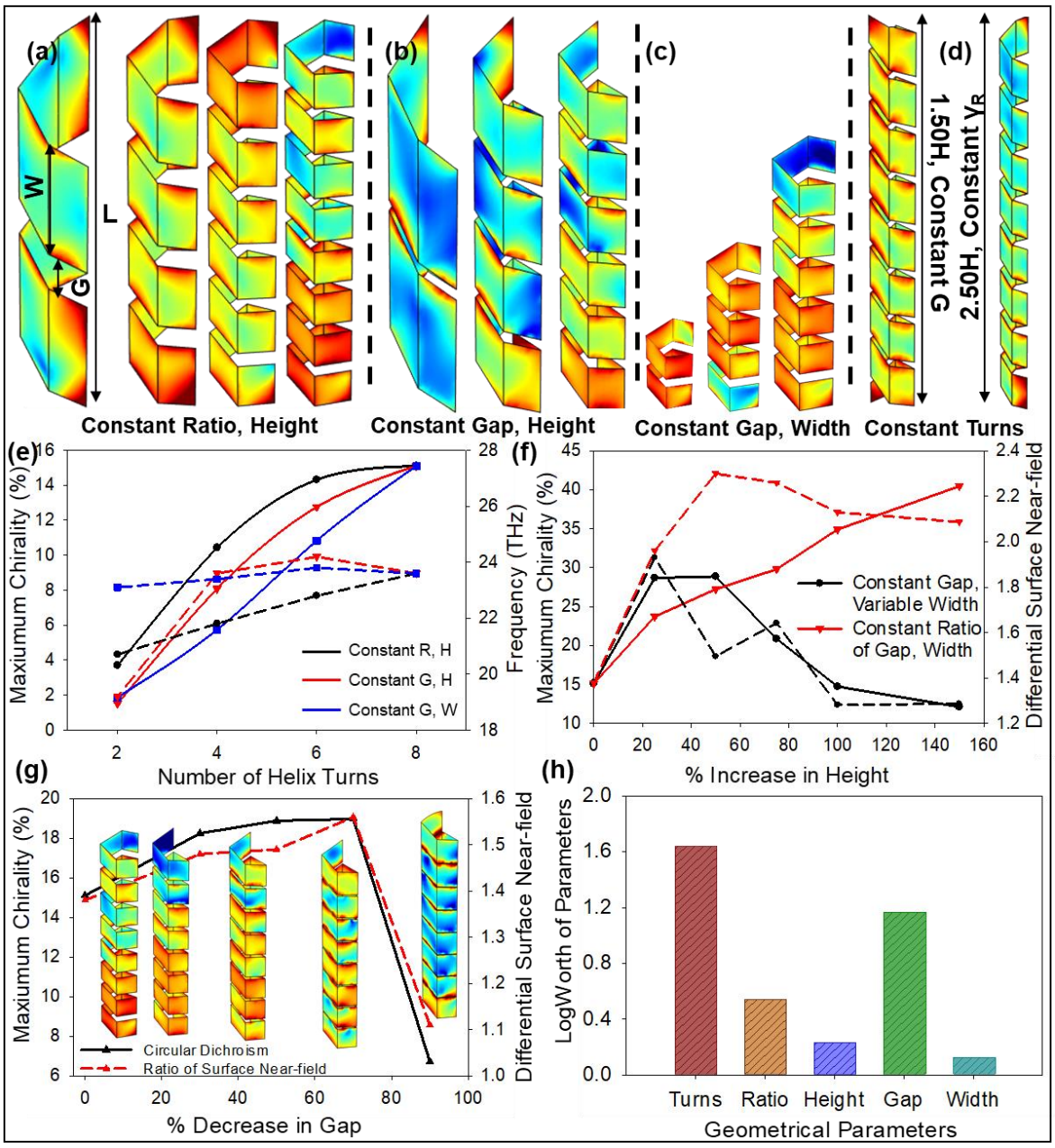

Figure 4.6 (a-d) Near-field enhancement plotted on the surface of the 3D cubic graphene helixes for varying turns and height while maintaining some other parameters constant. (e) The maximum chirality and the corresponding

resonant frequency for the cubic helixes with varying number of turns (f) The effect on chirality and the ratio of surface fields for RCP and LCP when the length of the structures is increased from 1.0H to 2.50H as shown in d. (g) Maximum chirality and ratio of the surface electric field between RCP and LCP polarizations for decreasing gap dimensions. (h) Graph showing the model fit obtained for the log worth of various geometrical parameters that affect the chirality.

The previous section demonstrated that helical graphene structures form an excellent basis for achieving mid-IR plasmonic chiral response; however, it was shown the high susceptibility of these structures to the plasmonic gap dynamics and the complex relationships driven by the curvature, which causes geometrical equations to be non-linear. Thus, it is necessary to examine other forms of helical structure to decrease the complexity while maintaining a high degree to chirality. In the previous chapter, elongated graphene cubic structures with a high dimensionality parameter were introduced, these structures delivered ultra-high surface fields. Since chirality in graphene is a surface phenomenon, integration of the high dimensionality cubic structures with chiral helixes can lead to an optimum platform for chiral plasmonics.

Similar to graphene helical tubes, the number of turns in the helical cubic structures can also be varied and be classified into three cases (1) Constant γ_R and L, (2) Constant G and L, and (3) Constant G and W (Figure 4.6 a-c). The resonant frequency in these structures is less affected by the turns and gap dynamics in these structures compared to cylindrical helixes. This is evidenced by the low resonant frequency change and the same chirality for two turn structures with high γ_R or small helix length (Figure 4.6e). The length of the cubic helixes also impacts the chirality induced in these structures (Figure 4.6d). However, unlike cylindrical structures there does not exist a saturation for the chirality on increasing the length of the helix. This phenomenon is again driven by the lower plasmon wavelength variance for the cubic helixes. Thus, achieving a chirality of ~41% for a length of 2.50H although with a lower ratio of the surface fields between the two polarizations at ~2.1 compared to ~3.8 for cylindrical helixes (Figure 4.6f). The sustenance of chirality over shorter gap lengths can also be evidenced when the gap is decreased such that the gap can be decreased by 75% without any decrease in chirality (Figure 4.6g). This is caused by the stronger surface fields in cubic helixes, which do not switch to the conventional edge fields until the gap is reduced beyond 75%.

Using multivariate regression, the LogWorth of the geometrical parameters comprising the cubic helixes show that for these structures the

effect of the number of turns within the cubic helixes far outweighs any other parameters. Moreover, due to the strong surface fields, the ratio of the gap and width of the ribbons does not significantly impact the chirality with a weak dependence on the gap within the helixes. Thus, the cubic helixes allow the realization of chiral plasmonic structures with lower complexity through the optimization of only a single statistically significant parameter.

4.5 Optical activity in vertically aligned pyramidal graphene helixes

A discussion of the 3D graphene structures, chirality, and helixes is incomplete without the incorporation of pyramidal helixes where asymmetry exists even in the direction of propagation. For the pyramidal helixes, the maximum chirality obtained is much lower than that for either tubular or cubic graphene helixes. This is caused primarily by the non-uniform length of the ribbons along the length of the helix, which causes losses in plasmon propagation through reduced inter-turn couplings as a result of different plasmon wavelengths as evidenced by the multiple resonant peaks in the

transmission response. When varying the number of turns of the helix while maintaining constant height of the structures, the gap and width can be simultaneously scaled for a constant γ_R (Figure 4.7a). However, in these pyramidal helixes, if the number of turns is varied for a constant gap and width of ribbons, then, along with the length of the helix, the diameter also scales proportionately (Figure 4.7b). In the former case the resonant frequency decreases due to increased ribbon widths, while in the latter case, the decrease in diameter causes the resonant frequency to increase (Figure 4.7c). Even with the increase in widths of the structures, there is no evidence of edge-based cross-couplings within these pyramidal helixes due to their inconsistent plasmon wavelengths. Thus, a slightly lower decay in chirality is seen for the first case when compared to the second which has an added decay from the reduced path length with number of turns. As we already know, that path length is one of the forward driving factors for stronger chirality. Similar to other helical structures, the path length in the pyramidal graphene helixes can be varied between 1.00H to 2.50H with a constant γ_R (Figure 4.7d). Due to the lower edge-couplings for both the cases an increase in chirality is seen for an increase in the length of the helix with no saturation of the chiral response (Figure 4.7e). The complex non-uniformity along the length of the helix and the low tunability range for the chirality across all the geometrical parameters

(maximum chirality of only 12% across everything) is reflected in the high LogWorth for all the geometrical parameter constituting the pyramidal helix structure (Figure 4.7f). It is interesting to note that while the diameter has shown to be one of the key effect parameters in conventional metallic helixes [181], for the complex plasmonic interactions in graphene helixes, they are not a statistically significant parameter.

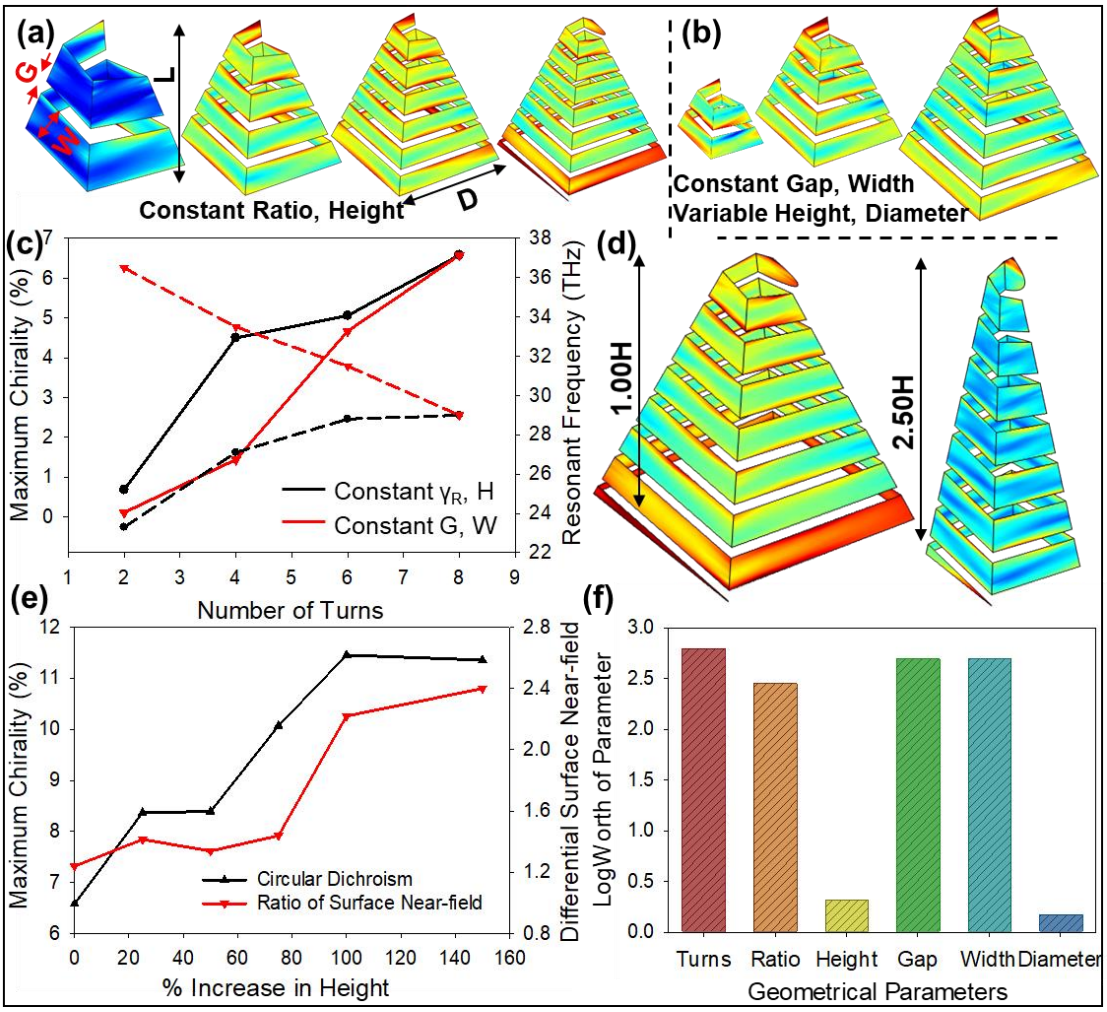

Figure 4.7 (a) Near-field enhancement plotted on the surface of pyramidal graphene helix of varying turns with a constant height such that the gap and

width are scaled equally to maintain a constant γ_R. (b) Near-field enhancement plotted on the surface of pyramidal graphene helix of varying turns with constant gap and width dimensions such that both the diameter and length of helix change. (c) Graph showing the change in chirality and resonant frequency for a varying number of turns in the pyramidal graphene helixes. (d) Near-field enhancement plotted on the surface of pyramidal graphene helix for varying length of helix such that the gap and width are scaled equally to maintain a constant γ_R. (e) Graph showing the change in chirality and the ratio of surface field for the two polarization when the length of the helix is varied by 150%. (f) Multivariate regression model showing the LogWorth of each geometrical parameter that constitutes its affect on the chirality.

4.6 Comparison of circular dichroism in 3D graphene structures

A comprehensive analysis of all the graphene structures in this chapter (Figure 4.8) reveals that the largest chirality is induced in the cubic helical structure owing to the high differential absorption that can be induced within

them for increasing length of helix without saturation, uniformity of ribbons forming it, and higher surface fields for a cubic structure, and low change in resonant frequency. This is followed closely by the chirality induced in tubular graphene helixes, then the pyramidal graphene helixes and lateral graphene helix. The tube and 2D ribbon structures do no demonstrate any chirality in their transmission response. However, in terms of selective near-field enhancement for a polarization, the tubular graphene helix outperforms all other structures. The horizontal cubic and pyramidal structures induce a differential near-field enhancement close to each other and then the lateral helix with a negligible differential field. It should be noted that the vertically aligned structures do not demonstrate a volumetric and total surface enhancement that is as strong as the ones in the lateral tube structures under the same right-handed circular polarization of the incident wave. The field around the spatial volume of a 2D ribbon also outperforms the 3D vertically aligned helix structure, however, as already shown in previous sections, the volumetric and surface fields can be rapidly tuned in 3D graphene geometries for a strong enhancement while retaining their circular dichroism. While the integrated field enhancements do not show a strong intensity out-of-the-box for the vertical helical structures, the point-based enhancement is the strongest in vertical tubular graphene helixes stemming from the tapering of the ribbons

at the two ends of the helix and the switching to edge-based conventional plasmonics.

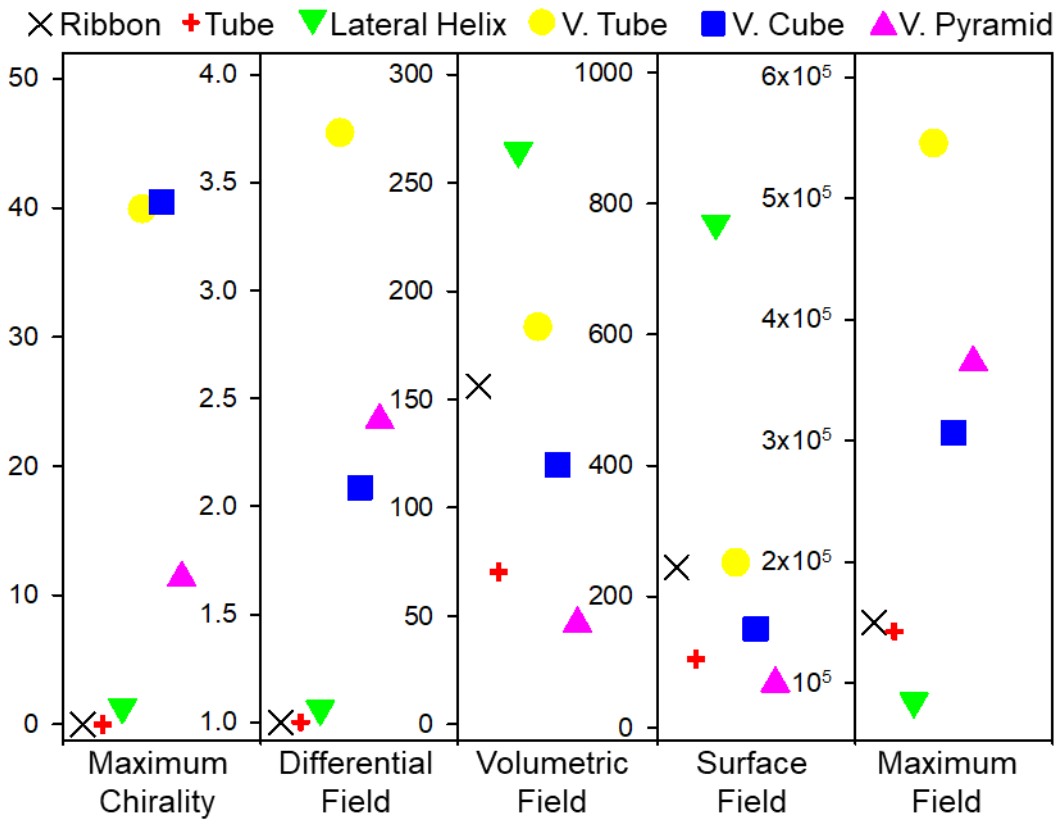

Figure 4.8 Graph comparing the maximum chirality percentage, differential surface fields, volumetric field enhancement, surface field enhancement, and the maximum enhancement intensity for 6 different types of graphene geometries namely, 2R ribbon, 3D tube, lateral helix, vertically aligned tubular helix, cubic helix, and pyramidal helix.

Chapter 5

Characterization of Plasmonics in 3D Graphene structures

5.1 Fabrication of 3D graphene structures

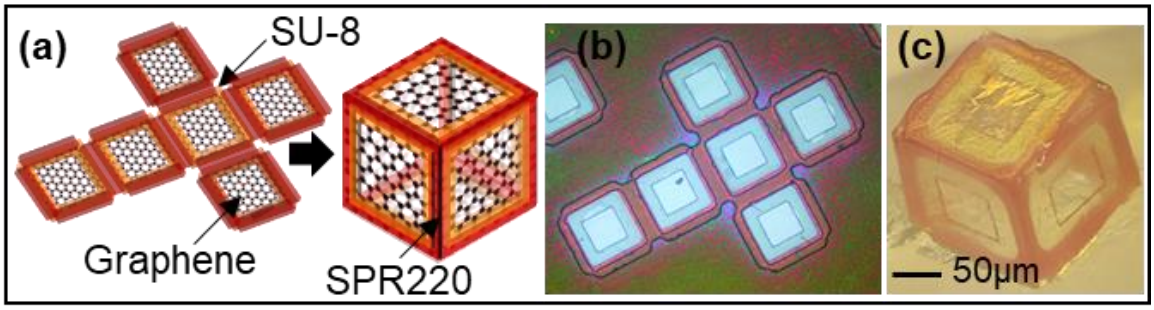

Figure 5.1 (a-c) Schematic illustrations and optical images of the 2D pattern and corresponding microscale 3D graphene cubic structure after self-folding [183].

As shown in Chapter 3, there exists a strong dependence of plasmonic fields on the dimension of the graphene structures, giving strong motivation for scalable fabrication at both micro and nanoscale. In this section, microscale structure is explained as a starting point due to its similarity in processes to that

used for realizing 3D SRR-based structures as detailed in chapter 2. The graphene oxide membranes in the previous section are replaced with multi-layer graphene followed by a self-folding process to result in microscale cubic graphene (Figure 5.1) [182]. Graphene plasmonic properties do not significantly appear at scales larger than a couple of microns. Thus, it is necessary to scale down the process covered in the previous section to a nanoscale. Even at the nanoscale, the 3D graphene nanoarchitectures can be realized by the origami-like self-assembly. Diverse 2D graphene patterns can be used to achieve three distinct types of hollow 3D graphene architectures, namely, 5-faced square pyramids (Figure 5.2a-d), 5- or 6-faced cubes (Figure 5.2e-h), and cylindrical tubes (Figure 5.2i-l) with heat energy supplied from hot plates, focused ion beams, and exothermic reactive ion etching [183].

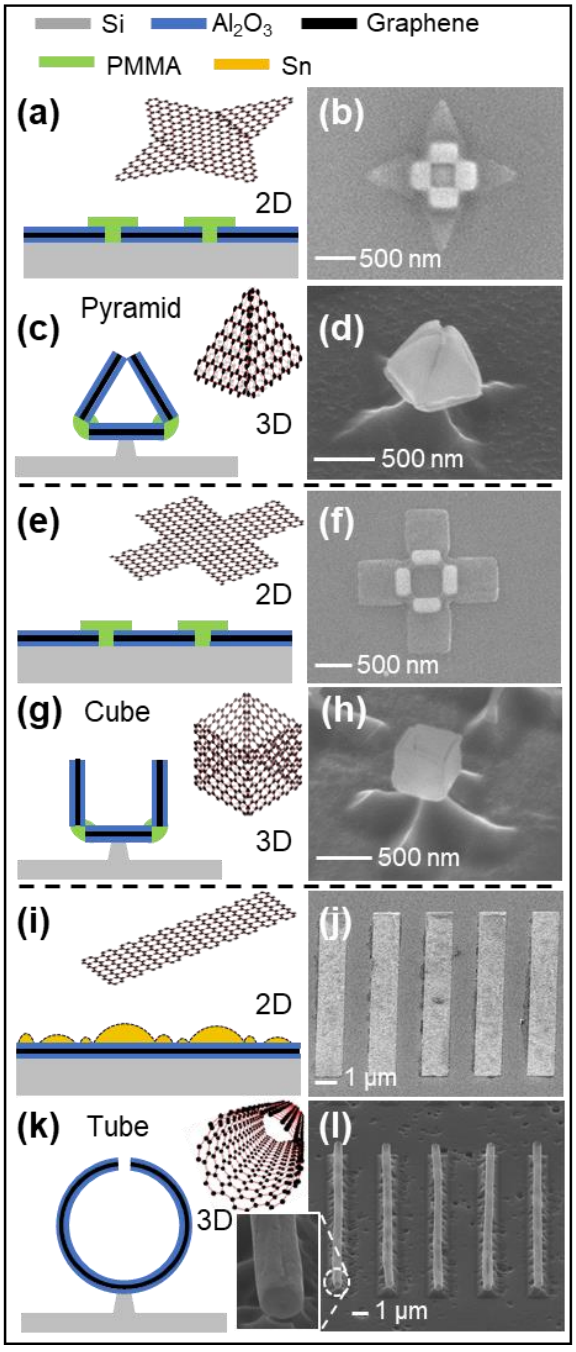

Figure 5.2 Schematic illustrations and SEM images for the 3D graphene architectures before and after self-assembly. (a–d) 2D pattern that folds into a 5-faced square 3D pyramid with graphene sandwiched between two protection layers of alumina and PMMA hinges. The heat required to melt the PMMA

polymer hinge was applied through a hot plate. (e-h) 2D pattern that folds into a 3D 5-faced graphene cube. The heat required for assembly was applied through a gallium ion beam that was focused only on the PMMA hinges to prevent damage to graphene. (i-l) 2D rectangular graphene ribbon that is folded to form a completely closed tube structure. The heat required for assembly was applied through exothermic plasma etching. The tin (Sn) hinge was etched after assembly of the self-supporting tube structure [183].

A similar self-assembly process has been developed that can realize 3D graphene helical structures from 2D patterns. The self-assembly process is carried out through in-situ monitoring in a scanning electron microscopy system, where the electron beam induces a crystallization in the thin alumina layers triggering the curvature of the structures through a differential stress in the alumina-chromium bi-layer system that has graphene patterned between them (Figure 5.3 a-c). If the structures are only anchored at one end and the anchor is also exposed to the electron beam, first the curvature of the strips occurs followed by the vertical alignment (Figure 5.3 d-f). [Adapted with permission from developer and collaborator Chunhui Dai]

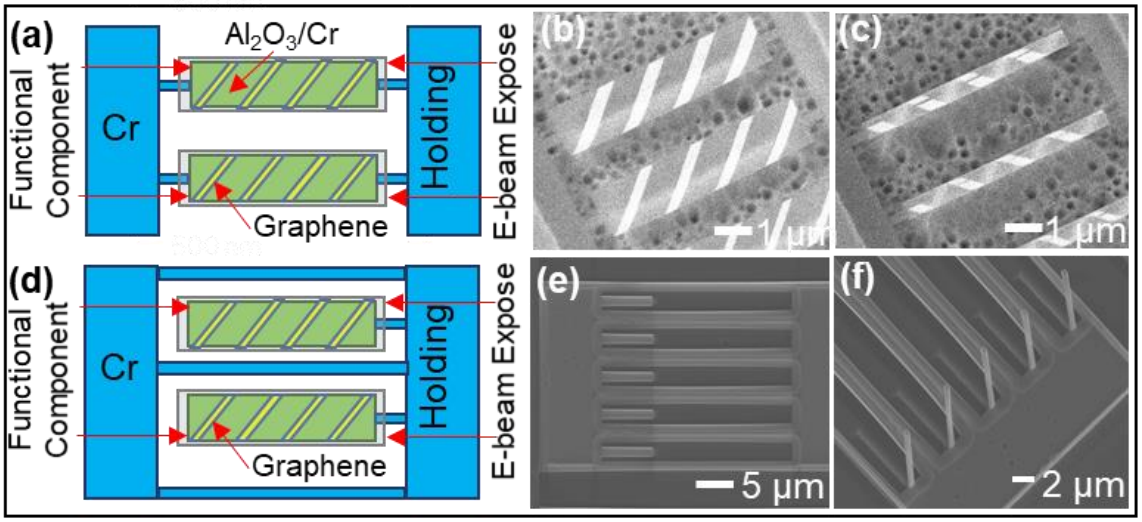

Figure 5.3 Schematic illustration and SEM images for the fabrication of 3D graphene lateral and vertical chiral helix structures. (a-c) Two different lateral helix structures realized using the e-beam triggered crystallization process. (d-f) Vertically aligned graphene tubes realized through the same process through a change in holding anchor design and exposure area. [Adapted with permission from Chunhui Dai].

5.2 Properties of the realized self-assembled 3D graphene structures

The effect of added dimensionality and the fabrication process can be divided into a few categories namely, the effect on intrinsic graphene chemical structure due to dimensionality, the effect on graphene optical properties due to dimensionality, and the effect of additional materials used in self-assembly.

5.2.1 Raman spectroscopy of 3D graphene

Before and after self-assembly, material properties of the 3D graphene-based structures were characterized using Raman spectra to investigate the effect of the self-assembly that might have on the graphene's chemical structure. For the nanoscale samples, the Raman spectra were captured after self-assembly with the results as shown in Figure 5.4a. The mapped images of the G-band peaks in the Raman spectra (Figure 5.4b-g) underwent the same transformations in shape as the actual sample between the respective 2D patterned graphene and 3D graphene architectures, thus, demonstrating that intrinsic graphene properties are preserved in the self-assembled 3D nanoarchitectures.

As a deeper study, the chemical structure changes in 3D tubes were investigated based on the Raman spectra and the resulting effect on optical properties. In the 3D partially and completely curved tubes, the defects could be attributed to the increased density of edge defects and lattice disorder caused by stress or wrinkles induced during self-assembly. After self-curving, the edges of the ribbons curve towards the middle of the tube and cause a higher density of edge defects and lattice structural stress, leading to a higher D band. To further quantify the defect level, the ratio of the D band intensity (I_D) and G band intensity (I_G), I_D/I_G, is calculated, which is around 1 (representing low defect regime [184]) for completely curved graphene nanotubes.

The change or any deterioration in graphene properties as a result of self-curving was also simulated to find the change in the resulting near-field enhancement. The higher I_D/I_G ratio in halfway (0.357) and completely (1.063) curved nanocylinder as compared to pristine graphene (0.058) can be attributed to two factors, firstly, the strain induced in graphene as a result of the curvature, and secondly, due to edge defects induced after self-curving. However, it is difficult to estimate the percentage contribution of both these factors; nevertheless, it is important to note that this level of defect ratio is still considered to the in the low defect regime that extends to all Raman peak ratios below 3.0.

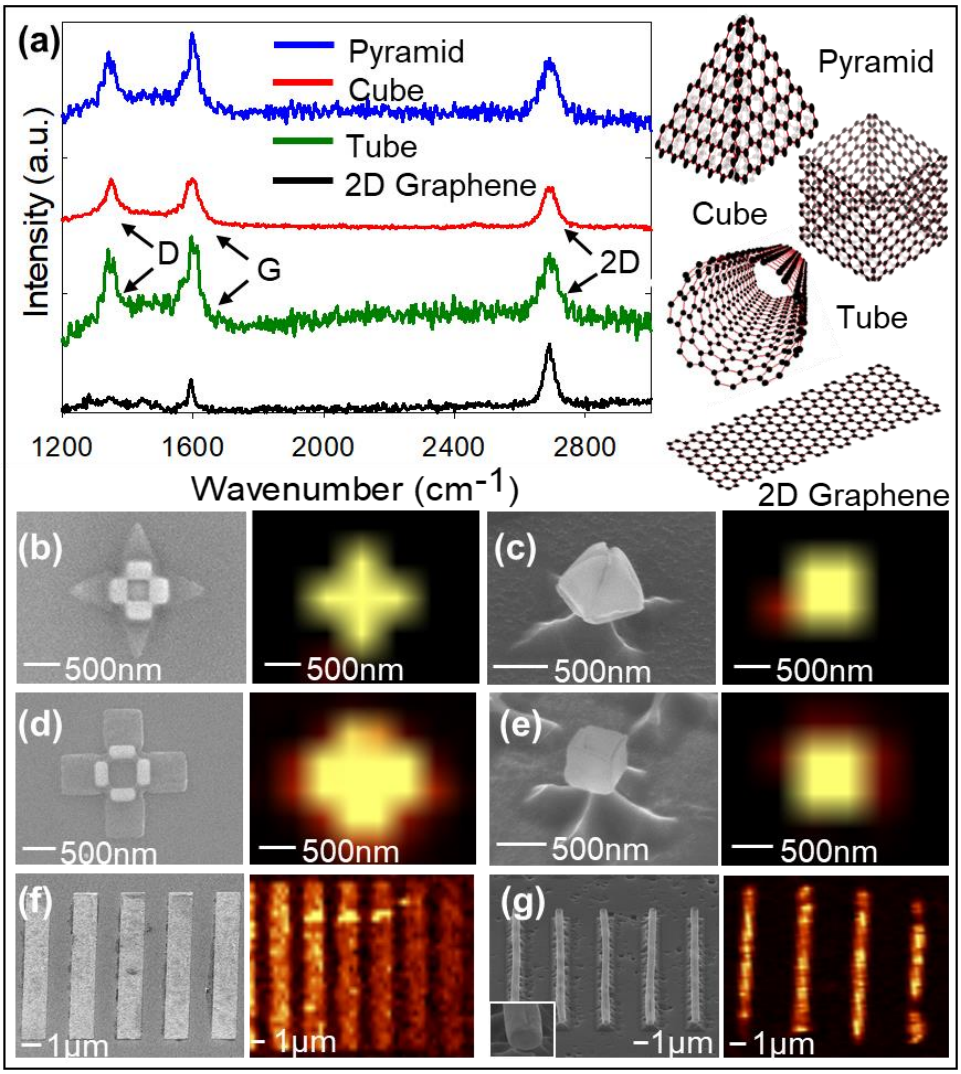

Figure 5.4 Raman spectra and mapped G-band images for various 3D geometries and 2D graphene. (a) The spectra demonstrates 3 peaks corresponding to D band, G band, and 2D band. The sharp G and 2D bank peaks demonstrate the preservation of the intrinsic graphene properties. (b-g) The mapped G-band peaks for the graphene before and after self-assembly show the same transformation in as in the geometry of the structure. [183]

Here, we account for the worst-case scenarios for the high I_D/I_G ratio in the 3D curved nanocylinders. The defect concentration (n_D) in graphene can be related to the Raman peak ratios using the relation below.

$$n_D\,(cm^{-2}) = \frac{(1.8 \pm 0.5) \times 10^{22}}{\lambda_L^4}\left(\frac{I_D}{I_G}\right)$$

where, λ_L is the wavelength of Raman light source and I_D and I_G are the intensities of the D and G band peaks, respectively. The defect concentration is inversely proportional to the relaxation time; thus, all other factors remaining constant (including Fermi velocity and Fermi energy), this gives a 5.45% decrease in the relaxation time for the curved cylinders. However, the relaxation time and Fermi energy do not remain constant in strained graphene. For graphene with a 10% strain, the Fermi velocity decreases by 15% [185]. The strain in graphene can open a bandgap and increase the bandgap in doped samples with some works even reporting an increase in the work function of 0.6 eV, however, there isn't a consensus on the percentage increase in the bandgap with strain [186]. It is well-known that the relaxation time (τ) in graphene can be calculated by the equation given below [187, 188].

$$\tau = \frac{\mu\,\hbar\,\sqrt{n\pi}}{e\,v_F}$$

where μ is the electron mobility (2700 cm^2/V-s), $\hbar$ is the Planck's constant n is the electron density (required for a bandgap of 0.4 eV chosen in our

simulations), e is the charge on an electron, and v_F is the Fermi velocity (typically 1×10^6 m/s). Using these values, we obtain the relaxation time for our 2D graphene ribbons to be equal to 0.101 ps (as opposed to 0.35 ps chosen previously). With the 15% increase in Fermi velocity for strained graphene, the relaxation time increases to 0.118 ps. Now, if we attribute the majority of the D band to defects introduced in graphene and not lattice stress, then the relaxation time for the curved nanocylinders turns out to be 0.015 ps. Simulations with a highly dense mesh compare the effect of relaxation time on the near-field enhancement in the 2D ribbon and 3D cylinders (Figure 5.5). The results show that the spectral width for the plasmon peaks in the ribbon and cylinder is nearly 11.71 and 10.69 THz, respectively. Moreover, even with the reduced relaxation time and in the absence of a conducting silicon substrate, the 3D cylinders demonstrate a volumetric enhancement that is 4 times stronger than the volumetric enhancement obtained for ribbons (assuming a thickness over the ribbon to make the volume equal to the volume within cylinders).

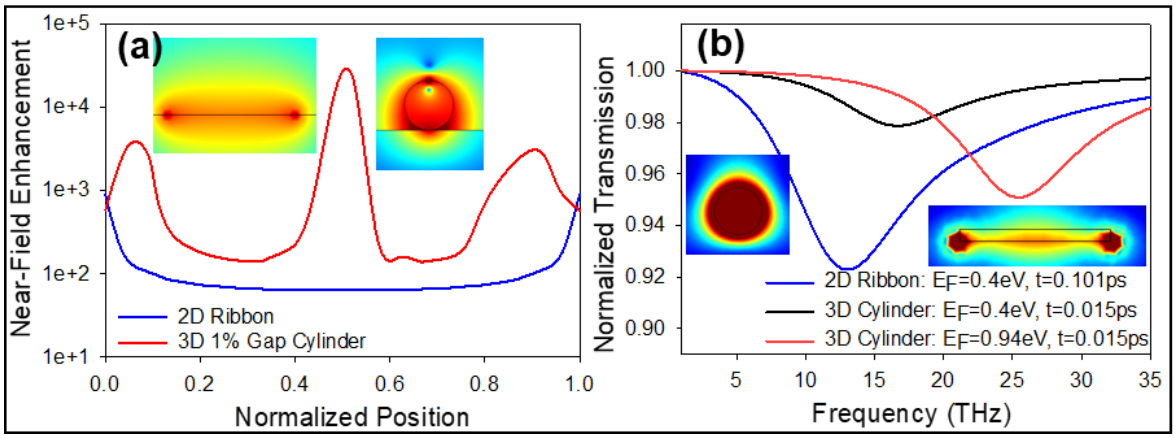

Figure 5.5 (a) Near-field enhancement plotted along the width of the ribbon and the circumference of the 3D cylinders with 1% gap under 2D simulations with a dense mesh to reduce any noise and fluctuations. (b) Transmission response showing the effect of change in relaxation time and Fermi level on the plasmon resonance caused due to curving of the 2D graphene into 3D completely curved cylinders. The insets show the corresponding near-field enhancements.

5.2.2 Effect of self-assembly materials on 3D graphene optical properties

5.2.2.1 Effect of hinge material

For the five-faced graphene cube without hinges, when the incident E-field is polarized along the bottom surface of the cube, a hotspot area of high

field enhancement is created on the bottom face of the cube due to the uniform field interference from all four adjoining graphene faces (Figure 5.5a). On the other hand, when metallic hinges are used to build 3D graphene-based nanostructures, the coupling induced between the graphene plasmons and the conducting metallic hinges causes losses in the plasmonic behavior of graphene (Figure 5.5b). For 100 nm thick metallic aluminum (Al) hinges, the size (500 nm × 500 nm) of the large hotspot is reduced in area (300 nm × 300 nm), extending to only those regions not covered by the metallic hinges (Figure 5.5b), as well as reduced in intensity by a factor of 3 (from 300, blue line, down to 100, black line, for a 500 nm length cube, Figure 5.5d). Thus, the bottom hotspot surface of the graphene cube with an overall near-field enhancement of 263 in the absence of hinges is reduced to 34 when metal hinges are present (Figure 5.5d). In contrast, when the nanocubes are realized using polymer hinges instead of metallic ones, the simulated results reveal the bottom surface of the cube retains the uniform circular hotspot of large near-field enhancement like the hotspot generated in the cube without hinges (Figure 5.6c). The hotspot surface on the bottom face of the polymer-hinged cube demonstrates a nearly uniform enhancement of ~311 (Figure 5.6d) with a minor increase as compared to a cube with no hinges (Figure 5.6d), which can be attributed to using the same mesh element size in the finite element modeling of hinges with

different refractive index (air space = 1, PMMA = 1.5) that modifies the wavelength of the incident light in the PMMA medium. The strong fields existing on the surfaces of the graphene create a strong volumetric field within the bound volume of the cube (Figure 5.6e), allowing it to be used as a smart container for increased sensitivity. In the presence of metal hinges, the lack of a hotspot reduces the field at the surfaces of the graphene cube and consequently the volumetric field is scattered from the surfaces of the cube (Figure 5.6e). However, in the presence of polymer hinges, a strong volumetric field is seen that decays when approaching the unbound surface (top face) of the cube.

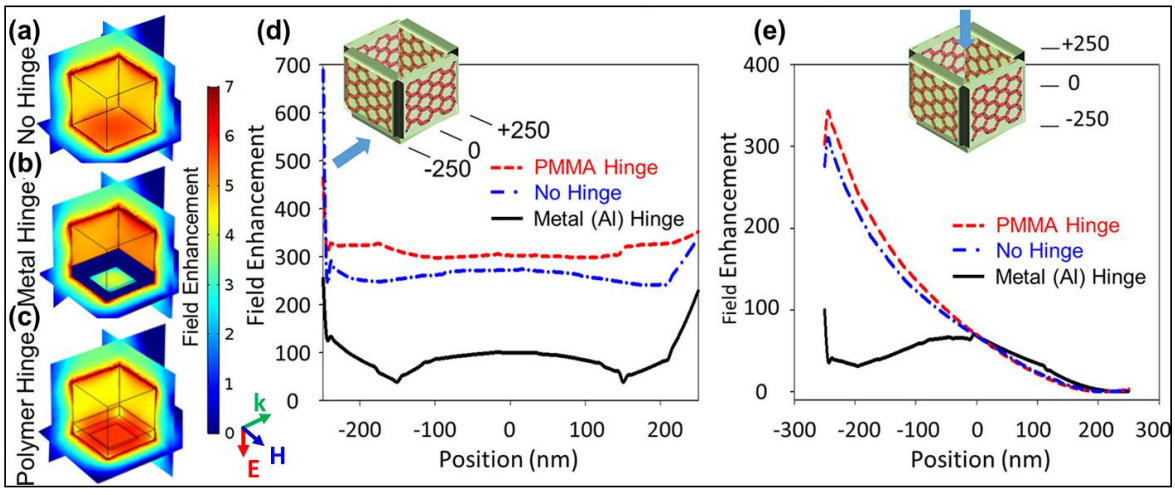

Figure 5.6 Analysis of the field enhancement in 3D graphene cubes with no hinges, metal (Al) hinges, and polymer (PMMA) hinges when the incident E-field is polarized toward the bottom surface of the cube with uniform coupling in all directions. (a-c) Simulated field enhancement (log scale) on the surface

of the cubic graphene containers with (a) no hinges, (b) metal hinges, and (c) polymer hinges. (d, e) Variations in the volumetric and surface enhanced fields for the cubic structures when (d) plotted along the bottom surface and (e) plotted at the center of the cubes along the direction of the incident E-field, as indicated by the arrow. [189]

In addition, the graphene container with polymer hinges experienced a minute shift in resonant frequency as opposed to large shifts experience by structures with metal hinges. The smaller shift in frequency is a major advantage for molecular sensing applications since the operating resonant frequency of the graphene containers needs to be controlled based on the vibration frequency of the targeted molecules and should be minimally affected by components constituting the plasmonic nanosensors. For a polymer hinge cube, the only factor affecting the resonant frequency is the size of the cube, thus requiring only one parameter for the design of plasmonic nanosensors with desired operating frequency. Thus, significant design convenience and accuracy are achieved compared to metal-hinged cubes where the combined effect of the cube size and hinge overlap and morphology need to be analyzed [189]. For these reasons, the 3D graphene tube structures have the Sn etched after completing the curving process. The Raman images proved

the continuous shape that is similar to the nanotubes after Sn etching. Even though the I_D/I_G ratio is slightly increased to 1.2, it still remains in the low defect regime. Both these two characterization results confirm the high optical properties of graphene after Sn removal process.

5.2.2.2 Effect of Alumina protection layer

The high surface quality of the Al_2O_3 layers is critical to the plasmons induced in graphene. Previous results show that when a dielectric material such as some spin-coated polymers or e-beam evaporated aluminum oxide are in contact with 2D and 3D graphene they seek to shift the resonant frequency proportional to the refractive index but do not significantly alter the near-field enhancement. It is important to note that the folding mechanism introduced here is not limited to CVD graphene or Al_2O_3 protection layers. Graphene tubes can also be fabricated using mechanically exfoliated graphene with hBN layers added between the current Al_2O_3-Graphene interfaces that have shown to also increase the relaxation to 3ps [190]. The aluminum oxide can also be completely replaced with other suitable materials such as SiO_2 or CaF_2. For the simulations, the dielectric layer is designed to be smooth; however, the impact of the roughness of Al_2O_3 roughness can be tremendous. Measurements of the

chemically (nitric acid) doped 200 nm graphene ribbons with and without the Al_2O_3 layers. Preliminary spectroscopy results (Figure 5.7) reveal that the quality and roughness of e-beam evaporated Al_2O_3 layers is low enough that it does not negatively impact the plasmon resonance of the graphene nanoribbons.

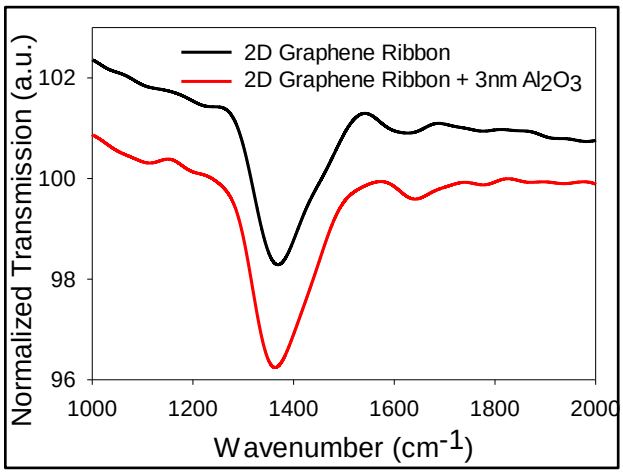

Figure 5.7 The measured transmission when a 3nm layer of e-beam evaporated Al_2O_3 is deposited on top of a 200nm width graphene nanoribbon.

5.2.3 Synchrotron infrared nano-spectroscopy for nanoscale 3D graphene

5.2.3.1 Advantages of 3D graphene measurement via Synchrotron-based nanospectroscopy

The characterization of the plasmon resonance induced within these structures is challenged by two major factors, namely, the targeted frequency range and the diffraction limit. The resonance of these 3D structures is targeted

to be within the far-IR range with a wavelength between 20-60 μm (5-15THz). This frequency range of the electromagnetic spectrum is particularly attractive to probe the low energy rotational modes within molecules, presenting an attractive application of graphene sensing [192]. But, the major challenge primarily arises from the lack of optical toolkits i.e. source, detectors, and materials that can support optical measurement systems within this frequency range. Quantum cascade lasers (QCLs) consisting of semiconductor heterostructures have made it possible to obtain commercialized mid-IR detection systems that operate at room temperatures [193]. Since the demonstration of the first QCL operating in the THz in 2001, material developments have led to achieving THz frequency generation from these devices, but the beams are extremely limited in terms of maximum power and often require cryogenic temperatures below 200K for operation [194]. Even with these advances, the Far-IR band of specific interest remains elusive due to the perfect overlap with the forbidden "Reststrahlen band" frequency range for semiconductors [195]. Within this frequency range, the vibrations within the semi-conductor crystals (phonons) give rise to a region of extremely high losses that cannot be overcome by QCLs; thus, necessitating the use of free electron lasers or synchrotron light sources where electrons are energized and accelerated to the speed of light by their movement through a magnetic field,

causing emissions in a path tangential to the curvature. The synchrotron light sources such as the one available at Advanced Light sources within Berkeley National Laboratory have a higher tunability range for wavelength and produce spectral brightness and coherence that far exceeds that of QCLs.

Even after overcoming the limitations of a source for the Far-IR beams, another obstacle is presented by the diffraction limit of the optics involved in conventional spectroscopy systems. These systems not only require a high filling factor of graphene (closely spaced arrays) but also place stringent requirements on the materials and quality of the underlying substrate. The three-fold reduction in surface area after self-assembly and the etching of the underlying substrate renders conventional spectroscopy-based measurement technique unusable for 3D graphene nanostructures. Therefore, the synchrotron infrared nano spectroscopy (SINS) technique is an ideal method to characterize the 3D graphene structures. The synchrotron produces an extremely high intensity and low wavelength IR beams that are required for the simultaneous excitation of plasmon across all surfaces of the 3D nanostructures to enable hybrid resonance modes. The beam is then coupled and confined to an AFM tip that launches the graphene plasmons as shown in Figure 5.8. The edge and area scans enabled by the AFM tip with a spatial resolution below 20 nm offer an attractive way to map and visualize the

plasmon couplings on the surface and reflections along the edges of the 3D graphene structures.

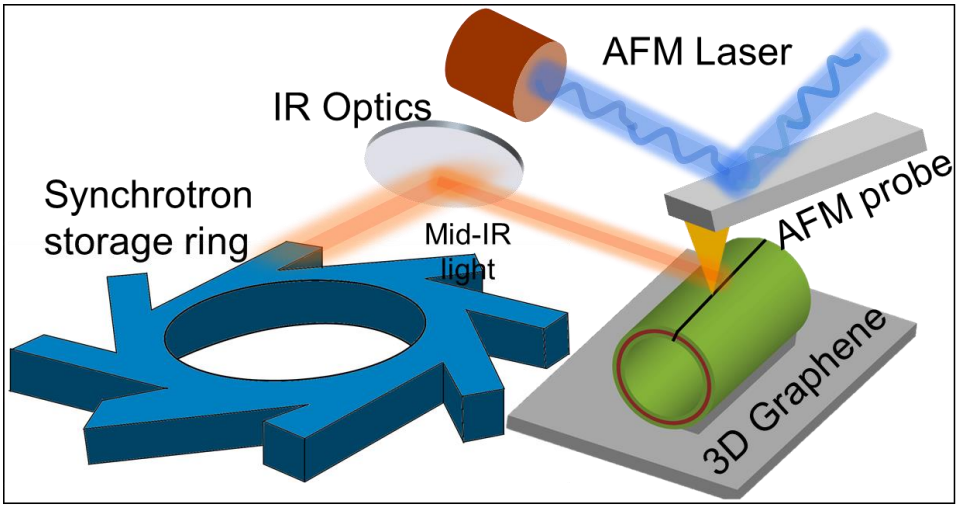

Figure 5.8 Schematic illustration of the measurement setup for SINS analysis of 3D graphene where IR radiation from a synchrotron beamline is used in an AFM nano-spectrometer.

5.2.3.2 Characterization of plasmon resonance in 3D graphene tubes

The high yield arrays of 3D graphene tubes, their simpler plasmon dynamics, easy to access morphology, and the similarity to 2D graphene ribbons make it an ideal choice for leading the SINS-based measurement of the plasmon resonance. The edge and area scans enabled by the AFM tip with

a spatial resolution below 20 nm offer an attractive way to map and visualize the plasmon couplings on the surface and reflections along the edges of the 3D graphene tubes. This technique allows line scans in AFM tapping mode along the top edge of the graphene tubes where it is expected that the plasmons are launched towards the edge and reflected by it. The interaction of the two small gap longitudinal edges within the curved graphene tubes will give rise to high-intensity edge-based near-field enhancement mode revealed by infrared nanoimaging functions within the SINS system. The 3D graphene tube samples were tilted at an angle of 45 degree to the surface and the incident light polarized along the width of the ribbon. The AFM Z-scan data shows the morphology (thickness) of the self-assembled graphene tubes (Figure 5.9a). The gap within the tube structures is below 15 nm as evident from the SEM images in Figure 5.2, however, due to the morphology of the tube structure and the tip-sample interaction, a larger gap of nearly 60-100 nm is perceived from the AFM data. The 3nm alumina layer used to support and protect the graphene is thin enough for the AFM tip to measure the absorption by the underlying graphene, which causes a deflection in the tip. The deflection image mapping is captured for a white light source integrated light nominally from approximately 330-1400 cm^{-1}. The images collected for different areas of the same sample show the strong edge-enhancements in the 3D graphene tubes

(Figure 5.9b). The rough surface of the silicon substrate adds to the noise level but the absorption on the 3D graphene remains clearly visible. The non-uniformity in the enhancement on the graphene tubes is primarily caused by the cracks and voids in the pristine graphene grown on the copper foil. The actual amplitude along 4 different positions as shown in Figure 5.9b was extracted using Gwyddion. The line profiles clearly demonstrate the high absorption amplitude on the graphene surface, which extends from about 0.1μm to 1.1μm in the graphed line profiles (Figure 5.9c). It should be noted here that the actual diameter of the graphene tubes is much smaller, but the tilt of the sample gives a higher perceived diameter. The perfect overlap of the actual AFM topography with the near-field absorption images prove that the graphene-based enhanced absorption that is observed is not an artifact or due to the underlying substrate (which is several 100nm away much farther than SINS vertical resolution).

The synchrotron light is a broadband source, thus, it cannot be exactly determined that the integrated absorption images correspond to exactly what frequency. To determine the exact frequency causing the strong absorption, spectra are collected using line scans over a few different positions on the tube structure. The second and third harmonic deflections of the cantilevers are considered to be optimum for measuring the near-field while maintaining a

high signal to noise ratio (SNR). The captured spectrum (Figure 5.10d) shows a clear increase in amplitude for the range of 600-700 cm^{-1} when measured on the tube surface. The spectrum also demonstrates the nearly flat and low absorption in this frequency regime when measured on the silicon surface that exists between the graphene tubes. Thus, the spectrum proves that the measured increased absorbance is due to the graphene and not an artifact.

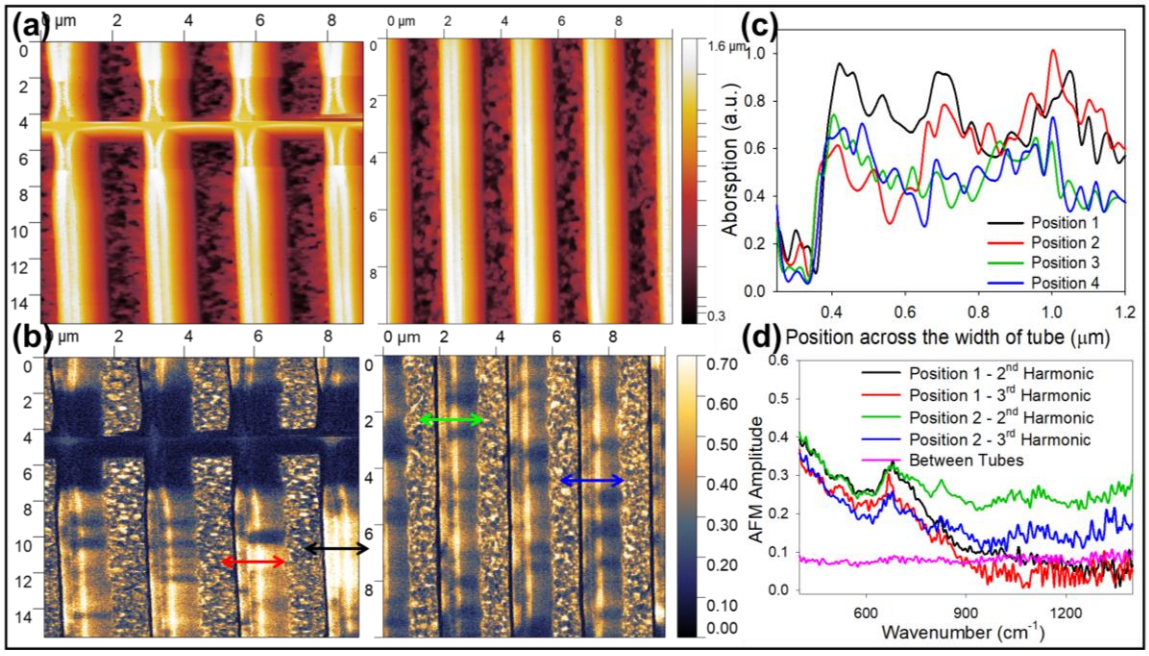

Figure 5.9 SINS data measured for the 3D graphene tubes. (a) AFM topography images showing the thickness of the tube samples. (b) AFM amplitude data corresponding to the near-field on the graphene and silicon surfaces. (c) Actual AFM amplitude data corresponding to the graphene absorption acquired for various positions as shown in b. (d) Second and third

harmonic linescan spectra for the graphene tubes captured for various positions on the sample.

A detailed analysis of the line scan image profiles reveals that there are sinusoidally varying absorption caused voltage maxima and minima on the graphene corresponding to the plasmon interference fringes. The width of these can consequently the plasmon wavelength can be measured by the distance between successive minima as shown in Figure 5.10a, where the plasmon wavelength is found to be 120 nm. The corresponding incident wavelength that induces plasmon resonance was found using third harmonic generation, which shows a clear peak at a wavenumber of 666.74 cm^{-1} i.e. a wavelength of 15 µm (Figure 5.10b). The incident wavelength information from the peak is further complemented by the change in phase slope also seen in the acquired spectra for the same wavenumber. This implies a confinement factor of 125 i.e. more than 2 orders of magnitude. The equivalent near-field power enhancement is then equal to four orders of magnitude in the 3D graphene tube structures. The result can be directly compared to the simulated data for the structures, which show a similar four order of magnitude near-field increase on the graphene tube (Figure 5.10c) for a resonant absorption peak at 530 cm^{-1} (Figure 5.10d). A slightly lower wavenumber for the simulated spectrum might be accounted

for by the difference in the chemically doped bandgap opened in measured graphene compared to the constant bandgap of 0.4 eV chosen for the simulated data. Similarly, the plasmon relaxation time was chosen to be 0.35 ps for the measurement whereas the doping and material stress in fabricated samples directly controls this value as discussed in section 5.2.1. It should be noted here that in the simulated samples a 5 orders of magnitude enhancement occurs at the center of the longitudinal split gap within the tubes (Figure 5.10c), however, as seen in the measured profiles (Figure 5.10a), a similar increase occurs at all three positions. This is a limitation of the AFM-IR process such that only absorption on a film can be measured and absorption inside the small gap cannot be probed the AFM tip morphology. Due to these limitations, currently the measurement of the volumetric enhancement in the 3D graphene cubic structures and pyramids and the cross-sectional enhancement in the 3D tube openings continues to be a challenge even with the advantages of the SINS technologies.

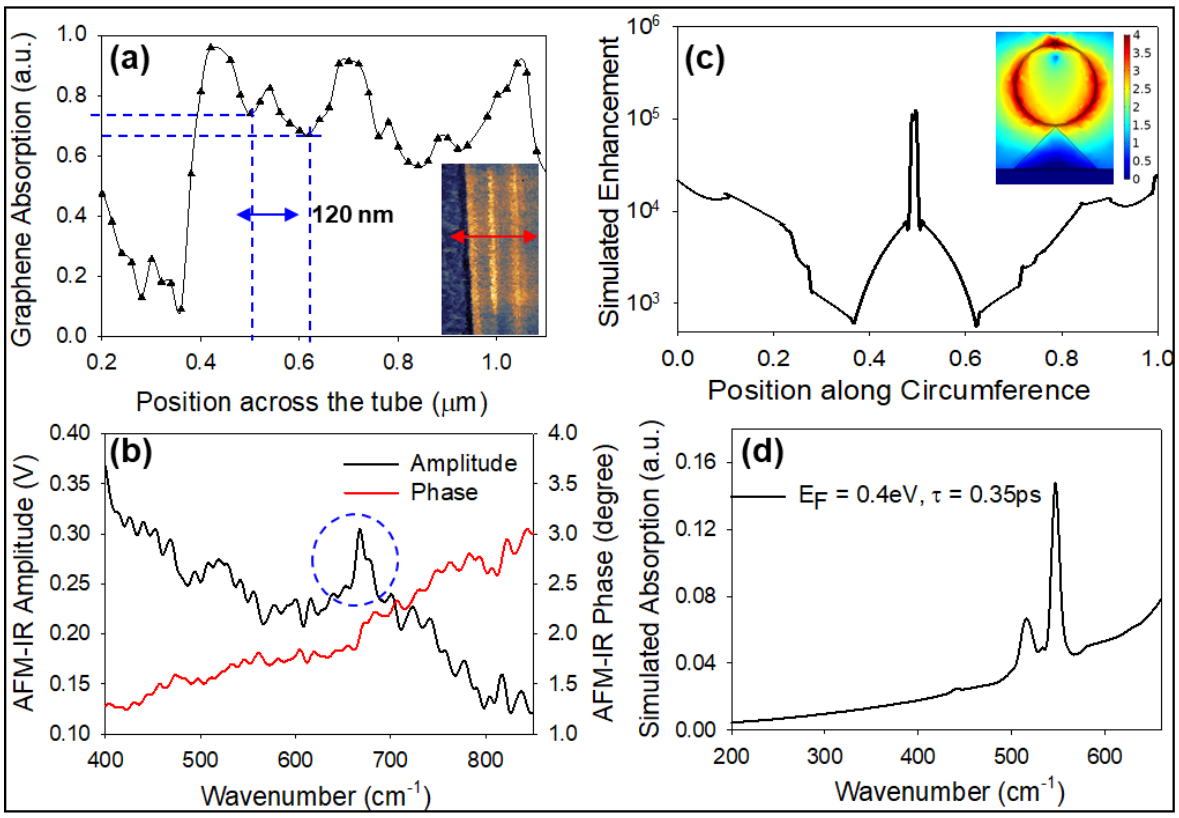

Figure 5.10 Comparison of the measured and simulated data for the 3D graphene tubes. (a) Graph showing the collected absorption data across the width as shown in the inset, the dashed lines mark the plasmon wavelength. (b) Third harmonic spectra captured for the 3D tubes showing the AFM amplitude and phase data. (c, d) Simulated near-field enhancement and resonance spectra for a 3D graphene tube with a bandgap (E_F) of 0.4 eV and a relaxation time (τ) of 0.35 ps. The inset in (c) shows a cross-sectional graphical image in log-scale for the near-field enhncement.

Chapter 6

Application of 3D Graphene for Optofluidic Sensing

6.1 Overview of architecture-based advantages for plasmonic sensors

3D nanoarchitectures extend and enhance conventional 2D graphene fields to deliver near-field enhancement modes that can be utilized for a wide range of applications through the selection of the 3D architecture and dimensions comprising it. The strong point-based confinement in cylindrical graphene and at the apex of pyramidal graphene can be utilized for the deposition of receptors needed to monitor target molecules of higher and known concentrations. The small diameter tubes offer a 2-fold advantage of utilizing the virtual cross-sectional area of uniform near-field enhancement for the detection of analytes as they flow within the graphene tubes without loss of target properties due to the need to attach targeted molecules on the surface of graphene. Furthermore, the strong near-field enhancement at the openings

of the nanotubes provides a stronger electric field gradient due to the reduced cross-section (diameter) as compared to the size of the corresponding ribbon. The high electric field gradients are particularly beneficial for enhancing dipole-forbidden transitions of quantum emitters for the analysis of several chemical species [196].

The 3D cubes and pyramids sacrifice the confined point and edge modes in favor of extremely large surface-area hotspots and volumetric enhancements. The intensified surface fields in 3D cubes stretching over an area that is an order of magnitude larger than 2D ribbons are especially attractive for studying adhesion and reaction properties of targeted molecules. The 3D coupled apex and base of the pyramid yield extreme volumetric enhancement, which can be leveraged for non-diffusion limited sensing at extremely small femto and atto molar concentrations of unknown targeted molecules. Two methods are possible to leverage the large surface and volumetric enhancements in 3D cubes and pyramids. First, even in 5-faced cubic graphene containers, a single large area hotspot can be induced due to one of the faces (bottom surface) experiencing uniform orthogonal coupling from all directions. Second, the targeted molecules can also be encapsulated within these 3D geometries by using biocompatible energy sources for generation of highly localized self-assembly triggers such as heating

prestressed hinges to 37 °C (optimum body temperature) or magnetic field-based assembly [171,198].

6.2 High concentration dielectric sensing in 3D graphene

For high sensitivity detection of biological analytes, the minimum detectable concentration is directly dependent on the changes in the frequency spectrum arising from changes in the electric field due to the dielectric properties of the targeted molecules. Hence, the near-field enhancement by graphene nanostructures is a key parameter in the development of higher sensitivity biological sensors. The presence of biological analytes introduces changes in the frequency spectrum of graphene by (i) shifting the LSPR frequency, and (ii) adding absorption peaks corresponding to the vibrational fingerprint of molecules. To analyze the performance of the 3D graphene nanoarchitectures as biological sensors, the shift in the LSPR frequency was simulated as a function of increasing relative permittivity of the molecules inside the nanocylinder, representing changes in concentration and presence of targeted analytes. Six structures were chosen to assess the sensing performance namely, the long-tube (α_t=4) (L. Tube), short-tube (α_t=4) (S. Tube), and (1%)

gap-tube (G. Tube)structures; elongated (α_c=4) (L. Cube), 4-faced (4 fc. Cube), and 6-faced cubic (6 fc. Cube), structures; and finally, square pyramids (α_p=1) (Sq. Pyramid), low dimensionality pyramids (α_p=0.5) (L. Pyramid), and octagonal pyramids (Oct. Pyramid) (Figure 6.1a-c). Each of the structures was simulated to be with a dimension of 100nm, a Fermi level of 0.4eV, and relaxation time of 0.35ps. The relative permittivity of the material filling the hollow cavity of the 3D graphene structures was varied from 1 to 8. The frequency spectrums were plotted for all six architectures for permittivity of 1 and 4 (Figure 6.1a-c). The resulting shifts in resonant frequency for all the structure is plotted in Figure 6.1d. As predicted, the highest shift in resonant frequency occurs for the octagonal pyramid structure owing to their highest volumetric enhancements. This is followed by that of the perfect square pyramid, which has the next highest volumetric enhancement. The worst sensing performance is seen in the short tubes and pyramids this is in part by their low shifts in resonant frequency but also accompanied by the large decrease in the absorption of the structure, which deteriorates the signal to noise ratio (SNR) for these structures (Figure 6.1e). The gapped tube structures offer an optimum compromise for these applications where a dielectric material of unknown permittivity completely fills the hollow cavity in 3D graphene structures. It should be noted that the slope of all 3D graphene

structures is maximum at permittivity of 1-2, which is the approximate range for all biological specimens.

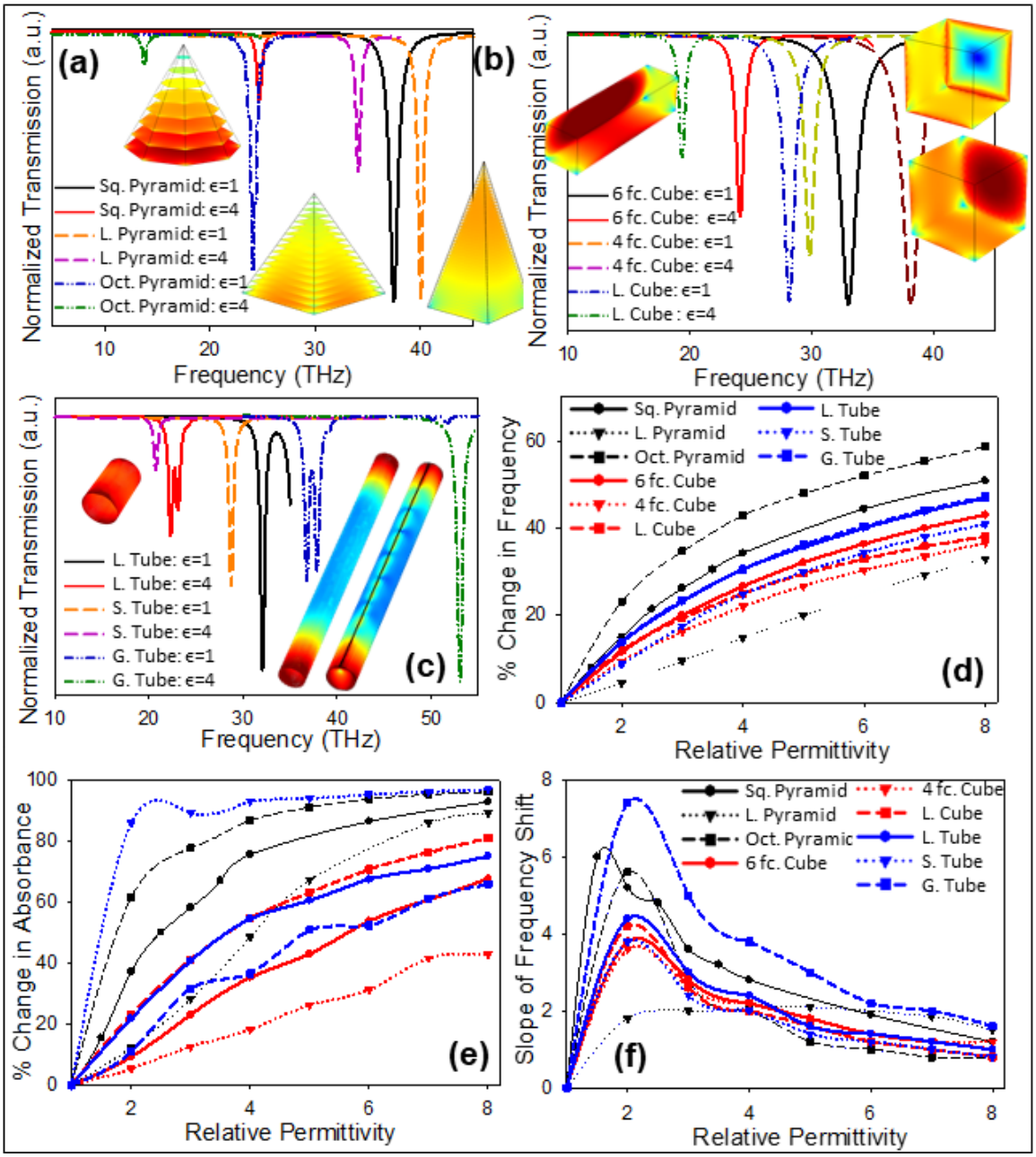

Figure 6.1 (a-c) Change in transmission response between a relative permittivity of 1 and 4 for diverse graphene tubes, cubes, and pyramids. (d)

Percentage change in resonant frequency for the various 3D graphene nanoarchitectures for increasing material permittivity inside the structures. (e) Percentage change in graphene absorbance for the various 3D graphene nanoarchitectures for increasing material permittivity inside the structures. (f) Point by point slope of frequency shift with the permittivity for 3D graphene.

6.3 Vibrational mode enhancement in 3D graphene structures

As covered in the previous section, one of the ways to apply the 3D graphene structures is through their use to enhance the vibrational modes that occur in proteins and DNA. The changes in the plasmon frequency spectrum as a result of the fingerprint of the amide I and II bands of protein A/G were simulated and analyzed to study the advantages of different 3D graphene nanoarchitectures for molecular fingerprint sensing. The small absorption of the electric field due to the large mismatch between the size of the protein particles and the wavelength of light corresponding to amide fingerprint frequency necessitates the enhancement of the incident electric field by

graphene plasmons to transduce measurable amide peaks in the frequency spectrum. The transmission response showing the overlap of the amide bands with the spectral bands of graphene is shown in Figure 6.2a-c. The evaluation for the response of cubic structure is relatively easy where we see that the strong surface field in the high dimensionality long cubic structure gives it the highest enhancement of the Amide bands for an equal amplitude (Figure 6.2b). When looking at the absolute amplitude this translates to a higher enhancement in the 6-faced cubic structures for the Amide-I band due to the higher relative absorption for 6-faced cubes among all the cubic structures (Figure 6.2d). However, the larger spectral bandwidth of the resonance in the long cubic structures is more desirable for the simultaneous detection of multiple bands as evidenced by the highest enhancement of the Amide-II band in these structures (Figure 6.2e). A similar analysis follows for the pyramid structures where even though the octagonal pyramid structures demonstrate a higher relative enhancement of the vibrational bands (Figure 6.2a), their actual absorption is low. This means that the maximum absorption for the Amide bands is induced by the square pyramid. It is interesting to note that even though the strongest actual absorption occurs for the elongated pyramid structures with low dimensionality, they offer the lowest enhancement of the Amide band absorption. The concept of relative absorptions is elucidated by

the graph shown in Figure 6.2f, where the heights of each section and the ratio between them reflect the actual and relative absorption values, respectively.

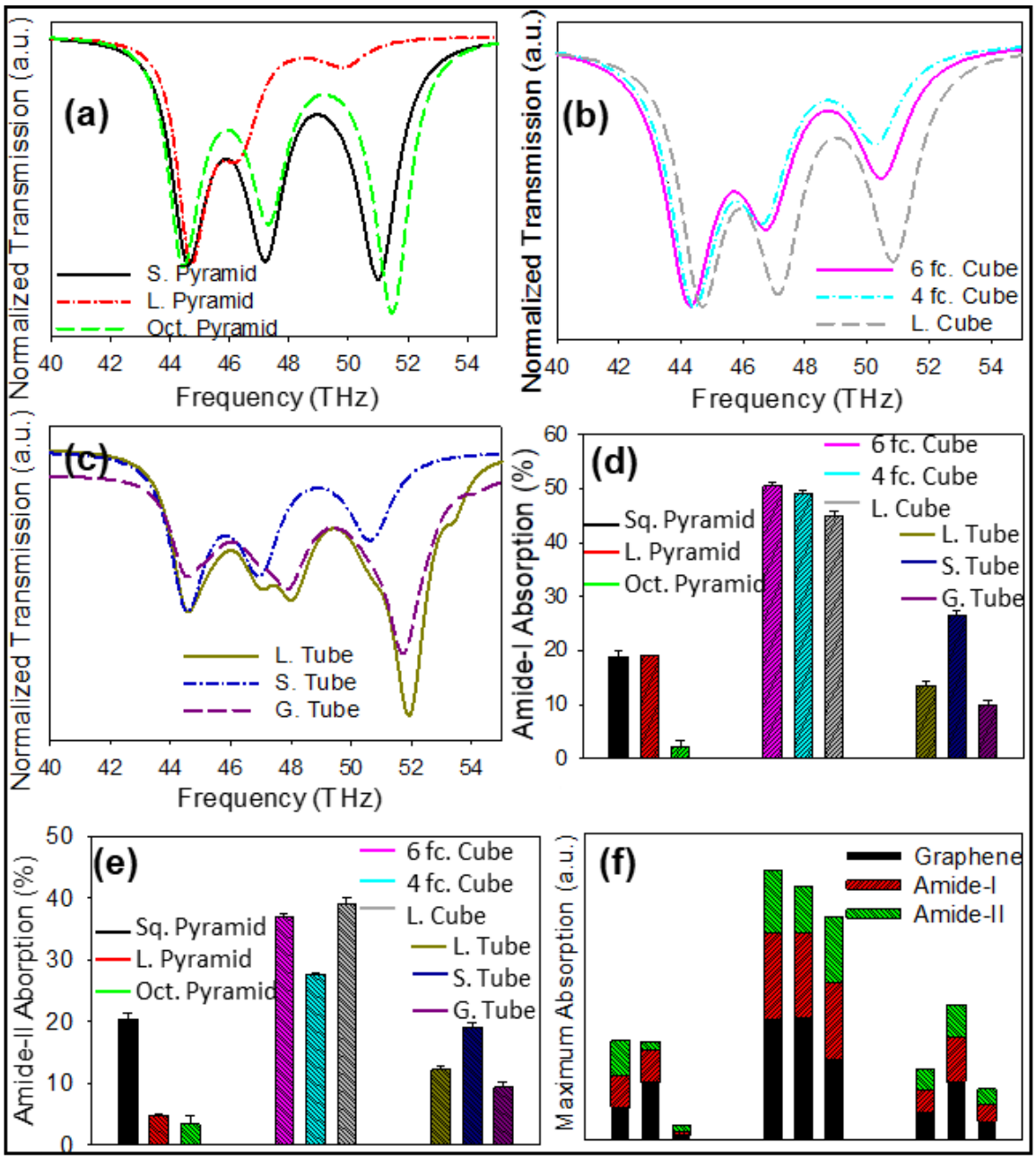

Figure 6.2 (a-c) Transmission response for diverse graphene tubes, cubes, and pyramids showing the three resonant peaks representing from low

frequency to high frequency, the graphene resonance, Amide-I band, and Amide-II bands. (d) Actual absorption in percentage for the Amide-I bands when the protein completely fills the hollow cavity of the 3D graphene geometries. (e) Actual absorption in percentage for the Amide-II bands when the protein completely fills the hollow cavity of the 3D graphene geometries. (f) Graph showing the absorption for the various 3D graphene structures and the enhanced Amide band absorption for protein filling their cavity. The height of each region of the bar graph represents the actual absorption.

This discussion becomes increasingly complex for the tube structures (Figure 6.2c), where the occurrence of quantized modes along the length of the tube at a higher frequency skews the results for long and gapped tube structures. However, it can be easily seen that the actual absorption induced in the Amide bands is strongest for the shorter tube structures (Figure 6.2d,e) where their actual absorption is also stronger stemming from the volumetric enhancement within them. It is important to note that this absorption of light by the shorter tube structure is not efficiently transferred to the amide enhancement by the lower ratio of the absorption between the graphene and amide bands as evidenced by their relative heights in Figure 6.2f. Looking at the bar graphs in Figure 6.2d-f, it is clear that cubic structures with their strong

surface fields offer the greatest advantage for enhancing the Amide-I and Amide-II bands spectra. Even within the cubic structures, the high dimensionality long cubic structures offer the best enhancement and an efficient transference of graphene absorption to a corresponding protein band absorption owing to their large area hotspots.

6.4 Low concentration sensing in 3D graphene

The primary reason that graphene biosensors are of wide interest is that small concentrations of targeted analyte below nanomolar concentrations can be detected with high sensitivity. To analyze the sensing ability of the 3D graphene structures to detect the permittivity of an unknown targeted material only available in nanomolar concentrations, simulations were conducted for a material of thickness (t) forming a uniform layer on the 3D graphene surfaces. Two characteristics define such sensors namely, their sensitivity and their figure of merit. Sensitivity is computed as the ratio of shift in resonant frequency to the corresponding increase in permittivity or refractive index. 3D graphene structures of 100 nm width with varying molecular layer thickness (t) from 2-50nm were simulated where the relative permittivity of the layer

was chosen to be 2.0 (close to that of most biological specimens) (Figure 6.3). The sensitivity in this case is then given by the percentage shift in resonant frequency with layer thickness. As shown in Figure 6.3a, the high volumetric enhancement of the pyramids allows them a larger overlap with the molecular layer, giving them the strongest shift in resonant frequencies. However, the surface enhancements are not particularly beneficial for sensing low concentrations. This is proven by the higher sensitivity for the edge-based modes in tubular structures. The pyramids also benefit from this higher edge-based enhancement whereas the cubic structures have the lowest edge enhancement as shown in section 3.5. It is interesting to note the switching in the second-highest shift between lower layer thickness for the tube and square pyramid structures.

The figure of merit (FOM) of sensors is important because it packages two parameters i.e. resonant frequency shift and the decrease in absorbance into one. FOM is defined as the ratio of sensitivity to the FWHM, as the absorbance decreases, the FWHM increases broadening the peaks and can cause the FOM, which is similar to SNR. To maintain a high FOM for reliable sensing, a proportional increase in sensitivity must occur. In chapter 1, one of the disadvantages discussed for 3D graphene formed with linear stacks was found to be the significant decrease in FOM even with increasing sensitivity.

However, for the self-assembled 3D graphene structures, it is evident that the superior sensitivity occurs alongside the higher FOM (Figure 6.3b).

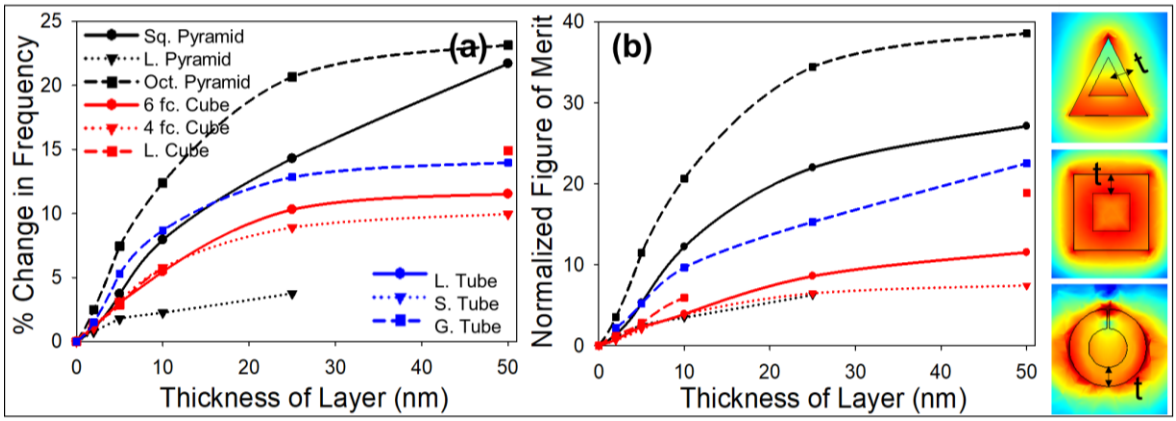

Figure 6.3 (a) Graph showing the percentage change in resonant frequency for increasing thickness of the molecular layer of relative permittivity 2.0 in contact with the diverse 3D graphene geometries. (b) Change in Normalized FOM that is computed by dividing the % change in 6.4a with the FWHM of the resonance.

For vibrational spectroscopy of single molecules that undergo absorption enhancement in the presence of graphene, the absorption is proportional to the field induced inside them that is also a function of their dielectric properties. Simulations were carried out for a single 2nm radium spherical particle with dielectric properties and amide band resonance modeled to mirror those in bovine serum albumin. Such a single particle within the 3D

graphene structures experiences the hollow cavity within which it is residing. To analyze the effects of the architecture of this cavity without effects from surface to mirror the non-surface diffusion sensing abilities, the simulations were carried out for the 2D cross-sections as shown in Figure 6.4a with varying distance from the surface (d) from 2 – 30nm. To overlap the graphene resonance at a 0.4eV Fermi level with that of the albumin amide bands, the 3D graphene cavity width was selected to be 60nm. In this case, the strongest volumetric enhancement gives the single particle, a much stronger enhancement over more than half of the cross-section of the cavity (Figure 6.4b). However, this increase exponentially decays whereas the uniform enhancements occurring in the cube and the short tube cavities are retained throughout the cross-section of the cavities.

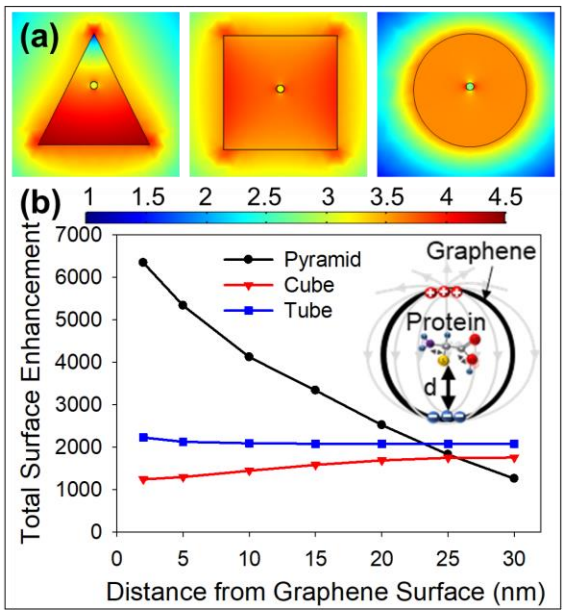

Figure 6.4 (a) Near-field enhancement within the 3D graphene cavities and on the surface of the single detected particle when the distance, d is 30 nm from surface. (b) Change in the enhancement on molecule surface with changing distance.

6.5 Tunability of sensing parameters in 3D graphene nanostructures

The previous sections have demonstrated that not just the near-field enhancement, but other parameters also control the efficiency of graphene-based plasmonic devices for biosensing applications. This section investigates the ability of the different 3D graphene structures to control, tune and enhance these parameters that affect the sensing capabilities. One of the first parameters that can be clearly analyzed when sensing dielectric materials of an unknown permittivity is the shift in the resonant frequency that is induced due to them. The minimum allowed detection level is controlled by the FWHM bandwidth of resonance. For a comparison between 3D graphene structures of different widths, this spectral width should be normalized with respect to the plasmon resonant frequency, this translates to the quality factor (Q-factor) of the plasmon resonance computed as the ratio of resonant frequency to the FWHM. The FWHM and consequently the Q-factor of resonance for graphene are most affected by the plasmon relaxation time in graphene usually in the picosecond (ps) range. To simulate the effect of the relaxation on the Q-factor in 3D graphene with the strongest shifts in section 6.2, simulations were conducted from 0.01 to 1.00 ps such that the graphene conductivity used in simulations

as given by the Kubo formula changes due to change in relaxation time. As clearly seen in Figure 6.5, the Q-factor increases with an increasing relaxation by nearly 2 orders of magnitude. The lowest initial Q-factor exists for the tube structures but is partially an artifact, which is caused by the superimposition of the spectra of their two modes at low relaxation times below 0.2ps. The results for the pyramid and cube structures shows that the degree of coupling in the 3D graphene structures controls the Q-factor and the range of Q-factor with relaxation time. This is evidenced by the stronger changes for Q-factor in the full 360degree coupling in the octagonal pyramids; meanwhile, the gapped tube structures reduce the scattering of light leading to higher confinement and spectral narrowing from lower coupling for consequently stronger Q-factor, when compared to the cubic structures.

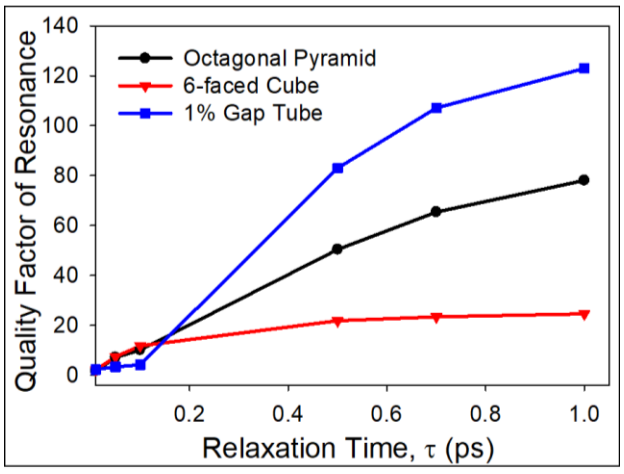

Figure 6.5 Graph showing the change in quality with the relaxation time for 3D graphene geometries with the highest shift in resonant frequency obtained from Figure 6.1.

While Q-factor of resonance is the most critical parameter for dielectric permittivity sensing, section 6.3 concluded that the sensing of vibrational modes in targeted species is controlled most critically by the spectral overlap of the graphene plasmon resonance with the amide band and the absorption in 3D graphene structure. The low or high Q-factor in sensing the vibrational modes only becomes important when selecting between the detection of several modes simultaneously (broadband, low Q-factor) or individually (narrow band, high Q-factor). As discussed in Chapter 1, one of the graphene's advantages stems from the ability to tune the plasmon resonant frequency and absorption dynamically with an externally applied gate voltage that causes a change in the Fermi level (E_F). This tunability allows a perfect overlap with the graphene resonance spectra with that of the targeted analyte. Thus, making it the ability to tune the plasmon resonance with the Fermi level, a critical parameter for detecting the protein and DNA vibrational modes.

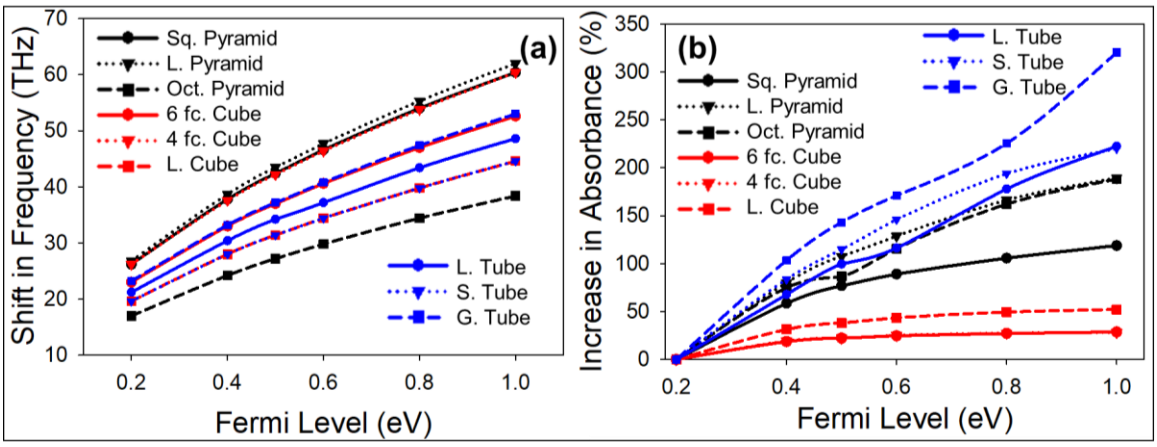

Figure 6.6 (a) Change in the resonant frequency for 3D graphene structures when the Fermi level changes for them. (b) Relative percent change in the absorption by plasmons in 3D graphene with Fermi level.

An advantage of the self-assembled graphene geometries is that all the 3D nanoarchitectures demonstrate a significant shift in resonant frequency with the Fermi level adding credit to their application in vibrational sensing. For all the 3D graphene geometries while the shifts are scaled proportional to the initial resonant frequency (Figure 6.6a), the slope of the shift remains the same across geometries. In contrast, the relative change in absorption across the different 3D graphene geometries is non-uniform (Figure 6.6b). A higher tunability of the absorption in 3D graphene tubes occurs due to the lower interdependent coupling of their plasmon modes, and weaker initial absorption. The strong initial absorption in cubic structure renders them

weaker to absorption tunability with Fermi level due to saturation to the limit of absorption that can be provided by a monolayer of graphene plasmons. The large tunability range of the three sensing control parameters namely, Q-factor, absorption, and resonant frequency in all the 3D graphene nanoarchitectures express their advantages in addition to the novel near-field enhancement modes when building plasmonic devices for sensing applications.

Chapter 7

Conclusion

In this thesis, three-dimensional photonic devices have been presented where the 3D nature of the couplings induced within them offers unique advantages and applications. In the case of split-ring resonators, careful design of the 3D coupling in a cubic structure, which possesses 9 planes of symmetry or 24 rotational symmetries, can deliver isotropic resonances that do not suffer the angle-dependence that plague other forms of SRR structure. The novel design presented here utilizes orthogonal coupling occurring at the vertices of the cubic structure to cause the "split" alignment to be similar to all the vectors of the incident light. Moreover, the redesign of the orthogonal resonator structures allows achieving a completely anisotropic response as well for optical gyroscope applications operating down to 1°/ns.

The clear advantages of three-dimensional coupling mechanisms can be leveraged for graphene plasmonics as well. Three kinds of plasmonic modes can be initiated driven by the three different forms of couplings in the nano-architectured graphene. In 3D graphene cubes, there exists a uniform

orthogonal coupling in all directions between the adjoining faces of the graphene structures. This cross-face coupling yields extremely large surface-area of uniform and strong near-field enhancement that can stretch over 8 times the plasmon wavelength especially useful for studying molecular binding dynamics and surface-enhanced mid-IR vibrational spectroscopy. The 9 planes of symmetry can also be carried forward in irregular structures such as in octagonal pyramids. In such structures, there exists a full 360-degree coupling of all the edges and slant surfaces at the apex of the pyramid and an out-of-plane coupling between the apex and the base of the pyramid. The 360-degree coupling in these geometries, deliver a "volumetric" plasmon-driven enhancement for the graphene structure that is more than 2 orders of magnitude stronger than 2D graphene and is beneficial for sensing dielectric material properties even at low concentrations of the targeted analyte and single-particle vibrational spectroscopy. The tubular structures combine radial coupling with edge couplings along the curvature to deliver edge-based enhancement modes or virtual surface-area modes at the openings of the tube with limited spatial overlap with the substrate, increasing the compatibility of graphene with various substrate environments. The edge modes are highly desirable for non-diffraction-limited plasmonic waveguides and optical interconnects with extremely long propagation lengths. The small diameter tubes offer a 3-fold

advantage; firstly, by utilizing the virtual cross-sectional area of uniform near-field enhancement for detection of analytes as they flow within the graphene tubes. Secondly, no loss of target properties occurs due to the need to attach targeted molecules on the surface of graphene, which is especially desirable in proteins, where surface adhesion changes the in-vivo structure causing them to lose their biological functions. And finally, the ease of integration of the tubular geometry with microfluidic channels and compatibility with diverse substrates. Unlike other forms of 3D graphene, the coupled graphene 3D architectures presented here can realize a strong sensitivity for even extremely low concentrations of targeted analyte alongside a high figure of merit. In addition, the 1% gap-tube structure induces a nearly 6 order of magnitude stronger enhancement of the near-field within the gap that propagates across the entire length of the structures, which find applications in non-diffraction-limited plasmonic waveguide technologies that also benefit with easy silicon integration due to the tube structure.

The 3D graphene geometries also allow breaking the mirror symmetry across multiple planes to achieve a giant plasmonic optical activity in graphene, a concept that has remained almost uninvestigated due to the need for out-of-plane asymmetry. The self-assembled graphene helixes deliver a chirality greater than 40%, which is rapidly tunable by the geometrical

parameters constituting the helical structure. Based on the nanoarchitecture that houses these helixes, the resulting structures can be tubular, cubic or pyramidal helix each with its distinct advantages. The cubic helixes offer the strongest chiral absorption in graphene whereas the tubular helix demonstrates the strongest different enhancement of the incident electric field between the two circular polarizations. Although the pyramid structures don't offer a strong chiral response when compared to a cubic or tubular helix of similar configuration, they form an attractive platform to develop broadband chiral response due to the non-uniformity in the graphene dimensions in the direction of propagation of the incident wave. These advantages alongside the mid-IR protein chirality and vibrational modes, present the possibility of developing vibrational circular dichroism spectroscopy using multi-plane asymmetry in 3D graphene structures.

The self-assembly technique presented in this thesis for realizing the 3D coupled photonic devices is a versatile process that is a combination of top-down and bottom-up fabrication. The processes presented here can be scaled from micro- to nano-scale for delivering 3D SRRs or 3D graphene structures that have been characterized using THz TDS, Raman, FTIR, and SINS technologies. In addition to the 3D couplings, the hollow cavity within these self-assembled 3D materials also offers unique advantages. The volumetric

field within the void of 3D graphene pyramids can excite atoms in the bulk volume, not only those near the surface of graphene, thus, achieving higher carrier generation to deliver fuel cells with lower reaction temperatures and photodetectors with higher efficiency and low response time.

There are several advantages of the 3D graphene nanostructures over conventional carbon nanotubes and fullerene. Compared to solution-processed carbon nanotubes and fullerenes, the combination of top-down and bottom-up fabrication used in 3D graphene tubes allows them to be easily integrated with devices fabricated by lithographic processes. Moreover, the structure, dimensions, and position of the 3D graphene nanostructures are easily controlled by the initial 2D pattern before self-assembly, thus, allowing much greater flexibility for device applications without limitations arising from limited geometries/size inaccuracies within carbon nanotubes and errors introduced during their transfer process.

In addition to their optical properties, self-assembled graphene is beneficial for a variety of other applications. Examples include: (i) gas/water protected containers or barriers for environmentally sensitive chemical/biological materials and molecular storages (due to graphene's gas-impermeability), (ii) targeted drug delivery systems, (iii) enclosed environmental cells for application in transmission electron microscopy

(TEM) providing in situ observation of fuel cells, batteries, catalysts, and biomedical materials, (iv) functional (or tunable) devices achieved through surface modification and encapsulation of nanomaterials such as colloidal nanoparticles, quantum dots, DNA, or segments, and (v) electronic devices and metamaterials (i.e., hollow microcube resonators) created by metal patterning on graphene surfaces.

Further investigation of symmetrical and asymmetrical couplings in 3D graphene structures can reveal unique plasmonic properties and their novel applications. The machine learning technique introduced here to study the plasmonic resonance in 3D graphene structures offers a pathway for developing a rapid design technique for highly efficient plasmonic devices. For a structure to accomplish infinite symmetry planes, the only available geometry is that of a sphere, but the interactions, applications, and integration of such a structure are extremely limited. However, careful design of the self-assembled structured such as broadband multi-layer graphene chirality or multi-plane symmetry through structures such as dodecahedral graphene. These unique advantages can be applied for the early detection of various disease-causing mutations at a molecular level in the DNA or proteins due to the mid-IR vibrational modes. Recent events have proven the need for rapid sensing technologies that can be easily administered in remote areas for a more

public health approach to breakthrough medicine. The widespread cancer burden across the world, which is caused by the short lead time of current detection techniques (<0.1-2 years), unfavorable prognosis at advanced stages, and complications arising after and during lung biopsy, places a severe burden on remotely located, low-income populations. Analysis of circulating tumor DNA, which is a low concentration, but an early disease marker that can save millions of lives. The application of optofluidic 3D graphene-based plasmonic sensors for analysis of mutations in circulating tumor DNA can provide cancer testing outreach to vulnerable populations and improve the prognosis for countless people.

Bibliography

1. Novoselov, K.S., Geim, A.K., Morozov, S.V., Jiang, D., Zhang, Y., Dubonos, S.V., Grigorieva, I.V. and Firsov, A.A., 2004. Electric field effect in atomically thin carbon films. science, 306(5696), pp.666-669.
2. Miró, P., Audiffred, M. and Heine, T., 2014. An atlas of two-dimensional materials. Chemical Society Reviews, 43(18), pp.6537-6554.
3. Das, S., Robinson, J.A., Dubey, M., Terrones, H. and Terrones, M., 2015. Beyond graphene: progress in novel two-dimensional materials and van der Waals solids. Annual Review of Materials Research, 45, pp.1-27.
4. Geng, D. and Yang, H.Y., 2018. Recent advances in growth of novel 2D materials: beyond graphene and transition metal dichalcogenides. Advanced Materials, 30(45), p.1800865.
5. Bonaccorso, F., Sun, Z., Hasan, T. and Ferrari, A.C., 2010. Graphene photonics and optoelectronics. Nature photonics, 4(9), p.611.
6. Novoselov, K.S., Fal, V.I., Colombo, L., Gellert, P.R., Schwab, M.G. and Kim, K., 2012. A roadmap for graphene. nature, 490(7419), pp.192-200.
7. Avouris, P., 2010. Graphene: electronic and photonic properties and devices. Nano letters, 10(11), pp.4285-4294.
8. Liang, L. and Meunier, V., 2013. Electronic and thermoelectric properties of assembled graphene nanoribbons with elastic strain and structural dislocation. Applied Physics Letters, 102(14), p.143101.

9. Cao, Q., Geng, X., Wang, H., Wang, P., Liu, A., Lan, Y. and Peng, Q., 2018. A review of current development of graphene mechanics. Crystals, 8(9), p.357.
10. Castro Neto AH, Guinea F, Peres NMR et al. The electronic properties of graphene. Rev Mod Phys 2009, 81: 109–62.
11. Ju L, Geng B, Horng J et al. Graphene plasmonics for tunable terahertz metamaterials. Nat Nanotechnol 2011, 6: 630–4
12. Horng J, Chen C-F, Geng B et al. Drude conductivity of Dirac fermions in graphene. Phys Rev B 2011, 83: 165113
13. Mak KF, Sfeir MY, Misewich JA et al. The evolution of electronic structure in few-layer graphene revealed by optical spectroscopy. Proc Natl Acad Sci 2010, 107: 14999–5004.
14. Avouris, P., Heinz, T., & Low, T. (Eds.). (2017). 2D Materials: Properties and Devices. Cambridge: Cambridge University Press.
15. Li ZQ, Henriksen EA, Jiang Z et al. Dirac charge dynamics in graphene by infrared spectroscopy. Nat Phys 2008, 4: 6–9
16. Hanson, G.W., 2008. Dyadic Green's functions and guided surface waves for a surface conductivity model of graphene. Journal of Applied Physics, 103(6), p.064302.
17. Mak KF, Ju L, Wang F et al. Optical spectroscopy of graphene: From the far infrared to the ultraviolet. Solid State Commun 2012, 152: 1341–9.
18. Fei, Z., Rodin, A.S., Andreev, G.O., Bao, W., McLeod, A.S., Wagner, M., Zhang, L.M., Zhao, Z., Thiemens, M., Dominguez, G. and Fogler, M.M., 2012. Gate-tuning of graphene plasmons revealed by infrared nano-imaging. Nature, 487(7405), pp.82-85.

19. Abedinpour SH, Vignale G, Principi A et al. Drude weight, plasmon dispersion, and ac conductivity in doped graphene sheets. Phys Rev B - Condens Matter Mater Phys 2011, 84: 1–14.

20. Singh, V., Joung, D., Zhai, L., Das, S., Khondaker, S.I. and Seal, S., 2011. Graphene based materials: past, present and future. Progress in materials science, 56(8), pp.1178-1271.

21. Areshkin, D.A., Gunlycke, D. and White, C.T., 2007. Ballistic transport in graphene nanostrips in the presence of disorder: Importance of edge effects. Nano letters, 7(1), pp.204-210.

22. Chen, J., Badioli, M., Alonso-González, P., Thongrattanasiri, S., Huth, F., Osmond, J., Spasenović, M., Centeno, A., Pesquera, A., Godignon, P. and Elorza, A.Z., 2012. Optical nano-imaging of gate-tunable graphene plasmons. Nature, 487(7405), pp.77-81.

23. Fernández-Rossier, J. and Palacios, J.J., 2007. Magnetism in graphene nanoislands. Physical Review Letters, 99(17), p.177204.

24. Son, Y.W., Cohen, M.L. and Louie, S.G., 2006. Half-metallic graphene nanoribbons. Nature, 444(7117), pp.347-349.

25. Huang, S., Song, C., Zhang, G. and Yan, H., 2016. Graphene plasmonics: physics and potential applications. Nanophotonics, 6(6), pp.1191-1204.

26. Luo, X., Qiu, T., Lu, W. and Ni, Z., 2013. Plasmons in graphene: recent progress and applications. Materials Science and Engineering: R: Reports, 74(11), pp.351-376.

27. Bonaccorso, F., Sun, Z., Hasan, T. and Ferrari, A.C., 2010. Graphene photonics and optoelectronics. Nature photonics, 4(9), p.611.

28. Kumawat, M.K., Thakur, M., Gurung, R.B. and Srivastava, R., 2017. Graphene quantum dots for cell proliferation, nucleus imaging, and photoluminescent sensing applications. Scientific reports, 7(1), pp.1-16.

29. Nematpour, A., Nikoufard, M. and Mehragha, R., 2018. Design and optimization of the plasmonic graphene/InP thin-film solar-cell structure. Laser Physics, 28(6), p.066202.

30. Yang, X., Zhao, X., Yang, K., Liu, Y., Liu, Y., Fu, W. and Luo, Y., 2016. Biomedical applications of terahertz spectroscopy and imaging. Trends in biotechnology, 34(10), pp.810-824.

31. Penke, B., Bogár, F., Paragi, G., Gera, J. and Fülöp, L., 2019. Key peptides and proteins in Alzheimer's disease. Current Protein and Peptide Science, 20(6), pp.577-599.

32. Yadav, K., Yadav, A., Vashistha, P., Pandey, V.P. and Dwivedi, U.N., 2019. Protein misfolding diseases and therapeutic approaches. Current Protein and Peptide Science, 20(12), pp.1226-1245.

33. Xu, R.H., Wei, W., Krawczyk, M., Wang, W., Luo, H., Flagg, K., Yi, S., Shi, W., Quan, Q., Li, K. and Zheng, L., 2017. Circulating tumour DNA methylation markers for diagnosis and prognosis of hepatocellular carcinoma. Nature materials, 16(11), pp.1155-1161.

34. Rodrigo, D., Limaj, O., Janner, D., Etezadi, D., De Abajo, F.J.G., Pruneri, V. and Altug, H., 2015. Mid-infrared plasmonic biosensing with graphene. Science, 349(6244), pp.165-168.

35. Hu, H., Yang, X., Zhai, F., Hu, D., Liu, R., Liu, K., Sun, Z. and Dai, Q., 2016. Far-field nanoscale infrared spectroscopy of vibrational fingerprints of molecules with graphene plasmons. Nature communications, 7(1), pp.1-8.

36. Li, Y., Yan, H., Farmer, D.B., Meng, X., Zhu, W., Osgood, R.M., Heinz, T.F. and Avouris, P., 2014. Graphene plasmon enhanced vibrational sensing of surface-adsorbed layers. Nano letters, 14(3), pp.1573-1577.

37. Marini, A., Silveiro, I. and García de Abajo, F.J., 2015. Molecular sensing with tunable graphene plasmons. Acs Photonics, 2(7), pp.876-882.

38. Farmer, D.B., Avouris, P., Li, Y., Heinz, T.F. and Han, S.J., 2016. Ultrasensitive plasmonic detection of molecules with graphene. Acs Photonics, 3(4), pp.553-557.

39. Sheehan, P.E. and Whitman, L.J., 2005. Detection limits for nanoscale biosensors. Nano letters, 5(4), pp.803-807.

40. Sreekanth, K. V.; Alapan, Y.; ElKabbash, M.; Ilker, E.; Hinczewski, M.; Gurkan, U. A.; De Luca, A.; Strangi, G. Extreme Sensitivity Biosensing Platform Based on Hyperbolic Metamaterials. Nat. Mater. 2016, 15, 621.

41. Stiles, P.L., Dieringer, J.A., Shah, N.C. and Van Duyne, R.P., 2008. Surface-enhanced Raman spectroscopy. Annu. Rev. Anal. Chem., 1, pp.601-626.

42. Singh, E., Meyyappan, M. and Nalwa, H.S., 2017. Flexible graphene-based wearable gas and chemical sensors. ACS applied materials & interfaces, 9(40), pp.34544-34586.

43. Low, T. and Avouris, P., 2014. Graphene plasmonics for terahertz to mid-infrared applications. ACS nano, 8(2), pp.1086-1101.

44. Zundel, L. and Manjavacas, A., 2017. Spatially resolved optical sensing using graphene nanodisk arrays. ACS photonics, 4(7), pp.1831-1838.

45. Thongrattanasiri, S., Koppens, F.H. and De Abajo, F.J.G., 2012. Complete optical absorption in periodically patterned graphene. Physical review letters, 108(4), p.047401.

46. Luan, Y., McDermott, L., Hu, F. and Fei, Z., 2020. Tip-and Plasmon-Enhanced Infrared Nanoscopy for Ultrasensitive Molecular Characterizations. Physical Review Applied, 13(3), p.034020.
47. Marini, A., Silveiro, I. and García de Abajo, F.J., 2015. Molecular sensing with tunable graphene plasmons. Acs Photonics, 2(7), pp.876-882.
48. Chen, J., Badioli, M., Alonso-González, P., Thongrattanasiri, S., Huth, F., Osmond, J., Spasenović, M., Centeno, A., Pesquera, A., Godignon, P. and Elorza, A.Z., 2012. Optical nano-imaging of gate-tunable graphene plasmons. Nature, 487(7405), pp.77-81.
49. Zhang, Q., Li, X., Hossain, M.M., Xue, Y., Zhang, J., Song, J., Liu, J., Turner, M.D., Fan, S., Bao, Q. and Gu, M., 2014. Graphene surface plasmons at the near-infrared optical regime. Scientific reports, 4, p.6559.
50. Xu, H., Zhang, Z., Wang, S., Liu, Y., Zhang, J., Chen, D., Ouyang, J. and Yang, J., 2019. Tunable Graphene-Based Plasmon-Induced Transparency Based on Edge Mode in the Mid-Infrared Region. Nanomaterials, 9(3), p.448.
51. Kim, Y., Yu, S. and Park, N., 2017. Low-dimensional gap plasmons for enhanced light-graphene interactions. Scientific reports, 7, p.43333.
52. Lee, I.H., Yoo, D., Avouris, P., Low, T. and Oh, S.H., 2019. Graphene acoustic plasmon resonator for ultrasensitive infrared spectroscopy. Nature nanotechnology, 14(4), pp.313-319.
53. Pisarra, M., Sindona, A., Riccardi, P., Silkin, V.M. and Pitarke, J.M., 2014. Acoustic plasmons in extrinsic free-standing graphene. New Journal of Physics, 16(8), p.083003.
54. Chen, S., Autore, M., Li, J., Li, P., Alonso-Gonzalez, P., Yang, Z., Martin-Moreno, L., Hillenbrand, R. and Nikitin, A.Y., 2017. Acoustic

graphene plasmon nanoresonators for field-enhanced infrared molecular spectroscopy. ACS photonics, 4(12), pp.3089-3097.

55. Fang, Z., Wang, Y., Schlather, A.E., Liu, Z., Ajayan, P.M., García de Abajo, F.J., Nordlander, P., Zhu, X. and Halas, N.J., 2014. Active tunable absorption enhancement with graphene nanodisk arrays. Nano letters, 14(1), pp.299-304.

56. Aglieri, V., Jin, X., Rovere, A., Piccoli, R., Caraffini, D., Tuccio, S., De Angelis, F., Morandotti, R., Macaluso, R., Toma, A. and Razzari, L., 2020. Improving nanoscale terahertz field localization by means of sharply tapered resonant nanoantennas. Nanophotonics, 9(3), pp.683-690.

57. Freitag, M., Low, T. and Avouris, P., 2013. Increased responsivity of suspended graphene photodetectors. Nano letters, 13(4), pp.1644-1648.

58. Kim, S.Y. and Park, H.S., 2009. Multilayer friction and attachment effects on energy dissipation in graphene nanoresonators. Applied Physics Letters, 94(10), p.101918.

59. Shi, Q., Cha, Y., Song, Y., Lee, J.I., Zhu, C., Li, X., Song, M.K., Du, D. and Lin, Y., 2016. 3D graphene-based hybrid materials: synthesis and applications in energy storage and conversion. Nanoscale, 8(34), pp.15414-15447.

60. Yang, Z., Chabi, S., Xia, Y. and Zhu, Y., 2015. Preparation of 3D graphene-based architectures and their applications in supercapacitors. Progress in Natural Science: Materials International, 25(6), pp.554-562.

61. Yan, H., Li, X., Chandra, B., Tulevski, G., Wu, Y., Freitag, M., Zhu, W., Avouris, P. and Xia, F., 2012. Tunable infrared plasmonic devices using graphene/insulator stacks. Nature nanotechnology, 7(5), pp.330-334.

62. Rodrigo, D., Tittl, A., Limaj, O., De Abajo, F.J.G., Pruneri, V. and Altug, H., 2017. Double-layer graphene for enhanced tunable infrared plasmonics. Light: Science & Applications, 6(6), pp.e16277-e16277.

63. Gomez-Diaz, J.S., Moldovan, C., Capdevila, S., Romeu, J., Bernard, L.S., Magrez, A., Ionescu, A.M. and Perruisseau-Carrier, J., 2015. Self-biased reconfigurable graphene stacks for terahertz plasmonics. Nature communications, 6(1), pp.1-8.

64. Wang, B., Zhang, X., Ping Loh, K. and Teng, J., 2014. Tunable broadband transmission and phase modulation of light through graphene multilayers. Journal of Applied Physics, 115(21), p.213102.

65. Ma, W., Huang, Z., Bai, X., Zhan, P. and Liu, Y., 2017. Dual-band light focusing using stacked graphene metasurfaces. ACS Photonics, 4(7), pp.1770-1775.

66. Tamagnone, M., Gomez-Diaz, J.S., Mosig, J.R. and Perruisseau-Carrier, J., 2012. Reconfigurable terahertz plasmonic antenna concept using a graphene stack. Applied Physics Letters, 101(21), p.214102.

67. Huang, Y., Zhong, S., Shen, Y., Yao, L., Yu, Y. and Cui, D., 2017. Graphene/insulator stack based ultrasensitive terahertz sensor with surface plasmon resonance. IEEE Photonics Journal, 9(6), pp.1-11.

68. Huang, Y., Zhong, S., Yao, H. and Cui, D., 2017. Tunable terahertz plasmonic sensor based on graphene/insulator stacks. IEEE Photonics Journal, 9(1), pp.1-10.

69. Vickery, J.L., Patil, A.J. and Mann, S., 2009. fabrication of graphene–polymer nanocomposites with higher-order three-dimensional architectures. Advanced Materials, 21(21), pp.2180-2184.

70. Chen, W. and Yan, L., 2011. In situ self-assembly of mild chemical reduction graphene for three-dimensional architectures. Nanoscale, 3(8), pp.3132-3137.

71. Xu, Y., Sheng, K., Li, C. and Shi, G., 2010. Self-assembled graphene hydrogel via a one-step hydrothermal process. ACS nano, 4(7), pp.4324-4330.

72. Chen, Z., Ren, W., Gao, L., Liu, B., Pei, S. and Cheng, H.M., 2011. Three-dimensional flexible and conductive interconnected graphene networks grown by chemical vapour deposition. Nature materials, 10(6), p.424.

73. Sun, L., Kong, W., Jiang, Y., Wu, H., Jiang, K., Wang, J. and Fan, S., 2015. Super-aligned carbon nanotube/graphene hybrid materials as a framework for sulfur cathodes in high performance lithium sulfur batteries. Journal of Materials Chemistry A, 3(10), pp.5305-5312.

74. Shi, Q., Cha, Y., Song, Y., Lee, J.I., Zhu, C., Li, X., Song, M.K., Du, D. and Lin, Y., 2016. 3D graphene-based hybrid materials: synthesis and applications in energy storage and conversion. Nanoscale, 8(34), pp.15414-15447.

75. Sun, L., Wang, L., Tian, C., Tan, T., Xie, Y., Shi, K., Li, M. and Fu, H., 2012. Nitrogen-doped graphene with high nitrogen level via a one-step hydrothermal reaction of graphene oxide with urea for superior capacitive energy storage. Rsc Advances, 2(10), pp.4498-4506.

76. Song, Y., Chen, C. and Wang, C., 2015. Graphene/enzyme-encrusted three-dimensional carbon micropillar arrays for mediatorless micro-biofuel cells. Nanoscale, 7(16), pp.7084-7090.

77. Xu, C., Wu, Y., Zhao, X., Wang, X., Du, G., Zhang, J. and Tu, J., 2015. Sulfur/three-dimensional graphene composite for high performance lithium–sulfur batteries. Journal of Power Sources, 275, pp.22-25.

78. Shin, Y.C., Kang, S.H., Lee, J.H., Kim, B., Hong, S.W. and Han, D.W., 2018. Three-dimensional graphene oxide-coated polyurethane foams beneficial to myogenesis. Journal of Biomaterials science, Polymer edition, 29(7-9), pp.762-774.

79. Liu, X.L., Wang, C., Wu, Q.H. and Wang, Z., 2014. Preconcentration of chlorophenols in water samples using three-dimensional graphene-based magnetic nanocomposite as absorbent. Chinese Chemical Letters, 25(8), pp.1185-1189.

80. Wei, L., Jiang, W., Yuan, Y., Goh, K., Yu, D., Wang, L. and Chen, Y., 2015. Synthesis of free-standing carbon nanohybrid by directly growing carbon nanotubes on air-sprayed graphene oxide paper and its application in supercapacitor. Journal of Solid State Chemistry, 224, pp.45-51.

81. Huang, Z., Chen, H., Huang, Y., Ge, Z., Zhou, Y., Yang, Y., Xiao, P., Liang, J., Zhang, T., Shi, Q. and Li, G., 2018. Ultra-Broadband Wide-Angle Terahertz Absorption Properties of 3D Graphene Foam. Advanced Functional Materials, 28(2), p.1704363.

82. Chen, H., Ma, W., Huang, Z., Zhang, Y., Huang, Y. and Chen, Y., 2019. Graphene-Based Materials toward Microwave and Terahertz Absorbing Stealth Technologies. Advanced Optical Materials, 7(8), p.1801318.

83. Zeranska-Chudek, K., Lapinska, A., Wroblewska, A., Judek, J., Duzynska, A., Pawlowski, M., Witowski, A.M. and Zdrojek, M., 2018. Study of the absorption coefficient of graphene-polymer composites. Scientific reports, 8(1), pp.1-8.

84. Xu, S.T., Fan, F., Cheng, J., Chen, H., Ma, W., Huang, Y. and Chang, S., 2019. Active Terahertz Shielding and Absorption Based on Graphene Foam Modulated by Electric and Optical Field Excitation. Advanced Optical Materials, 7(18), p.1900555.

85. Wang, P., Liang, O., Zhang, W., Schroeder, T. and Xie, Y.H., 2013. Ultra-sensitive graphene-plasmonic hybrid platform for label-free detection. Advanced Materials, 25(35), pp.4918-4924.

86. Reserbat-Plantey, A., Kalita, D., Han, Z., Ferlazzo, L., Autier-Laurent, S., Komatsu, K., Li, C., Weil, R., Ralko, A., Marty, L. and Guéron, S., 2014. Strain superlattices and macroscale suspension of graphene induced by corrugated substrates. Nano letters, 14(9), pp.5044-5051.

87. Kim, J., Son, H., Cho, D.J., Geng, B., Regan, W., Shi, S., Kim, K., Zettl, A., Shen, Y.R. and Wang, F., 2012. Electrical control of optical plasmon resonance with graphene. Nano letters, 12(11), pp.5598-5602.

88. Wang, R., Hao, Y., Wang, Z., Gong, H. and Thong, J.T., 2010. Large-diameter graphene nanotubes synthesized using Ni nanowire templates. Nano letters, 10(12), pp.4844-4850.

89. Matthaiakakis, N., Mizuta, H. and Charlton, M.D.B., 2016. Strong modulation of plasmons in Graphene with the use of an Inverted pyramid array diffraction grating. Scientific reports, 6, p.27550.

90. Xie, X., Ju, L., Feng, X., Sun, Y., Zhou, R., Liu, K., Fan, S., Li, Q. and Jiang, K., 2009. Controlled fabrication of high-quality carbon nanoscrolls from monolayer graphene. Nano letters, 9(7), pp.2565-2570.

91. Zhu, B., Niu, Z., Wang, H., Leow, W.R., Wang, H., Li, Y., Zheng, L., Wei, J., Huo, F. and Chen, X., 2014. Microstructured graphene arrays for highly sensitive flexible tactile sensors. Small, 10(18), pp.3625-3631.

92. Mueller, T., Xia, F. and Avouris, P., 2010. Graphene photodetectors for high-speed optical communications. Nature photonics, 4(5), p.297.

93. Salihoglu, O., Balci, S. and Kocabas, C., 2012. Plasmon-polaritons on graphene-metal surface and their use in biosensors. Applied Physics Letters, 100(21), p.213110.

94. Bao, Q., Zhang, H., Wang, B., Ni, Z., Lim, C.H.Y.X., Wang, Y., Tang, D.Y. and Loh, K.P., 2011. Broadband graphene polarizer. Nature photonics, 5(7), p.411.

95. Johansson, A., Myllyperkiö, P., Koskinen, P., Aumanen, J., Koivistoinen, J., Tsai, H.C., Chen, C.H., Chang, L.Y., Hiltunen, V.M., Manninen, J.J. and Woon, W.Y., 2017. Optical forging of graphene into three-dimensional shapes. Nano letters, 17(10), pp.6469-6474.

96. Choi, J., Kim, H.J., Wang, M.C., Leem, J., King, W.P. and Nam, S., 2015. Three-dimensional integration of graphene via swelling, shrinking, and adaptation. Nano letters, 15(7), pp.4525-4531.

97. Gill, S.T., Hinnefeld, J.H., Zhu, S., Swanson, W.J., Li, T. and Mason, N., 2015. Mechanical control of graphene on engineered pyramidal strain arrays. ACS nano, 9(6), pp.5799-5806.

98. Wang, M.C., Chun, S., Han, R.S., Ashraf, A., Kang, P. and Nam, S., 2015. Heterogeneous, three-dimensional texturing of graphene. Nano letters, 15(3), pp.1829-1835.

99. Pacakova, B., Vejpravova, J., Repko, A., Mantlikova, A. and Kalbac, M., 2015. Formation of wrinkles on graphene induced by nanoparticles: atomic force microscopy study. Carbon, 95, pp.573-579.

100. Chen, R., Yang, C., Jia, Y., Guo, L. and Chen, J., 2019. Plasmon reflection reveals local electronic properties of natural graphene wrinkles. Chinese Physics B, 28(11), p.117302.

101. Fasolino, A., Los, J.H. and Katsnelson, M.I., 2007. Intrinsic ripples in graphene. Nature materials, 6(11), pp.858-861.

102. Luo, J., Jang, H.D., Sun, T., Xiao, L., He, Z., Katsoulidis, A.P., Kanatzidis, M.G., Gibson, J.M. and Huang, J., 2011. Compression and aggregation-resistant particles of crumpled soft sheets. ACS nano, 5(11), pp.8943-8949.

103. Pan, Z., Liu, N., Fu, L. and Liu, Z., 2011. Wrinkle engineering: a new approach to massive graphene nanoribbon arrays. Journal of the American Chemical Society, 133(44), pp.17578-17581.

104. Zhu, W., Low, T., Perebeinos, V., Bol, A.A., Zhu, Y., Yan, H., Tersoff, J. and Avouris, P., 2012. Structure and electronic transport in graphene wrinkles. Nano letters, 12(7), pp.3431-3436.

105. Pacakova, B., Verhagen, T., Bousa, M., Hübner, U., Vejpravova, J., Kalbac, M. and Frank, O., 2017. Mastering the wrinkling of self-supported graphene. Scientific reports, 7(1), pp.1-11.

106. Chen, R., Yang, C., Jia, Y., Guo, L. and Chen, J., 2019. Plasmon reflection reveals local electronic properties of natural graphene wrinkles. Chinese Physics B, 28(11), p.117302.

107. Yang, C., Chen, R., Jia, Y., Guo, L. and Chen, J., 2017. Asymmetrical plasmon reflections in tapered graphene ribbons with wrinkle edges. Chinese Physics B, 26(7), p.074220.

108. Slipchenko, T.M., Nesterov, M.L., Hillenbrand, R., Nikitin, A.Y. and Martín-Moreno, L., 2017. Graphene plasmon reflection by corrugations. ACS Photonics, 4(12), pp.3081-3088.

109. Yue, K., Gao, W., Huang, R. and Liechti, K.M., 2012. Analytical methods for the mechanics of graphene bubbles. Journal of Applied Physics, 112(8), p.083512.

110. Stolyarova, E., Stolyarov, D., Bolotin, K., Ryu, S., Liu, L., Rim, K.T., Klima, M., Hybertsen, M., Pogorelsky, I., Pavlishin, I. and Kusche, K., 2009. Observation of graphene bubbles and effective mass transport under graphene films. Nano letters, 9(1), pp.332-337.

111. Su, D., 2012. Macroporous 'bubble'graphene film via template-directed ordered-assembly for high rate supercapacitors. Chemical communications, 48(57), pp.7149-7151.

112. Georgiou, T., Britnell, L., Blake, P., Gorbachev, R.V., Gholinia, A., Geim, A.K., Casiraghi, C. and Novoselov, K.S., 2011. Graphene bubbles with controllable curvature. Applied Physics Letters, 99(9), p.093103.

113. Wang, X., Zhang, Y., Zhi, C., Wang, X., Tang, D., Xu, Y., Weng, Q., Jiang, X., Mitome, M., Golberg, D. and Bando, Y., 2013. Three-dimensional strutted graphene grown by substrate-free sugar blowing for high-power-density supercapacitors. Nature communications, 4(1), pp.1-8.

114. Sheng, L., Liang, Y., Jiang, L., Wang, Q., Wei, T., Qu, L. and Fan, Z., 2015. Bubble-decorated honeycomb-like graphene film as ultrahigh sensitivity pressure sensors. Advanced Functional Materials, 25(41), pp.6545-6551.

115. Khestanova, E., Guinea, F., Fumagalli, L., Geim, A.K. and Grigorieva, I.V., 2016. Universal shape and pressure inside bubbles appearing in van der Waals heterostructures. Nature communications, 7(1), pp.1-10.

116. Fei, Z., Foley IV, J.J., Gannett, W., Liu, M.K., Dai, S., Ni, G.X., Zettl, A., Fogler, M.M., Wiederrecht, G.P., Gray, S.K. and Basov, D.N., 2016. Ultraconfined plasmonic hotspots inside graphene nanobubbles. Nano letters, 16(12), pp.7842-7848.

117. Barcelos, I.D., Cadore, A.R., Campos, L.C., Malachias, A., Watanabe, K., Taniguchi, T., Maia, F.C., Freitas, R. and Deneke, C., 2015. Graphene/h-

BN plasmon–phonon coupling and plasmon delocalization observed by infrared nano-spectroscopy. Nanoscale, 7(27), pp.11620-11625.

118. Ning, X., Wang, X., Zhang, Y., Yu, X., Choi, D., Zheng, N., Kim, D.S., Huang, Y., Zhang, Y. and Rogers, J.A., 2018. Assembly of advanced materials into 3D functional structures by methods inspired by origami and kirigami: a review. Advanced Materials Interfaces, 5(13), p.1800284.

119. Blees, M.K., Barnard, A.W., Rose, P.A., Roberts, S.P., McGill, K.L., Huang, P.Y., Ruyack, A.R., Kevek, J.W., Kobrin, B., Muller, D.A. and McEuen, P.L., 2015. Graphene kirigami. Nature, 524(7564), pp.204-207.

120. Mortazavi, B., Lherbier, A., Fan, Z., Harju, A., Rabczuk, T. and Charlier, J.C., 2017. Thermal and electronic transport characteristics of highly stretchable graphene kirigami. Nanoscale, 9(42), pp.16329-16341.

121. Hua, Z., Zhao, Y., Dong, S., Yu, P., Liu, Y., Wei, N. and Zhao, J., 2017. Large stretchability and failure mechanism of graphene kirigami under tension. Soft matter, 13(47), pp.8930-8939.

122. Moura, A., Galvao, D.S. and Autreto, P.A.D.S., 2020. Ballistic Properties of Highly Stretchable Graphene Kirigami Pyramid. arXiv preprint arXiv:2001.09546.

123. Bahamon, D.A., Qi, Z., Park, H.S., Pereira, V.M. and Campbell, D.K., 2016. Graphene kirigami as a platform for stretchable and tunable quantum dot arrays. Physical Review B, 93(23), p.235408.

124. Ebbesen, T.W. and Hiura, H., 1995. Graphene in 3-dimensions: Towards graphite origami. Advanced Materials, 7(6), pp.582-586.

125. Johnson, M., Chen, Y., Hovet, S., Xu, S., Wood, B., Ren, H., Tokuda, J. and Tse, Z.T.H., 2017. Fabricating biomedical origami: a state-of-the-art review. International journal of computer assisted radiology and surgery, 12(11), pp.2023-2032.

126. Origami-inspired active graphene-based paper for programmable instant self-folding walking devices

127. Zhu, S. and Li, T., 2014. Hydrogenation-assisted graphene origami and its application in programmable molecular mass uptake, storage, and release. ACS nano, 8(3), pp.2864-2872.

128. Miskin, M.Z., Dorsey, K.J., Bircan, B., Han, Y., Muller, D.A., McEuen, P.L. and Cohen, I., 2018. Graphene-based bimorphs for micron-sized, autonomous origami machines. Proceedings of the National Academy of Sciences, 115(3), pp.466-470.

129. Costa, A.T., Ferreira, M.S., Hallam, T., Duesberg, G.S. and Neto, A.C., 2013. Origami-based spintronics in graphene. EPL (Europhysics Letters), 104(4), p.47001.

130. Xu, W., Qin, Z., Chen, C.T., Kwag, H.R., Ma, Q., Sarkar, A., Buehler, M.J. and Gracias, D.H., 2017. Ultrathin thermoresponsive self-folding 3D graphene. Science advances, 3(10), p.e1701084.

131. Cho, J.H., Keung, M.D., Verellen, N., Lagae, L., Moshchalkov, V.V., Van Dorpe, P. and Gracias, D.H., 2011. Nanoscale origami for 3D optics. Small, 7(14), pp.1943-1948.

132. Cho, J.H., Hu, S. and Gracias, D.H., 2008. Self-assembly of orthogonal three-axis sensors. Applied Physics Letters, 93(4), p.043505.

133. Agarwal, K., Hwang, S., Bartnik, A., Buchele, N., Mishra, A. and Cho, J.H., 2018. Small-Scale Biological and Artificial Multidimensional Sensors for 3D Sensing. Small, 14(35), p.1801145.

134. Burckel, D.B., Wendt, J.R., Ten Eyck, G.A., Ginn, J.C., Ellis, A.R., Brener, I. and Sinclair, M.B., 2010. Micrometer-scale cubic unit cell 3D metamaterial layers. Advanced Materials, 22(44), pp.5053-5057.

135. Liu, Z., Du, S., Cui, A., Li, Z., Fan, Y., Chen, S., Li, W., Li, J. and Gu, C., 2017. High-Quality-Factor Mid-Infrared Toroidal Excitation in Folded 3D Metamaterials. Advanced Materials, 29(17), p.1606298.

136. Song, Y.M., Xie, Y., Malyarchuk, V., Xiao, J., Jung, I., Choi, K.J., Liu, Z., Park, H., Lu, C., Kim, R.H. and Li, R., 2013. Digital cameras with designs inspired by the arthropod eye. Nature, 497(7447), pp.95-99.

137. Takei, K., Yu, Z., Zheng, M., Ota, H., Takahashi, T. and Javey, A., 2014. Highly sensitive electronic whiskers based on patterned carbon nanotube and silver nanoparticle composite films. Proceedings of the National Academy of Sciences, 111(5), pp.1703-1707.

138. Cho, J.H., Hu, S. and Gracias, D.H., 2010, December. A three dimensional self-folding package (SFP) for electronics. In 2010 MRS Spring Meeting (pp. 317-321).

139. Rogers, J., Huang, Y., Schmidt, O.G. and Gracias, D.H., 2016. Origami mems and nems. Mrs Bulletin, 41(2), pp.123-129.

140. Leong, T.G., Zarafshar, A.M. and Gracias, D.H., 2010. Three-dimensional fabrication at small size scales. Small, 6(7), pp.792-806.

141. Liu, C., Agarwal, K., Zhang, Y., Chowdhury, D.R., Azad, A.K. and Cho, J.H., 2016. Displacement current mediated resonances in terahertz metamaterials. Advanced Optical Materials, 4(8), pp.1302-1309.

142. Park, S.J., Hong, J.T., Choi, S.J., Kim, H.S., Park, W.K., Han, S.T., Park, J.Y., Lee, S., Kim, D.S. and Ahn, Y.H., 2014. Detection of microorganisms using terahertz metamaterials. Scientific reports, 4, p.4988.

143. Wellenzohn, M. and Brandl, M., 2015. A theoretical design of a biosensor device based on split ring resonators for operation in the microwave regime. Procedia engineering, 120, pp.865-869.

144. Xu, X., Peng, B., Li, D., Zhang, J., Wong, L.M., Zhang, Q., Wang, S. and Xiong, Q., 2011. Flexible visible–infrared metamaterials and their applications in highly sensitive chemical and biological sensing. Nano letters, 11(8), pp.3232-3238.

145. Melik, R., Unal, E., Kosku Perkgoz, N., Puttlitz, C. and Demir, H.V., 2009. Flexible metamaterials for wireless strain sensing. Applied Physics Letters, 95(18), p.181105.

146. Rusni, I.M., Ismail, A., Alhawari, A.R.H., Hamidon, M.N. and Yusof, N.A., 2014. An aligned-gap and centered-gap rectangular multiple split ring resonator for dielectric sensing applications. Sensors, 14(7), pp.13134-13148.

147. Horestani, A.K., Fumeaux, C., Al-Sarawi, S.F. and Abbott, D., 2012. Displacement sensor based on diamond-shaped tapered split ring resonator. IEEE Sensors Journal, 13(4), pp.1153-1160.

148. Fischer, B.M., Walther, M. and Jepsen, P.U., 2002. Far-infrared vibrational modes of DNA components studied by terahertz time-domain spectroscopy. Physics in Medicine & Biology, 47(21), p.3807.

149. Liu, X., MacNaughton, S., Shrekenhamer, D.B., Tao, H., Selvarasah, S., Totachawattana, A., Averitt, R.D., Dokmeci, M.R., Sonkusale, S. and Padilla, W.J., 2010. Metamaterials on parylene thin film substrates: Design, fabrication, and characterization at terahertz frequency. Applied Physics Letters, 96(1), p.011906.

150. Chen, C.C., Ishikawa, A., Tang, Y.H., Shiao, M.H., Tsai, D.P. and Tanaka, T., 2015. Uniaxial-isotropic Metamaterials by Three-Dimensional Split-Ring Resonators. Advanced Optical Materials, 3(1), pp.44-48.

151. Magdanz, V., Sanchez, S. and Schmidt, O.G., 2013. Development of a sperm-flagella driven micro-bio-robot. Advanced Materials, 25(45), pp.6581-6588.

152. Bajić, J.S., Stupar, D.Z., Manojlović, L.M., Slankamenac, M.P. and Živanov, M.B., 2012. A simple, low-cost, high-sensitivity fiber-optic tilt sensor. Sensors and Actuators A: Physical, 185, pp.33-38.

153. Agarwal, K., Liu, C., Joung, D., Park, H.R., Oh, S.H. and Cho, J.H., 2017. Three-dimensional anisotropic metamaterials as triaxial optical inclinometers. Scientific reports, 7(1), pp.1-12.

154. Joung, D., Agarwal, K., Park, H.R., Liu, C., Oh, S.H. and Cho, J.H., 2016. Self-Assembled Multifunctional 3D Microdevices. Advanced Electronic Materials, 2(6), p.1500459.

155. Agarwal, K., Liu, C., Joung, D., Park, H.R., Jeong, J., Kim, D.S. and Cho, J.H., 2017. Three-dimensionally coupled THz octagrams as isotropic metamaterials. ACS Photonics, 4(10), pp.2436-2445.

156. Karacolak, T., Moreland, E.C. and Topsakal, E., 2013. Cole–cole model for glucose-dependent dielectric properties of blood plasma for continuous glucose monitoring. Microwave and Optical Technology Letters, 55(5), pp.1160-1164.

157. Cho, S.H., Xue, N., Cauller, L., Rosellini, W. and Lee, J.B., 2012. A SU-8-based fully integrated biocompatible inductively powered wireless neurostimulator. Journal of microelectromechanical systems, 22(1), pp.170-176.

158. Lin, J.C. and Tseng, S.M., 2001. Surface characterization and platelet adhesion studies on polyethylene surface with hirudin immobilization. Journal of Materials Science: Materials in Medicine, 12(9), pp.827-832.

159. Sugiyama, K., Matsumoto, T. and Yamazaki, Y., 2000. Evaluation of biocompatibility of the surface of polyethylene films modified with various water soluble polymers using Ar plasma-post polymerization technique. Macromolecular Materials and Engineering, 282(1), pp.5-12.

160. Azam, A., Laflin, K.E., Jamal, M., Fernandes, R. and Gracias, D.H., 2011. Self-folding micropatterned polymeric containers. Biomedical microdevices, 13(1), pp.51-58.

161. Randall, C.L., Gultepe, E. and Gracias, D.H., 2012. Self-folding devices and materials for biomedical applications. Trends in biotechnology, 30(3), pp.138-146.

162. Joung, D., Gu, T. and Cho, J.H., 2016. Tunable optical transparency in self-assembled three-dimensional polyhedral graphene oxide. ACS nano, 10(10), pp.9586-9594.

163. Lindquist, N.C., Nagpal, P., Lesuffleur, A., Norris, D.J. and Oh, S.H., 2010. Three-dimensional plasmonic nanofocusing. Nano letters, 10(4), pp.1369-1373.

164. Oh, S.S. and Hess, O., 2015. Chiral metamaterials: enhancement and control of optical activity and circular dichroism. Nano Convergence, 2(1), p.24.

165. Sharma, V., Crne, M., Park, J.O. and Srinivasarao, M., 2009. Structural origin of circularly polarized iridescence in jeweled beetles. science, 325(5939), pp.449-451.

166. Kelly, S.M., Jess, T.J. and Price, N.C., 2005. How to study proteins by circular dichroism. Biochimica et Biophysica Acta (BBA)-Proteins and Proteomics, 1751(2), pp.119-139.

167. Choi, W.J., Cheng, G., Huang, Z., Zhang, S., Norris, T.B. and Kotov, N.A., 2019. Terahertz circular dichroism spectroscopy of biomaterials enabled by kirigami polarization modulators. Nature materials, 18(8), p.820.

168. Vollmer, F. and Fischer, P., 2006. Ring-resonator-based frequency-domain optical activity measurements of a chiral liquid. Optics letters, 31(4), pp.453-455.

169. Hentschel, M., Schäferling, M., Duan, X., Giessen, H. and Liu, N., 2017. Chiral plasmonics. Science advances, 3(5), p.e1602735.

170. Sanders, S., May, A., Alabastri, A. and Manjavacas, A., 2018. Extraordinary enhancement of quadrupolar transitions using nanostructured graphene. ACS Photonics, 5(8), pp.3282-3290.

171. Pandey, S., Gultepe, E. and Gracias, D.H., 2013. Origami inspired self-assembly of patterned and reconfigurable particles. JoVE (Journal of Visualized Experiments), (72), p.e50022.

172. Boncheva, M., Andreev, S.A., Mahadevan, L., Winkleman, A., Reichman, D.R., Prentiss, M.G., Whitesides, S. and Whitesides, G.M., 2005. Magnetic self-assembly of three-dimensional surfaces from planar sheets. Proceedings of the National Academy of Sciences, 102(11), pp.3924-3929.

173. Kong, X.T., Zhao, R., Wang, Z. and Govorov, A.O., 2017. Mid-infrared plasmonic circular dichroism generated by graphene nanodisk assemblies. Nano letters, 17(8), pp.5099-5105.

174. Guo, J., Kim, J.Y., Zhang, M., Wang, H., Stein, A., Murray, C.B., Kotov, N.A. and Kagan, C.R., 2019. Chemo-and Thermo-Mechanically Configurable 3D Optical Metamaterials Constructed from Colloidal Nanocrystal Assemblies. ACS nano, 14(2), pp. 1427-1435.

175. Liu, Z., Du, H., Li, J., Lu, L., Li, Z.Y. and Fang, N.X., 2018. Nano-kirigami with giant optical chirality. Science advances, 4(7), p.eaat4436.

176. Gansel, J.K., Thiel, M., Rill, M.S., Decker, M., Bade, K., Saile, V., von Freymann, G., Linden, S. and Wegener, M., 2009. Gold helix photonic metamaterial as broadband circular polarizer. Science, 325(5947), pp.1513-1515.

177. Hidalgo, B. and Goodman, M., 2013. Multivariate or multivariable regression?. American journal of public health, 103(1), pp.39-40.

178. Kadel, S., Persico, M., Thibodeau, J., Lainé, C. and Bazinet, L., 2019. Use of redundancy analysis and multivariate regression models to select the significant membrane properties affecting peptide migration during electrodialysis with filtration membranes. Separation and Purification Technology, 221, pp.114-125.

179. Kasera, S., Herrmann, L.O., Del Barrio, J., Baumberg, J.J. and Scherman, O.A., 2014. Quantitative multiplexing with nano-self-assemblies in SERS. Scientific reports, 4, p.6785.

180. Yasukuni, R., Gillibert, R., Triba, M.N., Grinyte, R., Pavlov, V. and de la Chapelle, M.L., 2019. Quantitative analysis of SERS spectra of MnSOD over fluctuated aptamer signals using multivariate statistics. Nanophotonics, 8(9), pp.1477-1483.

181. Gansel, J.K., Wegener, M., Burger, S. and Linden, S., 2010. Gold helix photonic metamaterials: a numerical parameter study. Optics express, 18(2), pp.1059-1069.

182. Joung, D., Nemilentsau, A., Agarwal, K., Dai, C., Liu, C., Su, Q., Li, J., Low, T., Koester, S.J. and Cho, J.H., 2017. Self-assembled three-dimensional graphene-based polyhedrons inducing volumetric light confinement. Nano letters, 17(3), pp.1987-1994.

183. Agarwal, K., Dai, C., Joung, D. and Cho, J.H., 2018. Nano-Architecture Driven Plasmonic Field Enhancement in 3D Graphene Structures. ACS nano, 13(2), pp.1050-1059.

184. Childres, I., Jauregui, L.A., Park, W., Cao, H. and Chen, Y.P., 2013. Raman spectroscopy of graphene and related materials. New developments in photon and materials research, 1, pp.1-20.

185. Wong, J.H., Wu, B.R. and Lin, M.F., 2012. Strain effect on the electronic properties of single layer and bilayer graphene. The Journal of Physical Chemistry C, 116(14), pp.8271-8277.

186. Choi, S.M., Jhi, S.H. and Son, Y.W., 2010. Effects of strain on electronic properties of graphene. Physical Review B, 81(8), p.081407.

187. Ooi, K.J., Chu, H.S., Hsieh, C.Y., Tan, D.T. and Ang, L.K., 2015. Highly efficient midinfrared on-chip electrical generation of graphene plasmons by inelastic electron tunneling excitation. Physical Review Applied, 3(5), p.054001.

188. Jablan, M., Buljan, H. and Soljačić, M., 2009. Plasmonics in graphene at infrared frequencies. Physical review B, 80(24), p.245435.

189. Dai, C., Agarwal, K. and Cho, J.H., 2018. Ion-Induced Localized Nanoscale Polymer Reflow for Three-Dimensional Self-Assembly. ACS nano, 12(10), pp.10251-10261.

190. Dean, C.R., Young, A.F., Meric, I., Lee, C., Wang, L., Sorgenfrei, S., Watanabe, K., Taniguchi, T., Kim, P., Shepard, K.L. and Hone, J., 2010. Boron nitride substrates for high-quality graphene electronics. Nature nanotechnology, 5(10), pp.722-726.

191. Nair, R.R., Blake, P., Grigorenko, A.N., Novoselov, K.S., Booth, T.J., Stauber, T., Peres, N.M.R. and Geim, A.K., 2008. Universal dynamic

conductivity and quantized visible opacity of suspended graphene. arXiv preprint arXiv:0803.3718.

192. Michaelian, K.H., Wen, Q., Billinghurst, B.E., Shaw, J.M. and Lastovka, V., 2012. Far-and mid-infrared photoacoustic spectra of tetracene, pentacene, perylene and pyrene. Vibrational Spectroscopy, 58, pp.50-56.

193. Razeghi, M., Lu, Q.Y., Bandyopadhyay, N., Zhou, W., Heydari, D., Bai, Y. and Slivken, S., 2015. Quantum cascade lasers: from tool to product. Optics express, 23(7), pp.8462-8475.

194. Fujita, K., Jung, S., Jiang, Y., Kim, J.H., Nakanishi, A., Ito, A., Hitaka, M., Edamura, T. and Belkin, M.A., 2018. Recent progress in terahertz difference-frequency quantum cascade laser sources. Nanophotonics, 7(11), pp.1795-1817.

195. Barcelos, I.D., Bechtel, H.A., de Matos, C.J., Bahamon, D.A., Kaestner, B., Maia, F.C. and Freitas, R.O., 2019. Probing Polaritons in 2D Materials with Synchrotron Infrared Nanospectroscopy. Advanced Optical Materials, p.1901091.

196. Sanders, S., May, A., Alabastri, A. and Manjavacas, A., 2018. Extraordinary enhancement of quadrupolar transitions using nanostructured graphene. ACS Photonics, 5(8), pp.3282-3290.

197. Boncheva, M., Andreev, S.A., Mahadevan, L., Winkleman, A., Reichman, D.R., Prentiss, M.G., Whitesides, S. and Whitesides, G.M., 2005. Magnetic self-assembly of three-dimensional surfaces from planar sheets. Proceedings of the National Academy of Sciences, 102(11), pp.3924-3929.